Alma Mater Studiorum
Università degli Studi di Bologna

Facoltá di Scienze Matematiche, Fisiche e Naturali

Dipartimento di Astronomia

DOTTORATO DI RICERCA IN ASTRONOMIA

Ciclo XXIII

LOW FREQUENCY STUDY OF DIFFUSE
RADIO EMISSION IN CLUSTERS OF GALAXIES

Dottoranda:

GIULIA MACARIO

Coordinatore:
Chiar.mo Prof.

LAURO MOSCARDINI

Relatore:
Chiar.ma Prof.ssa

LORETTA GREGORINI

Co-relatore:
Dott.ssa **TIZIANA VENTURI**

Co-relatore:
Dott. **GIANFRANCO BRUNETTI**

QUESTA TESI E' STATA SVOLTA

NELL'AMBITO DELLE ATTIVITA' DI RICERCA

DELL' ISTITUTO DI RADIOASTRONOMIA

DELL' ISTITUTO NAZIONALE DI ASTROFISICA

(BOLOGNA)

Contents

Abstract

The presence of non-thermal components in galaxy clusters is now clearly established. Diffuse Mpc-scale radio emission from the Intracluster Medium (ICM) is observed in the form of centrally located *radio halos* and peripheral *relics* in an increasing number of galaxy clusters. Their synchrotron emission probes the existence of a population of relativistic electrons, mixed with the thermal gas and diffusing through μG magnetic fields. These large scale radio sources are always hosted by clusters showing signatures of merger activity. This observational evidence provides one of the most important basis for our understanding of the origin of these sources. Indeed, it is believed that cluster mergers dissipate a fraction of their energy release into shocks and turbulent motions in the ICM, which in turn may amplify the cluster magnetic fields and (re-)accelerate relativistic particles on large scales. In a general picture, merger driven turbulence could be at the basis of the origin of radio halos (the so-called turbulent re-acceleration models), while the models for the origin of radio relics relate these sources to merger shocks.

Radio halos and relics have typically steep spectra ($\alpha > 1$, with $S \propto \nu^{-\alpha}$) thus low frequency radio observations are best suited to detect these sources, and to study their properties. Due to the presently available interferometers, most of the radio halos and relics known to date have been observed and studied preferentially at 1.4 GHz, and very little information is available on their emission properties at lower frequencies ($\leq$330 MHz). The radio spectrum of these sources is a key observational tool to disentangle between the models for their origin. Only for a handful of halos and relics however the spectrum is well sampled by multi-frequency observations and over a wide frequency range.

To understand the origin of cluster scale diffuse radio sources it is essential to investigate their connection with the dynamical state of the host cluster and with the cluster thermal properties.

The thesis focuses on these crucial aspects and its aim is to study the spectral properties of radio halos and relics, and the connection of these sources with the thermal ICM.

The approach followed in this thesis is twofold. In particular:

1. We focus on two special cases, A 697 and A 754, the first one hosting a radio halo with very steep spectrum, the second one hosting complex diffuse emission connected with a shock front detected in the X-rays. These two systems allow us to study and discuss the relevance of the information that can be extracted from the spectrum of radio halos and from their connection with cluster mergers and shocks.

2. We make use of the great potential of low frequency observations in this research field, that became available only in the last years, thanks to the improved capabilities of present radio telescopes (*e.g.* GMRT), and the upcoming new facilities (*e.g.* LOFAR). In this respect, we selected a small sample of clusters with steep spectrum radio halo to observe with the GMRT at 150 MHz. First results from the analysis of these data are reported in this thesis for A 697 and A 521, where the diffuse cluster-scale radio emission is well detected at other frequencies, providing crucial information of their spectral properties. Furthermore, a fraction of this thesis has been devoted to the commissioning activities of LOFAR, that will shortly observe galaxy clusters in the frequency range $30 - 240$ MHz. First commissioning observations of the galaxy clusters are being performed, and a first LOFAR image of A 2256, hosting both a radio relic and a central halo, is reported.

The main steps of this thesis can be summarized as follows:

• We perform a detailed multifrequency study of the radio halo in A 697, based on new high sensitivity GMRT observations at 325 MHz, together with GMRT data at 610 MHz, and VLA observations at 1.4 and 1.7 GHz (both archival VLA data and proprietary EVLA data). A 697 is one of the few radio halos with ultra steep spectrum ($\alpha \gtrsim 1.5$, *i.e.,* USSRHs) known so far, a class of radio halos with spectral properties suitable to help in discriminating between different models proposed for the origin of radio halos. To investigate the connection between the halo and the dynamics of the host cluster, we use archival X-ray

Chandra observations. We discuss our results within the framework of the models proposed for the origin of radio halos. To constrain the low-frequency end of the spectrum, we also use follow–up GMRT observations of the cluster at 150 MHz: preliminary results show that it is consistent with the steep spectral index.

- We perform a multi-wavelength study of the cluster A 754, based on new deep *Chandra* X-ray and high sensitivity GMRT low frequency (330 MHz) radio observations.

  The cluster is one of the very few in which a merger shock front is clearly detected so far. The X-ray analysis allow us to unambiguously confirm the previously suggested presence of a shock front in the South-West direction, along the merger axis, through a direct measurements of both the gas temperature and density jumps across the surface brightness edge. The new GMRT observation at 330 MHz, together with archival VLA observations at 1.4 GHz and available information at 74 MHz, enable us to derive the spectral properties of the diffuse radio emission, and to discuss in detail the observed connection between the thermal ICM and the cluster non thermal components. In particular, our multi-wavelength analysis show that A 754 is the second cluster known with a clear spatial coincidence between a shock and diffuse emission on cluster scale. We discuss our results in the framework of the possible scenarios proposed for radio relic and halo formation.

- We present an observational project aimed at studying the low frequency properties of USSRHs. We carried out high sensitivity GMRT 150 MHz observations of three clusters selected from the GMRT radio halo survey cluster sample hosting a confirmed USSRH, *i.e.,* A 521 and A 697, and a candidate one, A 1682. We present preliminary images and results for A697 and A521. Such study is particularly relevant, given that to date the properties of cluster scale diffuse radio sources at frequencies below 330 MHz are still poorly explored. This study is also important in light of the upcoming LOFAR observations. As Ph.D. member of the LOFAR cluster survey Key Science Project, during the past two years I participated in the first commissioning activities. First results from commissioning observations of the nearby cluster A 2256, hosting both a radio halo and a relic, are also reported.

The chapters of this thesis are organized as follows.

In **Chap. 1** I briefly review the main properties of the hot ICM, and of X-ray galaxy clusters. Then I concentrate on the non-thermal components of the ICM, and summarize the present knowledge of diffuse cluster scale radio sources, with focus on cluster radio halos and relics. Their main observational properties are reviewed, together with the present theoretical scenarios proposed to explain their origin.

In **Chap. 2** I describe the GMRT radio halo survey, and review its main results on the statistical properties of cluster radio halos. Then, I describe the expectations of the re-acceleration model at low frequencies, with focus on USSRHs.

Chap. 3, reports on our multifrequency study of the radio halo in the merging cluster A 697. The origin of the radio halo is then discussed in the framework of the current models. The main results from this chapter are also published in Macario et al. (2010).

Chap. 4 illustrates our project of GMRT 150 MHz follow-up observations of USSRHs; preliminary results for A 697 and A 521 are presented. Some of the results from this chapter are also presented in Macario et al. (2011b).

Chap. 5 contains the results of our X-ray and radio analysis of the merging cluster A 754. The results from this chapter can also be found in Macario et al. (2011a).

Chap. 6 is devoted to illustrate the impact of upcoming LOFAR observations on the study of diffuse cluster scale radio emission; first commissioning observations of the cluster A 2256 are also reported.

Finally, in the **Conclusions**, I summarize the main results of the present thesis, and illustrate the forthcoming developments of our studies and the future perspectives in the study of diffuse emission in clusters of galaxies.

Throughout the whole thesis, a flat cosmology with $H_0 = 70$ km s^{-1} Mpc^{-1} and $\Omega_0 = 0.3$ is assumed. Moreover, we adopt the convention $S \propto \nu^{-\alpha}$ for the synchrotron spectrum (unless stated otherwise).

Chapter 1

Thermal and non-thermal components in galaxy clusters

1.1 Galaxy clusters: overview

Clusters of galaxies are among the most interesting objects in the cosmic large-scale structure, being the largest and most massive self-gravitating aggregates of matter in the present Universe. Historically, their discovery as concentration of galaxies is dated back to 1754, when Charles Messier first noticed a concentration of nebulae in the Virgo constellation (see the historical review by Biviano, 2000). The beginning of systematic studies of galaxy clusters as a class of astrophysical objects started about two centuries later, when the first *Catalogue of Galaxies and Clusters of Galaxies* was published by Herzog et al. 1957, just one year before the publication of the Abell's famous paper *The distribution of rich clusters* (Abell et al. 1989). Abell et al. (1989) provided the first extensive, statistically complete sample of rich galaxy clusters in the northern sky. Based on purely visual inspection, clusters were identified as enhancements in the galaxy surface density and were characterized by their richness and estimated distance. Afterwards, some further cluster catalogs became available (*e.g.* Zwicky & Kowal, 1968; Gunn et al., 1986).

Galaxy clusters include hundreds to thousands of galaxies, distributed over regions of $\sim 1 - 3h^{-1}$ Mpc size, depending on the magnitude range considered. The population of galaxies in clusters is substantially different from that in the field (*i.e., morphological segragation*; *e.g.* Dressler, 1980): clusters are richer in ellipticals and spheroidals, and poorer in spirals, if compared to the field galaxy population. Rich clusters are often dominated by a single, central cD galaxy. Different

cluster properties have been used to construct morphological optical classification systems which define a sequence of clusters from "regular" to "irregular". Regular clusters appear almost spherical and symmetric, and have a core with a high concentration of galaxies at the center. They do not show significant evidence of substructures. On the contrary, irregular clusters have little symmetry or central concentration, and often show substantial substructures. This suggests that regular clusters are dynamically more evolved and relaxed than irregular ones. Optical observations of galaxy clusters allow to determine their distance, through spectroscopic determination of the redshifts of member galaxies. The combination of the spatial and kinematic analysis of member galaxies allows to quantify the amount of substructures and to study in detail the cluster dynamical state (*e.g.* Girardi & Biviano 2002).

Galaxies are not the dominant component in a cluster of galaxies, despite of their name. The volume between member galaxies is permeated by the Intra Cluster Medium (hereafter ICM), hot and rarified gas which emits X-rays via thermal Bremsstrahlung, making galaxy clusters among the brightest X-ray sources in the sky. The hot ICM represents the main *baryonic* component of galaxy clusters. Typical values for the total mass of galaxy clusters are of $\sim 10^{14} - 10^{15} h^{-1}$ M$_\odot$. Galaxies and ICM contribute to this mass budget only for a small fraction (a few % and $\sim$ 15–20 %, respectively), compared to the dominant unseen non-baryonic dark matter component ($\sim$ 80 %), which determine the cluster gravitational potential and whose presence can be inferred from *i.e.,* gravitational lensing effects on visible matter (*e.g.* Schneider 2006; Clowe et al. 2006).

The currently accepted ΛCDM model predicts a bottom-up sequence of the formation of cosmic structures. In this hierarchical scenario, small objects form first, and then progressively merge to form larger and larger structures. Clusters of galaxies are thus the youngest gravitationally bound objects, and are believed to assemble and grow through accretion and merging of smaller mass units at the intersection of the filaments which constitute the "cosmic web". This picture is supported both by numerical simulation and observational results (*e.g.* Katz & White 1993, Borgani et al. 2004).

1.2 Thermal X-ray emission from galaxy clusters

Clusters of galaxies are very bright extended X-ray sources, with typical luminosities of $10^{43} - 10^{45}$ erg/s. The discovery of clusters as a class of X-ray luminous sources came in with the advent of astrophysics from space missions in 1960s, thanks to the *Uhuru* X-ray astronomy satellite (Giacconi et al., 1972). Felten et al. (1966) first suggested that the X-ray emission from clusters was due to hot diffuse intergalactic gas, that is in thermal equilibrium with the gravitational potential well: the ICM.

The ICM has temperatures $T \approx 10^7 - 10^8$ K and particle number densities of $n \approx 10^{-2} cm^{-3}$ in the central regions down to $n \approx 10^{-4} cm^{-3}$ at the outskirts. It is composed by ionized hydrogen and helium plus traces of heavier elements at about $1/3$ of the solar abundance, increasing to around solar at the centres (*e.g.* De Grandi & Molendi 2001). It emits X-rays mostly via thermal Bremsstrahlung. At densities and temperatures typical for the ICM, the ionization equilibrium timescale is very short, and the electron-ion equilibration timescale via Coulomb collisions is generally shorter than the age of the cluster. At a first approximation, the ICM can be considered as a plasma at a single temperature (*i.e.*, $T_e = T_i$ can be assumed in most cluster regions). Under these conditions, the emissivity of the Bremsstrahlung X-ray continuum radiation at energy E from such a plasma is:

$$J(E) \propto g_{eff} n_i n_e T_{\mathrm{e}}^{-1/2} e^{-E/k_B T_e} \tag{1.1}$$

where g_{eff} is the effective Gaunt factor, which includes all continuum mechanisms and depends weakly on E, T_e and ion abundances, which corrects for quantum mechanical effects and whose value is of the order of 1 (*e.g.* Rybicki and Lightman, 1979).

The shape of the X-ray emission spectrum from the ICM is essentially flat for $E << k_B T_e$, while it has a sharp cut-off for $E \gtrsim k_B T_e$, due to the exponential term $-E/k_B T_{\mathrm{e}}$. In fact the continuum X-ray emission of galaxy clusters is generally well described, at first approximation, by this equation, with typical temperature of 2-10 keV (emission in the soft X-ray band). On top of this continuum, line emission is observed, the most prominent being the ionized iron line (*e.g.* Mewe and Gronenschild 1981; Werner et al. 2008a for a recent review). For typical cluster temperatures (kT $\gtrsim$ 2 keV) the emissivity of thermal Bremsstrahlung dominates

that from emission lines.

The ICM is optically thin for X-rays for almost all densities encountered in clusters (except for the possible resonant scattering at energies of strong emission lines in the dense central regions; *e.g.* Gilfanov et al. 1987). An X-ray telescope thus map the projected ICM density and the electron temperature. The electron temperature, T_e, averaged along the line of sight, can be determined from the shape of the continuum exponential spectrum (see however *e.g.* Mazzotta et al. 2004). Since the emissivity strongly depends on the density (eq. 1.1), under reasonable assumptions about the structure of the whole cluster, it is possible to "deproject" the ICM temperature and density in three dimensions. With such methods, the mass of the hot ICM can be determined for those clusters whose gas atmospheres are spherically symmetric. It is found to account for 5-15% of the total mass, several times more than the stellar mass in galaxies (*e.g.* , Allen et al. 2002; Vikhlinin et al., 2006).

The existence of hot diffuse X-ray emitting gas requires the presence of a deep gravitational potential well to confine the gas in the cluster.
In the absence of major dynamical disturbances like mergers (Sect. 1.3), the ICM relaxes to hydrostatic equilibrium on timescales similar to the sound crossing time of the ICM, which is much shorter than the cluster lifetime ($\sim$ age of the Universe). Under the assumptions of hydrostatic equilibrium and spherical symmetry of the gas and the total matter distribution, the total cluster mass within radius r can be written as:

$$M(< r) = -\frac{k_B T(r) r^2}{G \mu m_{\mathrm{p}}} \left(\frac{\mathrm{d} \ln \rho_{\mathrm{gas}}(r)}{\mathrm{d} \ln r} + \frac{\mathrm{d} \ln T(r)}{\mathrm{d} \ln r} \right) \, , \tag{1.2}$$

where μ is the mean molecular weight in a atomic mass unit, and m_p is the proton mass. Thus it is possible to derive the cluster total mass within a certain radius r, by measuring the radial distributions of the gas temperature $T(r)$ and density $\rho(r)$ (*e.g.* Sarazin, 1988). This method is complementary to those using galaxy velocity dispersions, gravitational lensing analysis (*e.g.* Schneider 2006), the caustic technique (Diaferio et al. 1999), and the measure of the Sunayaev-Zeldovich (SZ) effect (*e.g.* Bartlett et al. 2006). All those methods indicate that galaxy clusters contain $\sim 10^{14}$–10^{15} M$_\odot$, which is dominated by the dark matter ($\sim$ 75-80 % of the total); for those clusters where a comparison is possible, different total mass measurement usually agree to within a factor of 2.

To determine the properties of the ICM from the observed X-ray emission, a model for the distribution of the gas is needed. A common description of the gas density profile is given by the so-called β-model (Cavaliere & Fusco-Femiano 1976; 1978):

$$n_e(r) = n_e(0) \left[1 + \frac{r^2}{r_c^2}\right]^{-3/2\beta}, \qquad (1.3)$$

where $n_e(0)$ is the central electron number density, r_c is the core radius, while the parameter β is the ratio between the kinetic energy of any tracer of the gravitational potential (*e.g.* galaxies) and the thermal energy of the gas: $\beta = \frac{\mu m_p \sigma_r^2}{k_B T}$, where σ_r is the one dimensional velocity dispersion of the galaxies. This model assumes that both the galaxies and gas are isothermal and bound to the cluster, and that the gas is in hydrostatic equilibrium and the galaxies have an isotropic velocity dispersion. An additional assumption is the spherical symmetry of the gas.

Even though none of the assumptions at the basis of this isothermal model can be firmly verified, from Eq. 1.3 it is easy to derive the expression for the projected X-ray surface brightness:

$$S(r) = S(0) \left[1 + \frac{r^2}{r_c^2}\right]^{-3\beta+1/2} \qquad (1.4)$$

where $S(0)$ is the central surface brightness.

This parametrization is widely used in the X-ray astronomy to recover the gas density profile by fitting the surface brightness profile in galaxy clusters. However, this model often underestimates the surface brightness in the central core of relaxed clusters (*e.g.* Jones & Forman 1984) while overestimates the brightness at large radii ($r >> r_c$; *e.g.* Vikhlinin et al. 1999). The high sensitivity and and high resolution observations of clusters with *Chandra* and *XMM*-Newton telescopes revealed that the ICM is not strictly isothermal; typically, the temperature decreases towards the cluster centers and towards the edges (*e.g.* Vikhlinin et al. 2006). Moreover, the assumption of hydrostatic equilibrium is not strictly applicable in the case of unrelaxed merging clusters.

1.2.1   Cool-core and non cool-core clusters

Observationally, X-ray clusters can be divided into two classes: cool core (CC) clusters with dense gaseous core regions in which gas temperature drops inwards,
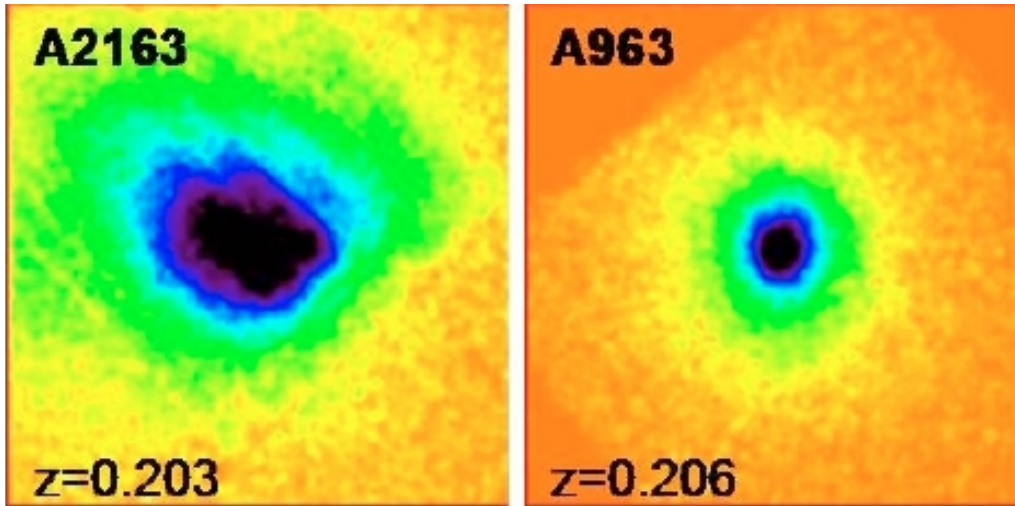
Figure 1.1: *Chandra* X-ray images showing a well known merging cluster, classified as non cool-core cluster (A 2163, left image) and a more relaxed systems, classified as cool core cluster (A 963). Taken from Santos et al. 2008.

and non-cool core (NCC) clusters with shallower core profiles (*e.g.* Jones & Forman 1984; Peres et al. 1998; Schuecker et al. 2001). Cool core clusters have sharply peaked X-ray emission at their centres due to the rise in central gas density which allows efficient central cooling.

CC clusters have central cooling times significantly lower than the Hubble time. Formerly, it was believed that the ICM in the cores of CC clusters cools and condenses, given the absence of heating mechanisms to compensate the radiated energy, and therefore these clusters were termed cooling flow clusters (*e.g.* Fabian et al. 1994). With the advent of the *XMM*-Newton and *Chandra* satellites, the spectral features predicted by the cooling flow picture were not observed in the X-ray spectra of the cores of CC clusters (*e.g.* Peterson et al. 2001 and Peterson et al. 2003). In particular, the gas is not observed to cool to very low temperatures at the rates expected from the observed core X-ray luminosities, and a consensus has now emerged that this is due to the feedback from a central active galactic nucleus, which limits the effects of cooling through processes which are still not very well understood (*e.g.* Peterson & Fabian 2006, for a review of cool cores in clusters).

Besides the presence of a central peak in the gas density and surface brightness, CC clusters have relatively undisturbed ICM (*e.g.* Fig. 1.1, right panel), indicating

that they are fairly dynamically relaxed. On the other hand, NCC clusters typically shows more substructures (*e.g.* Jones & Forman 1984; Peres et al. 1998; Schuecker et al. 2001; *e.g.* Fig. 1.1, left panel). This dichotomy may reflect a different origin for the two classes, which may be due to a primordial division (*e.g.* O'Hara et al. 2006; McCarthy et al. 2008). However, present observations support an evolutionary scenario (*e.g.* Rossetti & Molendi 2010), in which galaxy clusters should naturally evolve into a CC state, until a merger event occurs. The energy released by the merger can thus efficiently disrupt the cool core, leading to NCC clusters which should be in an un-relaxed, post-merger stage (*e.g.* Gómez et al. 2002).

1.3 Merging clusters: observations of substructures

In the hierarchical scenario for the the formation of cosmic structure, galaxy clusters are believed to form through anisotropic and episodic accretion of mass. It is thus expected that a fraction of them shows deviations from the spherical symmetry and that signatures of these phenomena are visible in X-ray and optical data. Indeed, a large fraction of clusters shows evidence of substructures both in their galaxy distribution and in X-ray emission morphology. The fraction of clusters with substructures depends on the cluster sample and on the substructure identification technique, but it is substantially lying in the range 30-80% (*e.g.* Ramella et al. 2007, and references therein), and increases with redshift (Jeltema et al. 2005).

In particular, optical studies may reveal signatures of the dynamical activity in clusters by the analysis of the line-of-sight velocity distribution of cluster member galaxies, as well as the presence of substructures and segregation in the galaxy distribution projected on the plane of the sky (*e.g.* Girardi & Biviano 2002). A most efficient way to constrain the dynamical state of clusters is however based on X-ray studies.

Early observations performed with the *Einstein* satellite soon revealed that X-ray clusters have a variety of morphologies, from regular to very complex systems with multiple substructures (*e.g.* Jones & Forman 1999). Direct observations of merger events were first provided by the ROSAT (*e.g.* Briel et al. 1991; 1992) and ASCA (*e.g.* Markevitch et al. 1999) satellites, probing that clusters are still assembling at the present epoch, as expected in the hierarchical formation model.

With the advent of *Chandra* and *XMM*-Newton both the density and temperature structure of the ICM in nearby clusters have been mapped with unprecedented accuracy, enabling deep investigation of the cluster dynamics and the effect of the mergers on the ICM. The high angular and spectral resolutions of those X-ray telescopes allows to resolve the internal structure of clusters, and to identify signature of merger activity: substructure in the gas density distribution, multiple peaks, distortions, edges and tails of emission; patchy temperature structures (*e.g.* Markevitch et al. 2000; Henry et al. 2004; Belsole et al. 2005); metallicity gradients (*e.g.* Finoguenov et al. 2006, Werner et al. 2008b); surface brightness discontinuities associated with jumps in gas density and temperature, *i.e.,* bow shocks (see Section 1.8.1) and cold fronts (*e.g.* Markevitch & Vikhlinin 2007).

At high redshift the number of irregular and merging clusters increases, in line with what is expected in the hierarchical scenario for structure formation. One of the most spectacular examples of an interacting system is the cluster MACS J0717+3745, at z=0.55, where a triple ongoing merger has been observed (Ebeling et al. 2004).

All these results indicate that merging episodes are common phenomena in clusters, and their signatures can be studied through optical studies of member galaxies and X-ray observations of the *thermal* ICM. Such energetic phenomena may also have important effects on the *non-thermal* components of galaxy clusters, as we will see in the following Sections.

1.4   The non-thermal components of the ICM

The ICM does not contain hot thermal gas only. Observations have revealed that magnetic fields and relativistic particles are also present on cluster scales. These are referred to as *non-thermal* components of the ICM.

The clearest evidence for the existence of non-thermal components in the ICM comes from the observations of diffuse synchrotron radio sources extended on Mpc scales, which directly probes the presence of magnetic fields and relativistic electrons on the cluster scale. These sources are the object of study of the present thesis, and will be discussed in detail in the next sections.

The existence of intracluster magnetic fields is also probed by Faraday Rotation

Measures of radio sources behind and inside galaxy clusters, which are enhanced with respect to the field sources (*e.g.* Clarke et al. 2001, 2004; Govoni et al. 2001b; Johnson-Hollit et al. 2004).

Possible evidence for relativistic electrons in the ICM comes from the hard X-ray (HXR) band. In a few galaxy clusters, an excess of emission has been detected in the hard region of the X-ray spectrum (i.e. $\gtrsim$ 10 keV) exceeding the high energy extrapolation of the thermal soft-X ray emission (*e.g.* Coma, Fusco-Femiano et al. 1999; 2004, Rephaeli & Gruber 2002; A2256, Fusco-Femiano et al. 2000, 2005, Rephaeli & Gruber 2003; A754, Fusco-Femiano et al. 2003; see Rephaeli et al. 2008 for a complete recent review). The most likely interpretation of the non-thermal HXR emission in clusters is Inverse Compton (IC) radiation from relativistic electrons scattering photons of the cosmic microwave background (*e.g.* Fusco-Femiano et al. 2000). However the existence of HXR excess and its origin still remain controversial (*e.g.* Rossetti & Molendi 2004; Fusco-Femiano, Landi & Orlandini 2007; Ajello et al. 2009, 2010; Wik at al. 2009, 2011). If confirmed by the next hard X-ray imaging missions (*e.g.* NuSTAR/ Astro-H), the HXR excess will represent an important tool to derive the amount of the ICM energy in terms of relativistic electrons.

1.4.1 General properties of cluster-scale diffuse radio emission

Radio observations reveal the presence of spectacular diffuse radio sources in a fraction of massive galaxy clusters.

Cluster scale diffuse radio sources are very extended regions of emission, whose linear sizes ranges from hundreds of kpc to up and above the Mpc scale. Such emission is not associated with individual galaxies but with the ICM. Diffuse cluster scale radio sources are characterized by common observational properties. Their integrated radio spectrum has a typical power-law shape, which indicates the non-thermal synchrotron origin of the emission, and probes the presence of relativistic electrons (Lorentz factor $\gamma \sim 1000$) and magnetic fields (~ 0.1-1 μG) permeating the cluster volume. The observed spectral indices of these sources are steep, with $\alpha \gtrsim 1$, and their radio emission has very low surface brightness ($\sim$ mJy to $\sim \mu$Jy arcsec^{-2} going from the MHz to the GHz range). These characteristics, combined with their large extent, makes their the detection and study very difficult with the

current radio telescopes.

Despite these common features (nature of emission, steep radio spectra, low surface brightness), cluster diffuse radio sources can be distinguished and classified on the basis of their different properties (size, position in the host cluster, intensity of polarized signal, morphology). In the literature, three main classes are usually defined, in particular *radio halos*, *radio relics* and *mini-halos* (see *e.g.* Ferrari et al. 2008 for a recent review).

While the thermal X-ray emission is present in all galaxy clusters, these diffuse radio sources have been detected only in a fraction of clusters. Since the discovery of the first radio halo in the Coma cluster (Large et al. 1959, Willson 1970), high sensitivity radio observations over the last 20 years have detected an increasing number radio halos, relics and mini halos. At present they are only observed in about 50 galaxy clusters, which suggests that these sources are relatively rare (*e.g.* Giovannini et al. 1999; see also Chapter 2).

In the following sections, we discuss in more details the physical properties of these class of sources, with particular focus on radio halos and relics.

1.5   Radio halos

Radio halos are spectacularly wide (~ 1 Mpc) and diffuse radio sources found in the central regions of galaxy clusters. They usually show a fairly regular morphology, with a radio surface brightness distribution which is peaked at the cluster centre and smoothly decreases towards the periphery. Their largest linear size (LLS) ranges from few hundreds of kpc up to and well beyond the Mpc scale. The sources with LLS $\gtrsim 1$ Mpc are referred to as *giant* radio halos, according to the definition in Cassano & Brunetti (2005). In Figure 1.2 we report the radio images of two giant radio halos, overlaid on the X-ray *Chandra* images of the hosting clusters. The prototypical and best studied radio halo is Coma C, in the rich and nearby Coma cluster (Wilson et al. 1970; Schlickeiser et al. 1987; Kim et al. 1990; Giovannini et al. 1993; Deiss et al. 1997; Thierbach et al. 2003; Brown & Rudnick 2010). The 327 MHz image of this source is reported in Figure 1.3 (left panel).

The emission from radio halos is unpolarized down to a few percent level, with upper limits for the fractional polarisation $< 5\text{-}10\%$ ($< 10\%$ in Coma; $< 6.5\%$ in A2219; $< 4\%$ in A2163; see Govoni & Feretti 2004 and references therein). This is

generally interpreted as due to Faraday depolarization internal to the radio emitting region, which thus demonstrates that the emission is coming from a large volume rather than a projected slab.

The first detection of polarized emission from a radio halo has been found in Abell 2255 (Govoni et al. 2005). This source shows a very complex and filamentary structure, with the brightest filaments strongly polarized at levels of $\sim$ 20-40 %. More recently however, Pizzo et al. (2011) have shown, through a rotation measure tomography of the cluster, that the polarized filaments lie at large distance from the cluster centre, suggesting that they could be relics in the foreground of the cluster seen in projection in the central halo region. Recently, Bonafede et al. (2009a) also found polarized emission in the radio halo discovered in the distant cluster MACS J0717+3745.; future rotation measure studies will help in clarifying whether also in this case the polarized filament if truly related to the radio halo or not.

The integrated radio spectrum of halos is that typical of aged radio sources, *i.e.,* steep with $\alpha \gtrsim 1$, with average values $\sim 1.2 - 1.4$. However, the shape of the synchrotron spectrum of radio halos is still poorly known since they are generally observed only at few frequencies, and over small frequency ranges.

The few radio halos for which radio observations cover an adequate frequency range show evidences of a spectral steepening at high frequency. The integrated radio spectrum of Coma C, is known in a frequency range that spans three order of magnitudes. It is a power law with $\alpha \sim 1.2$ at frequency below 1.4 GHz, while observations at higher frequencies reveal the presence of a cut-off (Schlickeiser et al. 1987; Thierbach et al. 2003) which is interpreted as due to a break in the spectrum of the emitting electrons (see right panel of Fig. 1.3). In few other cases, a steepening of the halo spectrum at high frequency has been tentatively detected (A 1914, Komissarov & Gubanov 1994; A 2319, Feretti et al. 1997; A 754: Bacchi et al. 2003; A 3562, Giacintucci et al. 2005; A 521, Brunetti et al. 2008).

The analysis of the spectral index distribution of a few well studied radio halos revealed the presence of inhomogeneities on small scales, which may reflect the complex form of the energy distribution of the radio emitting particles in these sources. Indications that the spectral index steepens radially with the distance from the cluster centre have been pointed out in Coma by Giovannini et al. (1993), and in A 665 and A 2163 by Feretti et al. (2004). Orrú et al. (2007) have shown that the
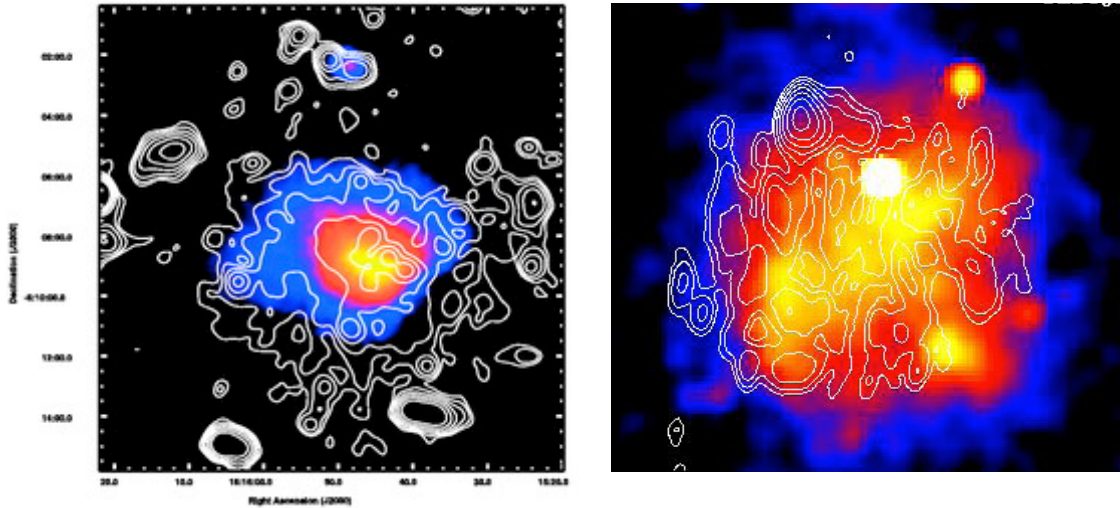
Figure 1.2: Two examples of giant radio halos (radio contours), overlaid to the X-ray Chandra images of the host clusters. *Left panel* - VLA 1.4 GHz radio contours of the radio halo in A2163 (LLS $\sim$ 1.9 Mpc); from Govoni et al. 2004. *Right panel* - VLA 1.4 GHz radio contours of the halo in RXCJ 2003.5-2323 (LLS $\sim$ 1.4 Mpc); from Giacintucci et al. 2009.

radio halos in A 2744 and A 2219 have an overall spectral index, averaged over the whole cluster, without a clear radial steepening, but with a very patchy structure. Spectral index image of the radio halo in A3562 also showed a complex structure (Giacintucci et al. 2005).

General statistical properties and correlations

At present, about 20 clusters are known to host a radio halo. A first observational contribution to the statistical properties of radio halos at z$\leq$ 0.2 has been obtained by means of deep follow-ups with the VLA of candidate radio halos identified on the NVSS (NRAO VLA Sky Survey; Condon et al. 1998) and WENSS (Westerbork Northern Sky Survey, Rengelink et al. 1997) radio surveys (Feretti 2003, for a review). By inspecting the 1.4 GHz NVSS survey, Giovannini et al. (1999) found that $\simeq$5% of the galaxy clusters in a complete X-ray flux-limited sample at z$\leq$0.2 host a diffuse halo source. The halo fraction increases with the X-ray luminosity of the hosting cluster, up to $\sim$ 30-35 % for clusters with X-ray luminosity larger than 10^{45} erg/s (Giovannini & Feretti 2002). Those studies may be however affected by selection biases, due to the brightness limit of the radio survey used to select radio halo candidates.
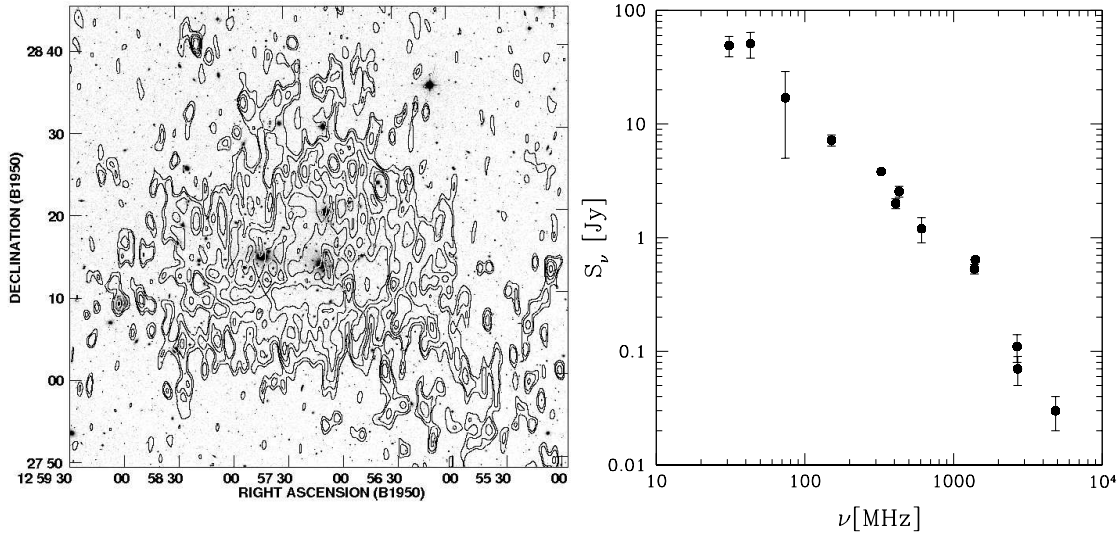
Figure 1.3: *Left panel* - 327 MHz 90 contours of the giant radio halo in the Coma cluster (z = 0.023), overlaid on the DSS optical image. Radio point sources have been subtracted (Feretti 2002) *Right panel* - Integrated radio spectrum of Coma C between 30.9 MHz and 4.9 GHz; a steepening in the spectrum stands out clearly >1 GHz (adapted from Thierbach et al. 2003).

More recently, deep radio observations of a complete sample of galaxy clusters in the redshift range z=0.2-0.4 have been carried out as part of the Giant Metrewave Radio Telescope (GMRT) Radio Halo Survey (Chapter 2; Venturi et al. 2007, 2008). These observations confirmed that diffuse cluster-scale radio emission is not ubiquitous in clusters: only 30% of the most X-ray luminous (L_X (0.1 - 2.4 keV) $\geq 5 \times 10^{44}$ erg/s) clusters host a radio halo.

Radio halos trace a well known correlation between their radio power $P_{1.4}$ and the X-ray luminosity of the host clusters L_X (*e.g.* Liang et al. 2000; Giovannini & Feretti 2002; Cassano et al. 2006 and 2007). A relation with a much larger scatter between $P_{1.4}$ and X-ray temperature of the ICM (T_X) has also been observed (*e.g.* Liang et al. 2000). Since both the cluster X-ray luminosity and temperature are correlated with the cluster mass (Reiprich & Böhringer 2002), the observed correlations reflect a dependence of radio halo power on the cluster mass.

1.6   Radio Relics

Similarly to radio halos, cluster radio relics are wide (≈ 1 Mpc) diffuse, low surface brightness, steep spectrum radio sources. They are usually located at the outskirts of the host clusters and have typically elongated morphologies, with various shapes (sheet and arc-like being the more common) and sharp emission edges.

The prototype of the class of cluster radio relics is 1253+275 in the Coma cluster (Ballarati et al. 1981; Giovannini, et al. 1991; Thierbach et al. 2003; also reported in the left panel of Fig. 1.4). At present that there are ~ 20 clusters of galaxies which are known to host at least one radio relic.

Contrary to radio halos, the emission of radio relic is strongly polarized, with typical linear fractional polarization at 1.4 GHz of 10-30 % (*e.g.* 1253+275, Thierbach et al. 2003), reaching values up to 50-60 % in some regions (*e.g.* in the A2256 relic, Clarke & Enßlin 2006; in CIZA J2242.8+5301, van Weeren et al. 2010). This is consistent with the fact that these sources originate from the cluster peripheries.

Impressive cases of double radio relics, extending on both sides of the X-ray emission and almost symmetrically located with respect to the cluster centre, have been observed. The first double relic cluster is A3667 (Rottgering et al. 1997; Roettiger et al. 1999a; Johnston-Hollitt et al. 2002). Other examples are found in A3376 (Bagchi et al. 2006), and in A2345 an A1240 (Bonafede et al. 2009b).

Very recently, van Weeren et al. 2010 discovered the most impressive case of double relics in the cluster CIZA J2242.8+5301 (Fig. 1.5, left panel). As seen in Fig. 1.5 (left panel) the northern relic is extremely narrow and its shape is close to a perfect arc.

In a growing number of clusters, the coexistence of both a central radio halo and a peripheral relic have been observed. For example in Coma (Giovannini et al. 1993) and A 2256 (see right panel of Fig. 1.5; *e.g.* Clarke & Enßlin 2006). Other clusters in which both a radio halo and a peripheral relic co-exist are A 521 (Sections 2.3 and Chapter 4; Giacintucci et al. 2006; 2008; Brunetti et al. 2008; Dallacasa et al. 2009) and A 2744 (Orru' et al. 2007, Venturi et al. 2011 to be submitted). The only cluster presently known to host both double relics and a central radio halo is RXCJ 1314.4-2515 (Feretti et al. 2005; Venturi et al. 2007).

To date, the available data and detailed knowledge of the physical properties
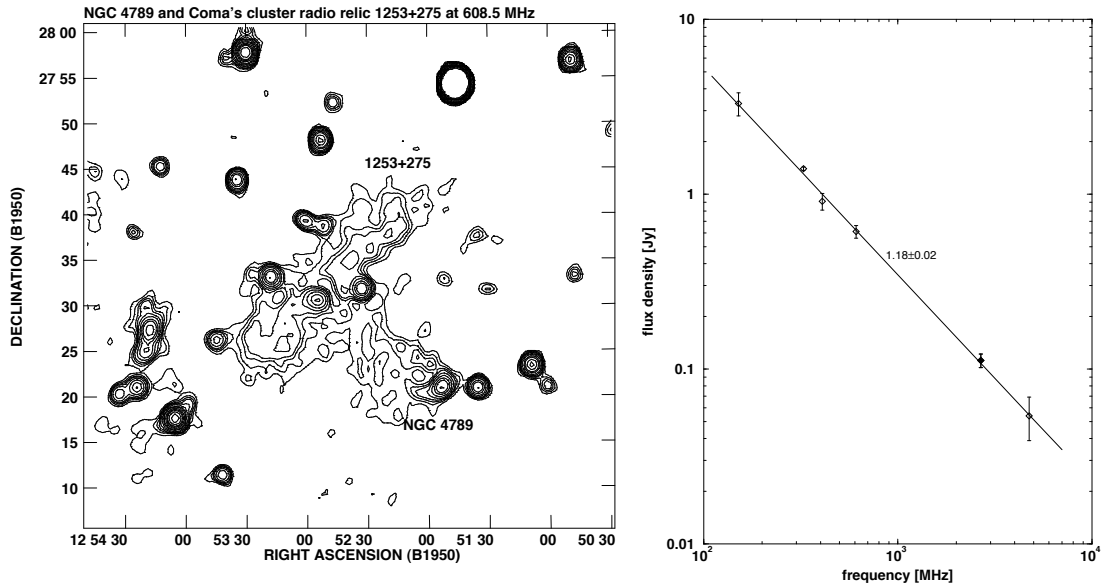
Figure 1.4: *Left panel* - 608 MHz image of the radio relic 1253+275 in the Coma cluster (from Giovannini et al. 1991) and the nearby narrow angle tail radio galaxy NGC4789. *Right panel* - Integrated radio spectrum of 1253+275 between 151 MHz and 4.75 GHz. The solid line is the best power-law fit to the data and has = 1.18 ± 0.02 (reproduced from Thierbach et al. 2003).
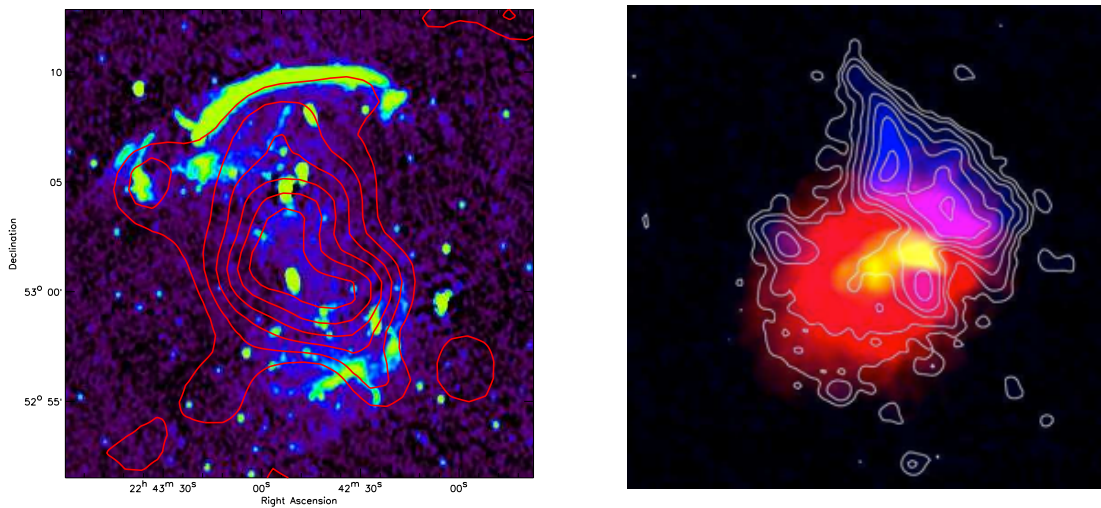
Figure 1.5: *Left panel* - WSRT 1.4 GHz radio image of the double relics in CIZA J2242.8+5301. Red contours represent the X-ray emission from ROSAT showing the hot ICM; from Van Weeren et al. 2010. *Right panel* - VLA 1.4 GHz image of the radio relic and halo (white contours) in A2256, on the X-ray Chandra cluster image (from Clarke & Enßlin 2006)

of radio relics are still poor, and the number of well studied sources is limited. Integrated radio spectra over a wide range of frequencies are available for few relics only. One of the relics with accurate flux density measurements at many different frequencies is 1253+275 in the Coma cluster: the total spectrum of this source is well fitted by a single power law with ∼1.2 extending on about two orders of magnitude in frequency (Thierbach et al. 2003). Another very well studied relic is the one in A 521, whose spectrum is known between 240 MHz and 5 GHz, and it is well fitted by a single power law with ∼1.5 (Section 2.3; Sect. 4.6; Giacintucci et al. 2008). A single power-law integrated spectrum is observed also for the northern narrow relic in CIZA J2242.8+5301 (Fig. 1.5, left panel).

Unlike radio halos (Sec. 1.5), no steepening at high frequencies is observed in the spectrum of these well studied relics. However, multifrequency radio information is needed for most relics, in order to test whether the absence of a high frequency steepening is a common feature within this class of radio sources.

For a few relics, images of the spectral index distribution were reported in the literature (*e.g.* A3667, Rottgering et al. 1997; 1253+275, Giovannini et al. 1991; A2256, Clarke & Enßlin 2006, Kale & Dwarakanath 2010; A2744, Orrú et al. 2007; A521, Giacintucci et al. 2008 ; A2345 and A1240, Bonafede et al. 2009b; CIZA J2242.8+5301, van Weeren et al. 2010). Those studies have shown indication of radial spectral steepening along the source minor axis, with the the flattest spectrum in the external side of the relic with respect to the cluster centre (due to the radiative ageing of electrons; Sect. 1.9.2).

1.7 Mini-halos

Mini-halos are diffuse extended radio sources of moderate size (few 10^2 kpc, LLS ≤ the cluster X-ray cores) and quite regular morphology, and always surround the dominant powerful radio galaxies at the cluster centre. Similarly to radio halos they are characterized by steep spectrum and very low surface brightness. Our current observational knowledge of mini halos is limited to about ten sources (*e.g.* , Perseus: Burns et al. 1992; A2390: Bacchi et al. 2003; RXJ1347.5-1145: Gitti et al. 2007, A1835, A2029, Ophiucus: Govoni et al. 2009; RXCJ1504.1-0248, recently discovered by Giacintucci et al. 2011). The detection of radio mini halos is complicated by the requirement of high dynamic range and resolution radio observations, to disentangle

between the different contributions from the central radio galaxy and the diffuse minihalo emission.

Interestingly, radio mini-halos are typically observed at the center of cool core clusters (see Section 1.2.1), and their sizes are comparable to that of the cooling region. Detailed individual studies indicate a possible relation between the mini-halo emission and some minor merger activity or sloshing of cluster core gas (see *e.g.* Gitti et al. 2007, Mazzotta & Giacintucci 2008, Govoni et al. 2009, Giacintucci et al. 2011).

1.8 Cluster mergers, shocks and turbulence

So far, radio halos and relics have been observed only in X-ray luminous galaxy clusters with evidence of substructures and disturbed dynamical activity (*e.g.* Buote 2001; Cassano et al. 2010b), which are clear signs of recent or ongoing merger event (see Sect. 1.3).

Clusters hosting a radio halo and/or a relic usually exhibit substructures in the spatial and velocity distributions of optical galaxies, as well as substructures and distorsions in the X-ray brightness distribution (Schuecker et al. 2001). They often show temperature gradients and shock heated regions (*e.g.* Markevitch et al. 1998; Markevitch & Vikhlinin 2001).

Moreover, an anti-correlation between clusters hosting radio halos and relics with the presence of a dense cool core is observed (*e.g.* Feretti 1999). This is a further indication that the cluster has undergone a recent merger event, as strong mergers are expected to disrupt the cool core, as shown, for example, by the simulations in Gömez et al. 2002.

Although not all merging clusters host a diffuse radio source, there is still no evidence of any radio halo or relic in a cluster where the presence of a merger can be firmly excluded (*e.g.* Buote 2001; Cassano et al. 2010b).

Cluster mergers are the most energetic events in the Universe since the Big Bang, with a total kinetic energy of the colliding sub clusters reaching $\sim 10^{64} - 10^{65}$ ergs (Markevitch et al. 1999). In the course of a merger, a significant fraction of this energy is converted into thermal energy on a typical time scale of ~ 1 Gyr by large scale hydrodynamical shock waves, driven in the gaseous atmosphere of the

cluster (Sec. 1.8.1). Furthermore, it is expected that a fraction of the merger energy is dissipated also through large scale turbulent motions of the gas (Sec. 1.8.2).

Merger shock waves and turbulence may have an important role in determining the non-thermal properties of the ICM. Indeed, they may amplify the cluster magnetic fields and accelerate or re-accelerate high energy particles in the cluster volume (see Sec. 1.9.1 and 1.9.2).

1.8.1 Merger Shock waves

Mergers between sub clusters happen at velocities of $\sim 2000 - 3000$ km s^{-1}, which are slightly higher than the sound speed in the ICM, ~ 1000–1500 km/s. The relative motions in cluster mergers are thus modestly supersonic, and shocks waves are driven into the ICM of the subclusters (*e.g.* Sarazin 2002).

The expected Mach number of such merger shocks is $M = v_s/c_s \lesssim$ 2–3 (*e.g.* Gabici & Blasi 2003), where v_s is the velocity of the shock relative to the pre-shock gas and $c_s = \sqrt{(5/3)P/\rho}$ the sound speed in the pre-shock gas, with P and ρ its pressure and density, respectively.

The formation of weak merger shock waves is also indicated by hydrodynamical simulations of cluster mergers (*e.g.* Ricker & Sarazin 2001; Ryu et al. 2003; Pfrommer at al. 2006; Vazza et al. 2010a). Most of these numerical simulations show that the bulk of the kinetic energy is dissipated in thermal energy at shocks with Mach number $M \sim 2$ in clusters, and the distribution of the energy flux through shocks in the Universe can be broadly described by a steep power law. An example of this is shown in Fig. 1.6 (Vazza et al. 2010a).

Cosmological simulations also predicts the existence of shocks with higher Mach numbers ($M \gtrsim 10$) in more peripheral cluster regions, the so called "accretion" or "external shocks", resulting from accretion of cold gas into already formed structures (*i.e.,* dark matter nodes; see Bykov et al. 2008 for a review).

In major mergers (*i.e.,* mergers between sub clusters of similar masses), hydrodynamical shocks dissipate energies of $\sim 10^{63} - 10^{64}$ ergs and are thus the major heating source of the X-ray emitting gas (*e.g.* Sarazin 2002). Merger shock waves are responsible for irreversible changes in the ICM. During their propagation, the shock fronts compress and heat the gas to temperatures up to several keV, and also increase its entropy (*e.g.* Ricker & Sarazin 2001; Randall et al. 2002).
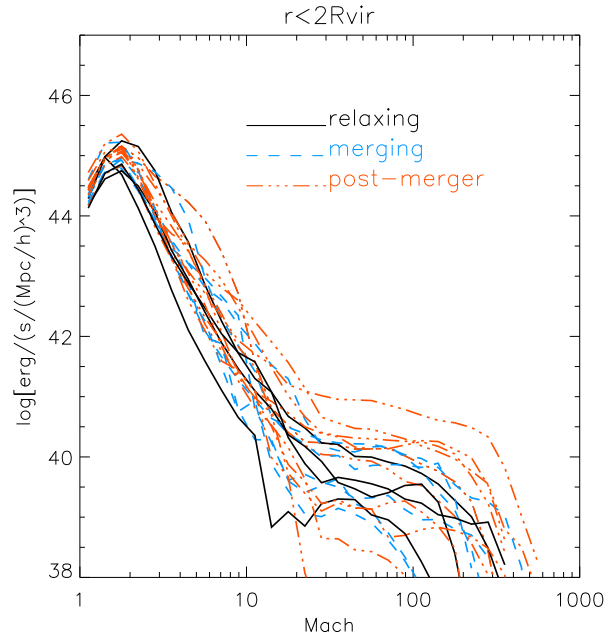
Figure 1.6: Distribution of the energy flux dissipated at shock waves of different Mach number, for a sample of massive galaxy clusters simulated with the grid code ENZO (see Vazza et al. 2010a for details).

X-ray observations of clusters of galaxies are the natural way to look for merger shock fronts, since they create sharp discontinuities in the cluster X-ray surface brightness images. However, known merger shock fronts are still rare, and their detection is difficult with the available X-ray instrumentation, for different reasons. Shock fronts created during the merger quickly propagates towards the cluster outskirts. However, fronts are more effectively detected close to the cluster centre, in high surface brightness regions, since the X-ray background emission dominates the peripheral regions. Moreover, the merger has to be occurring nearly in the plane of the sky, otherwise projection effects could hide the gas density and temperature jumps. So far, reliable detections of merger shock fronts have been reported in only four galaxy clusters (see Markevitch 2010 for a recent review), all made possible thanks to the extremely high resolution X-ray imaging capability of the *Chandra* observatory. One is the famous Bullet cluster (1E0657-56, Markevitch et al. 2002 and 2006). The impressive image of the bow shock and the clear jumps in the X-ray surface brightness and projected temperature profiles across the discontinuity are reported in Figure 1.7. Another merging cluster with a clear shock front is Abell 520 (Markevitch et al. 2005). Two symmetric fronts have been recently discovered

in Abell 2146 (Russell et al. 2010). A shock front in Abell 754 has been detected and studied in the present thesis (see Chapter 5; see also Macario et al. 2011a).
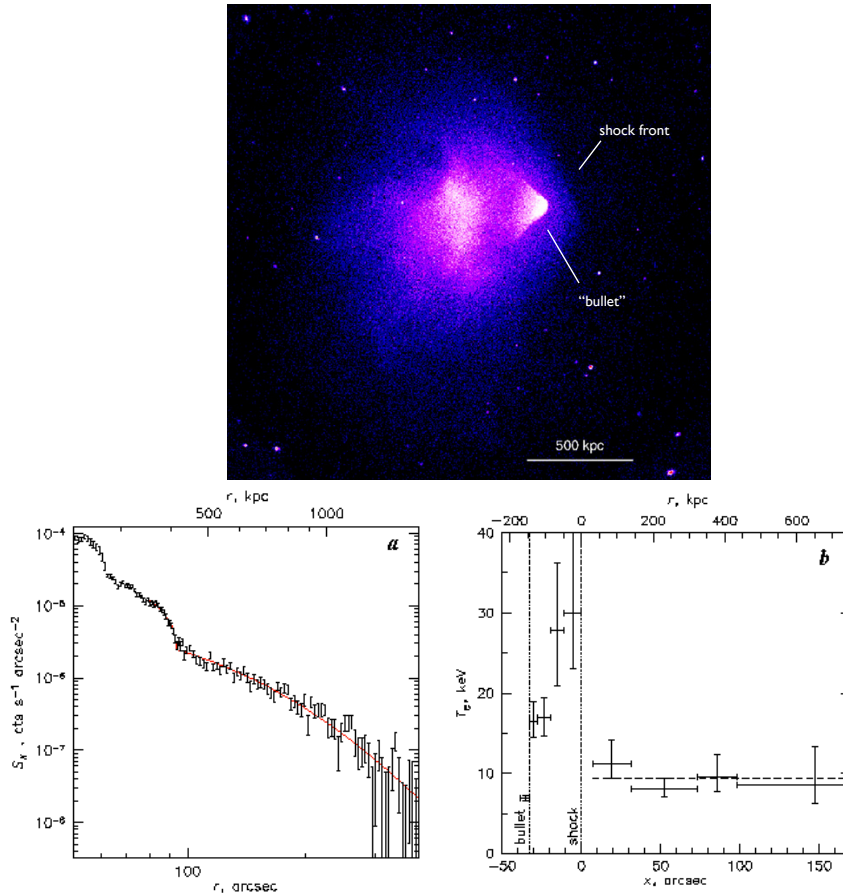
Figure 1.7: Shock front in the bullet cluster, 1E 0657-56. *Upper panel*: Chandra X-ray image of the cluster (0.8-4 keV band); the "bullet" of cold gas is preceded by the hot shock front. From Markevitch 2010. *Lower panel*: a) X-ray surface brightness profile across the shock, with the best-fit model for the density jump (solid line); b) X-ray projected temperature profile across the shock. From Markevitch 2006.

Only in these four clusters both the sharp gas density edges and the unambiguous temperature jumps were revealed, allowing the identification of the brightness feature as a shock and determination of both the shock Mach number and the gas velocity [1].

The highest Mach number is $M \simeq 3$ in 1E 0657-56, while the other known shock fronts have $M \simeq 1.6 - 2$. These values are in agreement with the expected Mach numbers

---

[1]At present there are few other likely merger shock fronts seen in the X-ray images (Coma, A3667, A2744, RXJ 1314-25, A 521), but a clear detection of temperature jumps across the putative fronts is still missing (see Markevitch 2010 for more details).

of merger shocks in clusters derived by analytical studies and hydrodynamical simulations ($M \lesssim 2 - 3$).

1.8.2   Merger-driven turbulence

Turbulence is expected to develope during galaxy clusters formation through mergers and accretion of matter. Cluster mergers may excite a non-negligible amount of turbulent motions in the gas of the colliding subclusters, due to the action of ram pressure and fluid instabilities that strip the gas from infalling dark matter halo. Such turbulent motions may transfer energy from large to smaller scales (*e.g.* Sarazin 2002; Cassano & Brunetti 2005; Subramanian et al. 2006; Brunetti & Lazarian 2007).

This idea is mainly supported by the results of numerical simulations of cluster mergers (*e.g.* Roettiger et al. 1999b; Ricker & Sarazin 2001; Takizawa 2005; Dolag et al. 2005; Vazza et al. 2006; Vazza et al. 2010a), which provide a detailed description of the gas dynamics in response to such high energetic events.
Recently, thanks to high-resolution simulations of galaxy clusters extracted from large cosmological volumes (*e.g.* Dolag et al. 2005; Vazza et al. 2006), it has been found that turbulent motions can account for $\sim$ 10–30 percent of the total pressure in the ICM (Nagai et al. 2007; Iapichino & Niemeyer 2008; Lau et al. 2009; Vazza et al. 2009; Paul et al. 2011). Similar estimates are also obtained from semi-analytical calculations (*e.g.* Cassano & Brunetti 2005, Vazza et al. 2006).

Unfortunately, the current instrumentation does not allow to directly probe and measure turbulence in galaxy clusters. Observationally, the presence of turbulent gas motions in the ICM is suggested by measurements of the Faraday Rotation of the polarization angle of the synchrotron emission from cluster radio galaxies. These studies show that the magnetic field in the ICM is tangled on a broad range of spatial scales (*e.g.* Murgia et al. 2004; Vogt & Enßlin 2005; Bonafede et al. 2010; Govoni et al. 2010) suggesting the presence of super-Alfvénic motions in the medium.
Other hints of the existence of turbulent motions come from X-ray observations of a number of nearby clusters. A signature of mildly supersonic turbulence has been revealed by the spatially resolved pseudo-pressure image of the Coma cluster, obtained by Schuecker et al. (2004) from high sensitivity X-ray XMM-Newton observations. An indirect observational indication for turbulent motions comes from

the lack of evidence for resonant scattering effects in the X-ray spectra (*e.g.* Henry et al. 2004; Churazov et al.2004).

Recently, important constraints on the fraction of the turbulent and thermal energy in the cores of clusters are based on the analysis of the broadening of the lines in the emitted X-ray spectra with *XMM*-Newton of cool core clusters (Churazov et al. 2008; Sanders et al. 2011). In several cases these studies derived interesting upper limits to the ratio of turbulent and thermal energy, of the order of ≤ 20 per cent, yet they are limited to compact cores in cool core, relaxed, clusters, where turbulence is not driven by cluster mergers. These limits are consistent with expectations in simulated, *non merging*, galaxy clusters (Vazza et al. 2010b).

1.9   Origin of diffuse cluster scale radio emission

The existence of Mpc scale diffuse steep spectrum radio emission of synchrotron origin in clusters of galaxies as giant radio halos and relics implies the presence of relativistic electrons ($\gamma \sim 10^4$) and $\sim \mu G$ magnetic fields in the ICM. Their large linear size rises a problem about the origin of relativistic radiating particles, since they lose energy over timescales much shorter than the particle diffusion time required to cover their Mpc extent. This is a long-standing problem, known as *diffusion problem* (Jaffe 1977). Relativistic electrons lose energy mainly via synchrotron emission and IC scattering of the CMB photons, thus their radiative lifetime is given by (*e.g.* Longair 1981):

$$\tau \approx \frac{2 \times 10^{12}}{\gamma_L} \left[(1+z)^4 + \left(\frac{B^2}{(3.25 \mu G)^2} \right) \right]^{-1} yrs. \tag{1.5}$$

where γ_L is the electron Lorentz factor and B is the magnetic field intensity in μG. For electrons emitting synchrotron radiation around ~ 1 GHz, the typical life-time is $\approx 10^8$ yr. Since their expected diffusion velocity is of the order of ~ 100 km/s (the Alfvén speed), electrons do not have enough time to propagate over the observed $\sim$ Mpc scale of giant cluster radio sources.

This implies that the electrons responsible for the radio emission must be accelerated everywhere in the cluster.

Shock waves and/or turbulence induced during cluster mergers may accelerate or re-accelerate relativistic particles (protons and electrons) in the cluster volume. The growing observational evidence of connections between the diffuse non-thermal radio

emissions and cluster mergers (Sec. 1.8) supports this idea. In particular, merger shocks (Sec. 1.8.1) can efficiently accelerate supra-thermal particles in the ICM up to relativistic energies, via Fermi-I processes (*e.g.* Ryu et al. 2003), or re-accelerate pre-existing relativistic particles due to adiabatic compression, and are believed to be at the basis of the models for the origin of peripheral radio relics (Sect. 1.9.2). Merger-driven turbulence may re-accelerate fossil relativistic plasma mixed with the thermal one on Mpc scales, through less efficient Fermi-II processes, giving rise to the observed extended radio halos (*e.g.* Brunetti 2003, 2004; Sect. 1.9.1).

1.9.1   Origin of Radio Halos and the turbulent re-acceleration model

The diffusion problem leads to the requirement that the electrons responsible for the radio halo emission must be continuously injected or accelerated everywhere in the cluster. So far two main possibilities have been proposed to explain the origin of radio halos, based on different origin of the radiating electrons:

1. the "re–acceleration model", whereby radio halos originate from the in–situ re–acceleration of pre–existing electrons by magneto–hydrodynamic (MHD) turbulence injected in the ICM during cluster mergers (*e.g.* Brunetti et al. 2001; Petrosian 2001);

2. "secondary electron models", predicting that relativistic electrons are injected in the cluster volume by hadronic collisions between relativistic cosmic ray protons and the thermal ions of the ICM (*e.g.* Dennison 1980; Blasi & Colafrancesco 1999). The inelastic hadronic collisions produce charged pions, which in turn decay and inject secondary electrons and positrons into the ICM. Since the relativistic protons are long-living particles (with radiative lifetime of the order of the Hubble time), the large extent of radio halos emission may be explained without invoking any (re)-acceleration process.

Although the origin of halos is still debated, present observations support the first scenario, and disfavour a secondary origin for the emitting particles.
The main observational evidence against secondary models is the fact that radio halos have been observed up to now in merging clusters only. A strong connection between cluster mergers and radio halos is a natural consequence of the re-acceleration model, since it assumes that MHD turbulence is injected during cluster

mergers, while such connection is not expected in secondary models. Moreover, observations have shown that radio halos are *rare* phenomena, since they are presently observed only in ~ 30 % of massive and X-ray luminous merging clusters (see Sec. 1.5). This is again disfavouring the hadronic collision hypothesis. Since all clusters have experienced mergers, and relativistic protons are mostly confined within the clusters, we should expect to observe extended radio emission in almost all galaxy clusters (Blasi et al. 2007).

Another piece of evidence in favour of the re-acceleration models comes from the observation of the high frequency cut-off in the spectra of a number of radio halos (*e.g.* Coma-C, Thierbach et al. 2003; A521, Brunetti et al. 2008, Dallacasa et al. 2009; see Sect. 1.5). This feature is expected by the the re-acceleration model, since stochastic particle acceleration is an inefficient (Fermi II) process. In this case, the competition between acceleration and energy losses limits the maximum energy of the accelerated electrons at $\gamma \sim 10^4$, implying the presence of an high frequency cut-off in the spectrum of radio halos. Finally, gamma-ray emission at the limit of *FERMI* sensitivity is also predicted in this context from the π_0 decay generated from hadron collisions (Blasi et al. 2007, Donnert et al. 2010). To date gamma ray observations did not detect emission from galaxy clusters, and upper limits only have been placed (*e.g.* Reimer et al. 2003; Aharonian et al 2009a; 2009b; Ackermann et al. 2010).

1.9.2 Models for the origin of Radio Relics

At present, theoretical models for the origin of radio relics imply a connection between these sources and the presence of merger shock waves propagating through the intracluster gas.

Two main scenarios have been proposed to explain the origin of radio relics.

Diffusive Shock Acceleration

In these models, first proposed to explain the formation of radio relics, the radio emitting electrons are accelerated up to relativistic energies directly from the ICM thermal pool, through Fermi-I diffusive shock acceleration (Enßlin et al. 1998; Roettiger et al. 1999a; Hoeft & Brüggen 2007).

In the case of a fully ionized plasma as the ICM, the spectrum of the electrons

accelerated by the shock is a power law in energy $N(E) \propto E^{-p}$, whose slope p is related to the shock Mach number M according to the following equation:

$$p = 2\frac{M^2 + 1}{M^2 - 1} + 1 \tag{1.6}$$

(*e.g.* Blandford & Eichler 1987), where the effect of particle aging $\Delta(p) = 1$ is included. The spectral index of the resulting radio emission $\alpha = (p - 1)/2$ is thus related to the Mach number of the shock.

If the shocks driven during mergers are weak (*i.e.,* $M \lesssim 3$), as suggested by semi-analytical calculations and numerical simulations (see Section 1.8.1), they are expected to produce steep particle spectra, which may be consistent with the steep integrated spectra observed in radio relics (Section 1.6). Once accelerated by the shock, the electrons are short-lived because of they lose energy via IC and synchrotron emission, and thus their spectrum will quickly steepen. In this case, it is expected that the spectral index distribution of the radio emission in relics exhibits a steepening going from the current shock location (where the observed is the electron injection spectral index) to the trailing edge (in the observer projection; Enßlin et al. 1998). Furthermore, it is expected that the shock may cause the magnetic field to become aligned with the shock plane. This may explain the high levels of polarization in radio relics, since it implies that even an originally isotropic distribution of magnetic fields would exhibit a preferred orientation after the shock crossing, which rearranges and orders the field topology (generating polarized signal).

Adiabatic compression

An alternative model for the relic origin is the adiabatic compression of fossil radio plasma as result of the passage of a merger shock (Enßlin & Gopal-Krishna 2001). Such fossil radio plasma may be the former outflow of a radio galaxy in which the central engine of the AGN has ceased to inject fresh relativistic plasma. The high energy electrons, related to the previous AGN activity, have suffered for major energy losses due to Inverse Compton and synchrotron radiation, and are able to produce radio emission only below the detectable limit with the current radio instrumentation, which may be eventually detected at very low frequencies (tens of MHz). For this reason, these cocoons of aged radio plasma are also called radio

ghosts (Enßlin 1999). When a radio ghost is crossed by a merger shock wave, propagating with a typical velocity of few 1000 km s^{-1}, the cocoon is compressed adiabatically and not shocked because of the much higher sound speed within it (the cocoon is supposed to be made of relativistic particles). Enßlin & Gopal-Krishna 2001 proposed that such compression may increase the magnetic field strength and re-energize the electron population in such fossil radio plasma, thus leading to synchrotron emission observable at decimeter wavelenghts. In this case the pre-existing relativistic electrons are expected to produce diffuse radio emission in front of the bow shock, and then rapidly lose their energy while moving away from the front. Hence a steepening in the spectral index distribution of the relic is expected also in this scenario. The numerical magneto-hydrodynamical simulations by Enßlin & Brüggen (2002) of a fossil radio cocoon crossed by a shock wave predict a variety of radio morphologies and polarization properties, which may be reasonably well matched by the available high sensitivity radio images of cluster radio relics. An important requirement in this scenario is that the electron population is not older than $\sim 0.2 - 2$ Gyr (Enßlin & Gopal-Krishna 2001), and therefore the presence of an active radio galaxy in the proximity of the relic is required. On the other hand, a strong requirement of this scenario, that typically disfavours it with respect to shock acceleration model, is that the cocoon of relativistic particles must be confined (not mixed) in the thermal ICM for a long time ($0.2 - 2$ Gyr).

Chapter 2

The GMRT Radio Halo Survey and statistics of radio halos

In this chapter we summarize the main characteristics and results of the GMRT Radio Halo Survey. The whole observational project is presented in Venturi et al. 2007 and 2008. The GMRT Radio Halo Survey is the starting point of the present thesis, that is mostly devoted at low frequency follow up observations of clusters in the GMRT radio halo cluster sample.

2.1 The Giant Metrewave Radio Telescope

The Giant Metrewave Radio Telescope (GMRT) is currently the world largest radio interferometer fully operating at meter wavelengths. It is operated by the National Centre for Radio Astrophysics (NCRA) of the Tata Institute of Fundamental Research (TIFR, India) and is located at ~80 km North of Pune. The instrument is an aperture synthesis array, composed of 30 fully steerable parabolic dishes of 45 m diameter each (see Fig. 2.1): 14 antennas are located in a compact central array, covering a region of about 1 km^2, and 16 are distributed along three arms to form an approximately Y-shaped configuration, with a longest baseline of ~25 km.

The array currently operates in five frequency bands centered around 150, 235, 325, 610 and 1420 MHz. The main system parameters are summarized in Table 2.1. At each frequency, two simultaneous observing bands are provided, namely the upper side band (USB) and lower side band (LSB), with a bandwidth of 16 MHz each at 325, 610 and 1420 MHz and 8 MHz at 235 and 150 MHz. Simultaneous dual-frequency observations are possible at 235 and 610 MHz, with an 8 MHz bandwidth at each frequency. Dual polarization information (right RR and left LL) is provided

at all frequencies. When the array observes in simultaneous mode at 235/610 MHz, LL polarization is recorded at 235 MHz, and RR at 610 MHz. The GMRT u-v coverage ensures a good sensitivity both to compact and extended sources. Hence, a single observation with the GMRT samples the u-v plane adequately on the short as well as on the long baselines, thus providing high sensitivity imaging over a wide range of angular resolutions (Tab. 2.1). Therefore GMRT is a very suitable instrument to study diffuse, low surface brightness and steep spectrum radio sources such as cluster scale radio halos and relics (Sec. 1.4.1). The possibility to obtain both high resolution (few arcsec) and low resolution (few tens of arcsec) images at all frequencies allows to discriminate between real diffuse emission and a blend of individual radio galaxies, and to detect and remove the possible contribution of discrete radio sources embedded in the halo/relic emission.

Table 2.1: Main GMRT parameters

	Frequency (MHz)				
	151	235	325	610	1420
Primary Beam (arcmin)	186	114	81	43	24
HPBW whole array (arcsec)	20	13	9	5	2
HPBW Central Compact Array (arcsec)	420	270	200	100	40
Largest Detectable Structure (arcmin)	68	44	32	17	7
Best rms sensitivity acheived presently known (mJy b^{-1})	0.7	0.25	0.04	0.02	0.03

Note: See www.ncra.tifr.res.in/~gtac/GMRT-specs.pdf for a more detailed description of the current system parameters (as of December 2010).

2.2 The GMRT Radio Halo Survey

The study of the statistical properties of radio halos, such as their distribution in redshift, occurrence in clusters and connection with cluster thermal properties and dynamics, is crucial to understand the origin and evolution of these sources. A first observational attempt to study the statistical properties of radio halos at z ≤ 0.2 has been obtained by means of deep follow-up imaging with the VLA at 1.4 GHz of candidate radio halos identified on the NVSS (Condon et al. 1998) and WENSS (Rengelink et al. 1997) radio surveys (Giovannini et al. 1999; Kempner & Sarazin 2001; Feretti 2003, for a review). A step forward was more recently achieved through
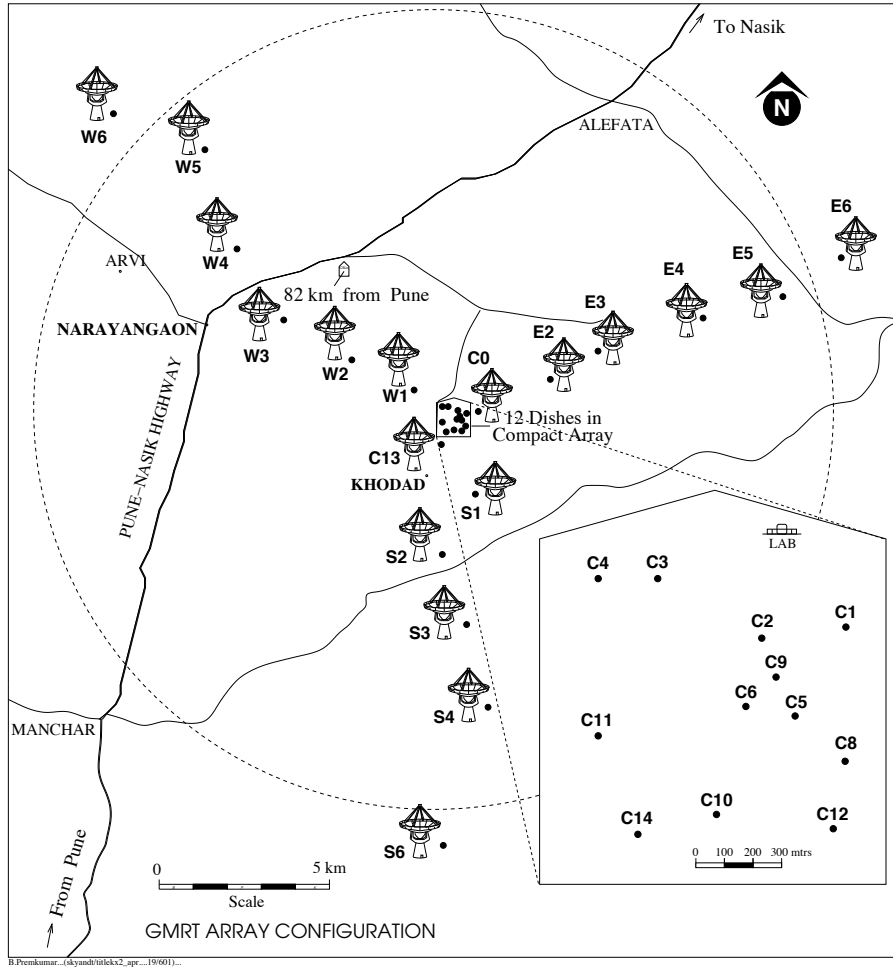
Figure 2.1: Location of the GMRT antennas.

a project carried out with the GMRT at 610 MHz, the "GMRT Radio Halo Survey" (Venturi et al. 2007; 2008).

The GMRT Radio Halo Survey was designed to measure the fraction of massive clusters hosting a radio halo and to highlight possible trends of this fraction with the cluster mass. The final aim of the survey was to investigate the connection between cluster mergers and the presence of diffuse cluster sources, and to test predictions of models for the origin of radio halos. In particular, Monte Carlo simulations based on the turbulent re-acceleration model have shown that the the bulk of giant radio halos should be generated in the redshift interval z = 0.2–0.4, where ~35% of massive (*i.e.,* M > 10^{15} M$_\odot$) clusters may host one.

The GMRT Radio Halo Survey thus represents the first approach to investigate the origin of radio halos and their occurrence rate by means of the study of a statistically

sound sample.

2.2.1 Selection criteria and the cluster sample

The galaxy cluster sample consists of 50 clusters which have been selected from the REFLEX (Böhringer et al. 2004) and eBCS (Ebeling et al. 1998 and 2000) X-ray cluster catalogues, according to the following criteria:

- $0.2 \leq z \leq 0.4$;

- $L_{X[0.1-2.4\text{keV}]} \geq 5 \times 10^{44}$ erg s^{-1}

- $-30^{\circ} \leq \delta \leq +2.5^{\circ}$ for the REFLEX catalogue, and $+15^{\circ} \leq \delta \leq +60^{\circ}$ for the eBCS catalogue.

The redshift range and the limit in X-ray luminosity were chosen to optimize the information requested to perform the statistical analysis. The former choice was made to complete the statistical information already available for $z \leq 0.2$ (Giovannini et al. 1999, see Sec. 1.5). Moreover, assuming the L_X–M_V correlation in Cassano et al. 2006, the adopted limit in L_X corresponds to a virial mass limit of $M_V \geq 1 - 1.5 \times 10^{15}$ M$_{\odot}$. This is the threshold above which: *(i)* substantial fraction of clusters are expected to host a radio halo (according to the re-acceleration model; *e.g.* Cassano et al. 2006); *(ii)* the expected radio halo luminosity (based on the $P_{1.4}$–L_X correlation; see Sect. 1.5; *e.g.* Giovannini & Feretti 2002) is well above the detection threshold of the pointed ∼2–4 hours GMRT observations at 610 MHz (see Sec. 2.2.2). The declination limits were imposed in order to ensure a good u-v coverage with the GMRT.

27 clusters were selected from the REFLEX catalogue and 23 from the eBCS catalogue. Among these, 7 clusters had a known radio halo, and other 9 either were part of the GMRT Cluster Key Project or had archival deep VLA observations. Thus GMRT observations at 610 MHz were carried out for 34 clusters, *i.e.,* those with no previous high sensitivity radio observations available.

2.2.2 Observations

The survey was performed during three different observing runs (January and October 2005, August 2006), for a total of ∼100 hours of observations. The choice of the GMRT was motivated by the observational evidence that diffuse cluster radio

emission is characterized by steep radio spectrum and very low surface brightness (Sect. 1.4.1). Thus an instrument capable of high sensitivity at low frequency as the GMRT was appropriate to the survey goals (Sec. 2.1). The survey was carried out at 610 MHz, since this frequency provides a fairly good sensitivity to extended diffuse emission: the largest detectable scale of $\sim 17'$ (Tab. 2.1) allows to properly detect giant radio halos in the selected redshift range. Moreover, the highest angular resolution ($\sim 5''$; Tab. 2.1) of the GMRT at this frequency allows to minimize the confusion.

Each of the 34 clusters was observed for $\sim$2.5–4 hours, and the typical noise in the images is of the order of 40-80 μJy beam^{-1}.

2.3 Main results of the GMRT Radio Halo Survey

The GMRT Radio Halo Survey, combined with the available information for clusters at lower redshift, allowed the investigation of the properties of radio halos on a solid statistical basis.

The survey observations turned out to be highly successful, with the discovery of three new radio halos, one cluster hosting both a radio halo and a double relic, one radio relic, and one mini-halo source. Moreover, four candidate diffuse sources have been found. More details on these sources and the host cluster are reported in Tab. 2.2.

Table 2.2: Results of the GMRT Radio Halo Survey: halos, relics and candidates.

Cluster	z	Source Type	$S_{610\text{MHz}}$ mJy
A 209	0.2060	Giant Halo	24±3.6
A 697	0.2820	Giant Halo	13.0±2.0
RXCJ2003.5–2323	0.3171	Giant Halo	24±3.6
RXCJ1314.4-2515	0.2439	Halo + 2 Relics	24±3.6
A 521	0.2475	Relic	41.9±2.1
Z 7160	0.2578	Mini-Halo	43.6±2.2
A 781	0.2984	Candidate Relic	32±2.0
Z 2661	0.3825	Candidate Halo	~5.9
A 1682	0.2260	Candidate Halo	~44
A 3444	0.2542	Candidate Mini-Halo	10±0.8

The new GMRT detections of radio halos, combined with the literature information, brought to 10 the number of clusters with a radio halo in the total sample.

However, in the great majority of the observed clusters (25/34), no diffuse emission was detected, and upper limits to the clusters radio luminosity of a putative radio halo were derived for all these cluster.

The main results related to the survey are summarized in the following.

- **Statistics of radio halos**

  The GMRT radio halo survey confirmed that diffuse cluster-scale radio emission is not ubiquitous in clusters (Sect. 1.5): the fraction of clusters in the GMRT sample with a central radio halo is ∼30%. By combining these results with the information from the NVSS for the clusters at redshift z < 0.2 (Giovannini et al. 1999), Cassano et al. (2008) performed an unbiased estimate of the occurrence of radio halos in a large sample of clusters in the redshift range 0–0.4. They found the first statistical evidence (at the 3.7σ level) that the fraction of clusters with radio halos increases with the cluster X-ray luminosity (and mass), from $\approx 10\%$ to $\approx 40\%$, considering the luminosity ranges $4 \times 10^{44} \lesssim L_X \lesssim 8 \times 10^{44}$ erg s^{-1} and $L_X \gtrsim 8 \times 10^{44}$ erg s^{-1}, respectively. This increase of the fraction of clusters with radio halos with the cluster mass can be explained in the framework of the re-acceleration scenario, since energy arguments imply that particle acceleration is more efficient in more massive (and X-ray luminous) clusters that undergo energetic merger events (Cassano et al. 2008; Sect 1.9.1).

- **$P_{1.4}$-L_X correlation and cluster radio bimodality**

  Beyond the positive detections, the survey allowed to place reliable upper limits to the non detections for 20 clusters (by means of the *"fake radio halos procedure"*, Brunetti et al. 2007; Venturi et al. 2008; see also Sec. 3.5.1). Once reported in the $P_{1.4}$-L_X diagram, the clusters of the GMRT radio halo sample show a bimodal behaviour: clusters with radio halos follow the well known correlation (Cassano et al. 2006; Sect. 1.5), while all the upper limits to the radio power of clusters without radio halos populate the bottom part of the diagram, lying more than 1 order of magnitudes below the correlation

(Brunetti et al. 2007; see Fig. 2.2).

This result has very important implications on the origin of radio halos. The observed bimodality suggests a "transient" nature of radio halos. In particular, the lack of clusters in the region between "radio halo" and "non-radio halo" (upper limits) clusters, indicates that, if the radio properties of clusters evolve with time, this evolution should be fast, on a timescale of a fraction of Gyr (Brunetti et al. 2007). The constrains put on the evolution of radio halos (and their connection to cluster mergers; see below) provide an important test for models of halo formation. The radio bimodality is indeed a natural consequence of models invoking particle acceleration in connection to cluster mergers (*e.g.* the turbulent re-acceleration models). On the other hand, it represents a challenge for secondary models (Sec. 1.9.1; see *e.g.* Brunetti 2009)[1].
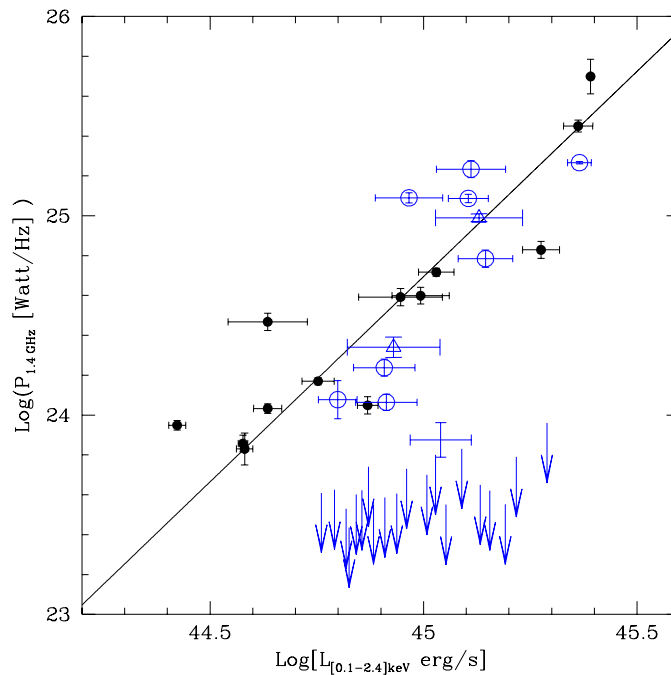
Figure 2.2: Distribution of galaxy clusters in the $P_{1.4}$-L_X plane. Filled black dots are clusters with radio halos known from the the literature, empty blue dots are the radio halos from the GMRT cluster sample. The solid line is the $P_{1.4}$-L_X correlation (from Cassano et al. 2006). Upper limits (represented by the blue arrows) are GMRT clusters with no hint of cluster-scale emission. From Brunetti & Cassano 2010.

---

[1]Enßlin et al. (2011) have recently proposed cosmic rays streaming to attempt to reconcile these models with observations.

Figure 2.3: Power ratio P_3/P_0 versus the concentration parameter c. Symbols are: radio halos (red filled dots), no-radio halos (black open dots), mini-halos (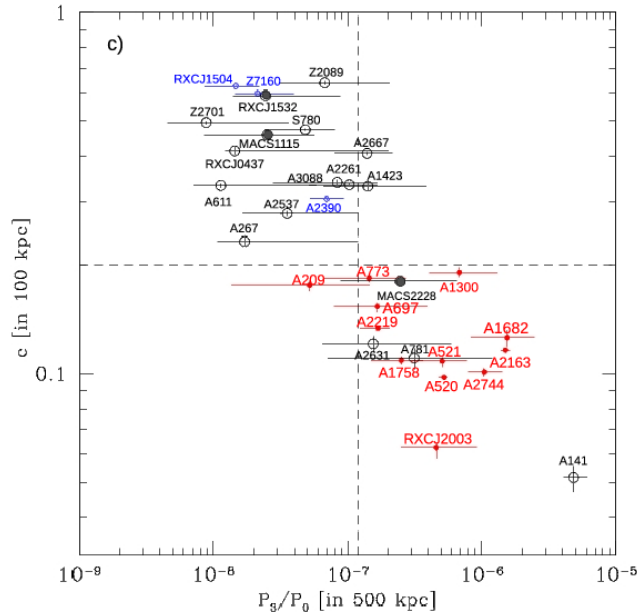blue open dots), z >0.32 (gray filled dots). Vertical and horizontal dashed lines are: $c = 0.2$ and $P_3/P_0 = 1.2 \times 10^{-7}$. From Cassano et al. 2010b.

- **Radio halo - cluster merger connection**

  Another important result of the survey is the confirmation of a tight connection between the presence of radio halos and the dynamical activity of the host clusters. A correlation between the radio halo luminosity at 1.4 GHz and the dynamical state of the cluster (expressed by the magnitude of the dipole power ratio P_1/P_0) was first found by Buote (2001). A similar analysis performed for a number of clusters of the GMRT sample with available X-ray information led to the result that all clusters hosting halos, relics and candidate diffuse emission show signature of dynamical activity (Venturi et al. 2008).

  To test the radio halo-cluster merger connection, Cassano et al. (2010b) recently combined the radio data from the GMRT survey with X-ray data of 32 clusters of the GMRT sample for which archive *Chandra* observations were available. For the first time it has been found that the cluster radio bimodality has a clear correspondence in terms of cluster dynamics: radio halo clusters are found in dynamically disturbed systems, while cluster without radio halo are more "relaxed" , with only a couple of outliers of disturbed cluster with no

radio halo (see Fig. 2.3).

- **Discovery of ultra steep spectrum radio halos: the case of Abell 521**

  The GMRT Radio Halo Survey provides a first step towards the exploration of cluster diffuse radio emission at low frequencies. A natural evolution in this direction has been a campaign of deep follow-up observations at low frequency with the GMRT, to better investigate the spectral properties of the new discovered diffuse radio sources and to confirm the presence of candidates (Venturi et al. 2009; Venturi et al. 2011 to be submitted). In particular, GMRT observations at 240 and 330 MHz of the merging cluster A 521, aimed to study the spectral properties of the peripheral radio relic source observed at 610 MHz (Giacintucci et al. 2008), led to the discovery of a giant radio halo at its center, which was only barely detected at 610 MHz (left panel of Fig. 2.4; see also Sect. 4.2). The integrated spectrum turned out to be very steep ($\alpha \sim 2$; right panel of Fig. 2.4), much steeper than the typical spectra of previously known radio halos found at higher frequency (Brunetti et al. 2008; Dallacasa et al. 2009). The source is now considered the prototypical example of the "class" of "ultra steep spectrum radio halos" (USSRH; see Sect. 2.4), whose existence is a unique prediction of the turbulent re-acceleration model.

2.4 Statistical expectations of the re-acceleration model at low frequency

In the framework of the turbulent re-acceleration models, the process of formation and evolution of radio halos in galaxy clusters is tightly connected with the formation and evolution of the host clusters (Sect 1.9.1).

The existence of a population of radio halos with very steep spectra, referred to as "ultra steep spectrum radio halos" (USSRH), is one of the most important predictions of these models. Since stochastic particle acceleration by MHD turbulence is a rather inefficient process in the ICM, electrons can be accelerated only up to energies of $m_e c^2 \leq$ several GeV, while at higher energies the radiation losses become more efficient and limits the acceleration process. The resulting spectral steepening expected in the synchrotron spectrum makes it difficult to observe these
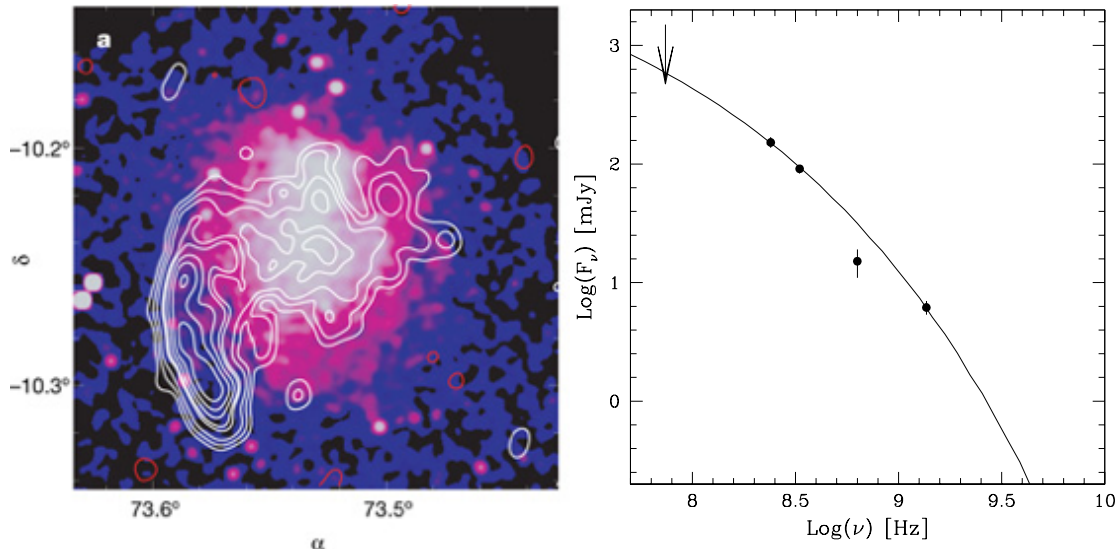
Figure 2.4: *Left* – GMRT 240 MHz contours of the USSRH and relic in A 521, overlaid to the *Chandra* image. *Right* – integrated radio spectrum of the USSRH (filled dots and upper limit). The solid curve is the re-acceleration model. From Brunetti et al. 2008 and Dallacasa et al. 2009.

Figure 2.5: Picture showing the connection between acceleration efficiency and spectrum of Radio Halos in the re-acceleration scenario. From Brunetti 2009.

sources at frequencies higher than the cut-off frequency ν_c, at which the steepening becomes severe (see Fig. 2.5, where spectra of radio halos are schematically shown). The value of ν_c is essentially determined by the acceleration efficiency,

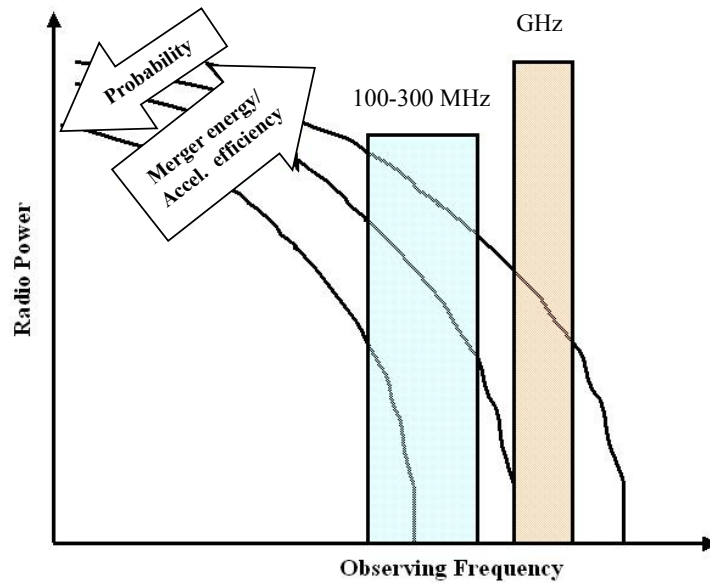which basically increases with the level of turbulence in the ICM. This is ultimately determined by the energetics of the merger events. Higher values of ν_c ($\nu_c > $ GHz) are expected in the more massive clusters undergoing major merger events. Less energetic merger events (*e.g.* major mergers between less massive systems or minor mergers in massive systems) are expected to generate radio halos with lower ν_c, that should thus glow up when observed at low frequencies (Fig. 2.5). Moreover, since less energetic mergers are expected to be more frequent, these low frequency radio halos are also expected to be more numerous than those commonly observed at GHz frequencies (Fig. 2.5). When observed at frequencies $\nu_{obs} < \nu_c$, radio halos should have very steep spectra (Fig. 2.5), with $\alpha > 1.5$, and are referred to as "ultra steep spectrum radio halos" (USSRH). Although radio halos with $\nu_c < 1$ GHz are expected to be relatively common, they are also less powerful than the presently known GHz radio halos. Thus deep low frequency observations are needed to test these predictions (*e.g.* Brunetti 2009; Cassano 2009; Cassano 2010).

Chapter 3

The very steep spectrum radio halo in Abell 697[*]

3.1 Introduction

As pointed out in Sec. 1.9.1 the analysis of the integrated spectrum of cluster radio halos is crucial to address the question of their origin. The turbulent re–acceleration model (Sec. 1.9.1) provides the unique expectation of radio halos with spectra much steeper than those found to date (USSRHs, *i.e.,* $\alpha > 1.5$; Sec. 2.4). Thus the detection of these USSRHs would be a major piece of evidence in support of this scenario. At the same time it would disfavour a secondary origin of the relativistic electrons, due to energy arguments (e.g. Brunetti 2004; see also this Chapter, Section 3.6).

In this chapter we present a detailed study of the merging cluster A 697, which hosts a candidate steep spectrum radio halo. We study its integrated radio spectrum, using high sensitivity GMRT observations at 325 MHz, previous proprietary GMRT observations at 610 MHz, and data from the VLA public archive at 1.4 GHz. We then discuss our results in the framework of the models for the origin of radio halos.

3.2 The cluster Abell 697

A 697 is a rich and massive ACO (Abell, Corwin and Olowin) galaxy cluster (Abell et al. 1989) located at z=0.282. The cluster is hot and luminous in the X–ray band, and is part of the ROSAT Brightest Cluster Sample (BCS; Ebeling et al. 1998). Its general properties are summarized in Table 3.1, which provides: coordinates;

---

[*]Macario et al. 2010, A&A, 517, 43

Table 3.1: General properties of the galaxy cluster A 697.

RA$_{J2000}$	08h 42m 53.3s
DEC$_{J2000}$	+36° 20′ 12″
Bautz–Morgan Class	II–III
Richness	1
z	0.282
σ_v	1334 km s^{-1} (a)
L$_{X[0.1-2.4keV]}$	10.57 × 10^{44} erg s^{-1}
T$_X$	10.2±0.8 keV (a)
M$_V$	2.25 × 10^{15} M$_\odot$ (b)
R$_V$	2.90 Mpc (b)

Notes to Table 3.1: (a): Girardi et al. 2006; (b): Estimated from the L$_X$–M$_V$ relation, see Eq. 6 and 7 in Cassano et al. (2006).

morphological classification of the cluster and richness; redshift z; cluster velocity dispersion σ_v (from optical spectroscopy); X–ray luminosity L$_X$ (taken from the BCS catalogue); cluster X-ray temperature T$_X$; virial mass M$_V$ and the corresponding virial radius R$_V$.

The presence of diffuse cluster–scale radio emission in A 697 was first suggested in Kempner & Sarazin (2001) by inspection of the NVSS and the WENSS, and further confirmed by GMRT observations at 610 MHz as part of the GMRT Radio Halo Survey (Sect. 2.2; Venturi et al. 2007; 2008). From those observations the extended radio emission at the cluster centre has been unambiguously classified as a giant radio halo.

At the redshift of A 697 (z=0.282), the cosmology adopted in this work leads to a linear scale of 1″ = 4.26 kpc.

3.3   GMRT radio data at 325 MHz

3.3.1   Radio observations and data reduction

A 697 was observed at 325 MHz with the GMRT (Section 2.1), as part of the GMRT radio halo survey low frequency follow up (Venturi et al. 2009, Venturi et al. 2011, to be submitted; see also Sect. 2.3). The main characteristics of the 325 MHz observations are summarised in Table 3.2, which reports: observing date, frequency, total bandwidth, total time on source, half power beamwidth (HPBW), rms level (1σ) at full resolution and u–v range of the full dataset.

The observations were carried out using simultaneously the upper and lower

side bands (USB and LSB, respectively), for a total observing bandwidth of 32 MHz. The default spectral–line observing mode was performed, with 128 channels for each band and a spectral resolution of 125 kHz/channel. The USB and LSB datasets were calibrated and analyzed separately using the NRAO Astronomical Image Processing System package (AIPS).

Due to the considerably lower quality of the LSB (strong RFI residuals), only the USB data were used to produce the final images presented and analysed in this work.

The very large field of view of the GMRT at 325 MHz (primary beam $\sim$ 1.8°) required the implementation of the wide–field imaging technique in each step of the phase self–calibration process, in order to account for the non–planar nature of the sky. We covered the field of view ($\sim 2.7 \times 2.7$ square degrees) with 25 facets.

Even though only half of the full dataset was usable, the quality of the final image is very good: the rms ranges from $\sim 45~\mu$Jy b^{-1} in the central region around the halo to $\sim 55~\mu$Jy b^{-1} in the outer parts of the field. The residuals amplitude errors are $\lesssim 5\%$.

Table 3.2: Summary of the GMRT radio observations.

Observation date	ν (MHz)	$\Delta\nu$ (MHz)	t (min)	HPBW, p.a. (full array , $''\times''$, °)	rms (μJy b^{-1})	u–v range (kλ)
17 Jan 2007	325	32(16)*	480	10.0×9.1, -64	45	∼0.08-25

Notes to Table 3.2: * The observations were performed using a total bandwidth of 32 MHz (USB+LSB), but only the USB dataset was used for the analysis (see Sect. 3.3.1)

3.3.2 The field

In Fig. 3.1 we report the 325 MHz GMRT full resolution contours of the central $12' \times 12'$ ($\sim 3 \times 3$ Mpc^2) portion of the A 697 field. The region corresponds to half of the cluster virial radius ($R_V = 2.9$ Mpc, Table 3.1).

The most prominent features at this resolution are the two extended radio galaxies, labelled as S1 and S2 in Fig. 3.1, located South of the cluster centre. In addition, the diffuse radio emission associated with the radio halo is clearly visible around the cluster centre. The positive residuals surrounding the central diffuse emission indicate that this source is quite extended.
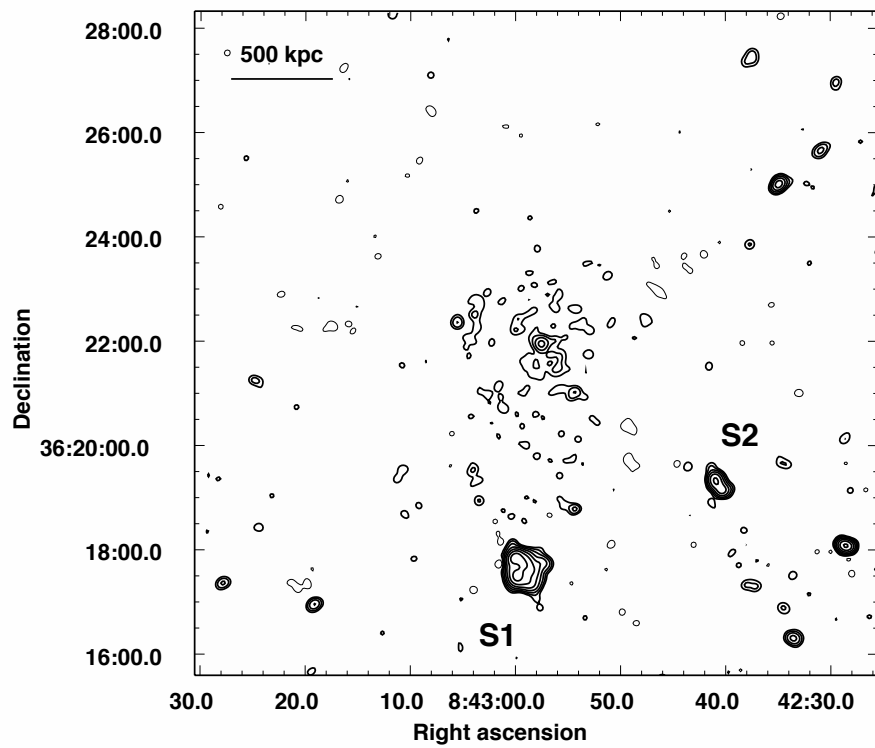
Figure 3.1: GMRT 325 MHz radio contours of the inner $12' \times 12'$ region centered on A 697. The 1σ level in the image is 45 μJy b^{-1}. Contours are spaced by a factor 2 starting from $5\sigma = \pm$ 0.225 mJy b^{-1}. The HPWB is $10.0'' \times 9.1''$, p.a. $-64°$. The labels S1 and S2 indicate the two extended radio galaxies in the Southern part of the cluster.

Table 3.3: Individual radio galaxies at the center of A 697.

Radio source	Radio position RA$_{J2000}$ & DEC$_{J2000}$	S$_{325\,MHz}$ mJy	Optical Position RA$_{J2000}$ & DEC$_{J2000}$	z
A	08 42 57.70 +36 22 01	4.63±0.23	08 42 57.55 +36 22 00	0.281
D	08 42 54.54 +36 21 05	1.97±0.10	08 42 54.36 +36 21 03	0.274
G	08 43 05.65 +36 22 25	1.36±0.07	08 43 05.50 +36 22 24	0.267

3.3.3   The radio halo

Fig. 3.2 zooms into the radio halo. The left panel shows the full resolution 325 MHz contours (starting from $\pm 3\sigma$), overlaid on the red optical frame from the Digitized Palomar Sky Survey (DSS–2). Three discrete radio sources embedded in the halo emission are optically identified with cluster members (Girardi et al. 2006, hereinafter G06). We labelled them A, D and G, following the same notation used for the corresponding sources identified in the GMRT 610 MHz full resolution image (left panel of Fig. 3.2, see also Venturi et al. 2008). In Table 3.3 we report their radio position and flux density at 325 MHz (obtained from Gaussian fits on the full resolution image), together with their optical identification and redshift (from G06). Source A is identified with the central cD galaxy.

In order to image the diffuse emission of the radio halo, the three sources A, D and G, whose total flux density amounts to S$_{325\,MHz}$ = 7.96 ± 0.26 mJy, were subtracted out of the u–v data. The final "subtracted" dataset was used to produce images of the radio halo at various angular resolutions, tapering the u–v data by means of the parameters `robust` and `uvtaper` in the task IMAGR.

In the right panel of Fig. 3.2 we report the 325 MHz contours of the radio halo at the resolution of 46.8″ × 41.4″, overlaid on a GMRT 610 MHz image of similar resoution (46.4″ × 35.9″; grey scale, see also Venturi et al. 2008). The first contour corresponds to the $\pm 3\sigma$ significance level.

The radio halo of A 697 is very extended at 325 MHz, with a largest angular size (LAS) of $\sim 5.1'$, corresponding to a largest linear size (LLS) of ~ 1.3 Mpc h$_{70}^{-1}$. Its overall morphology is regular and symmetric, and more extended than imaged at 610 MHz. The central $\sim 1'$ is similar at both frequencies, and the bright feature well visible at 610 MHz in the western part of the halo is almost coincident with a
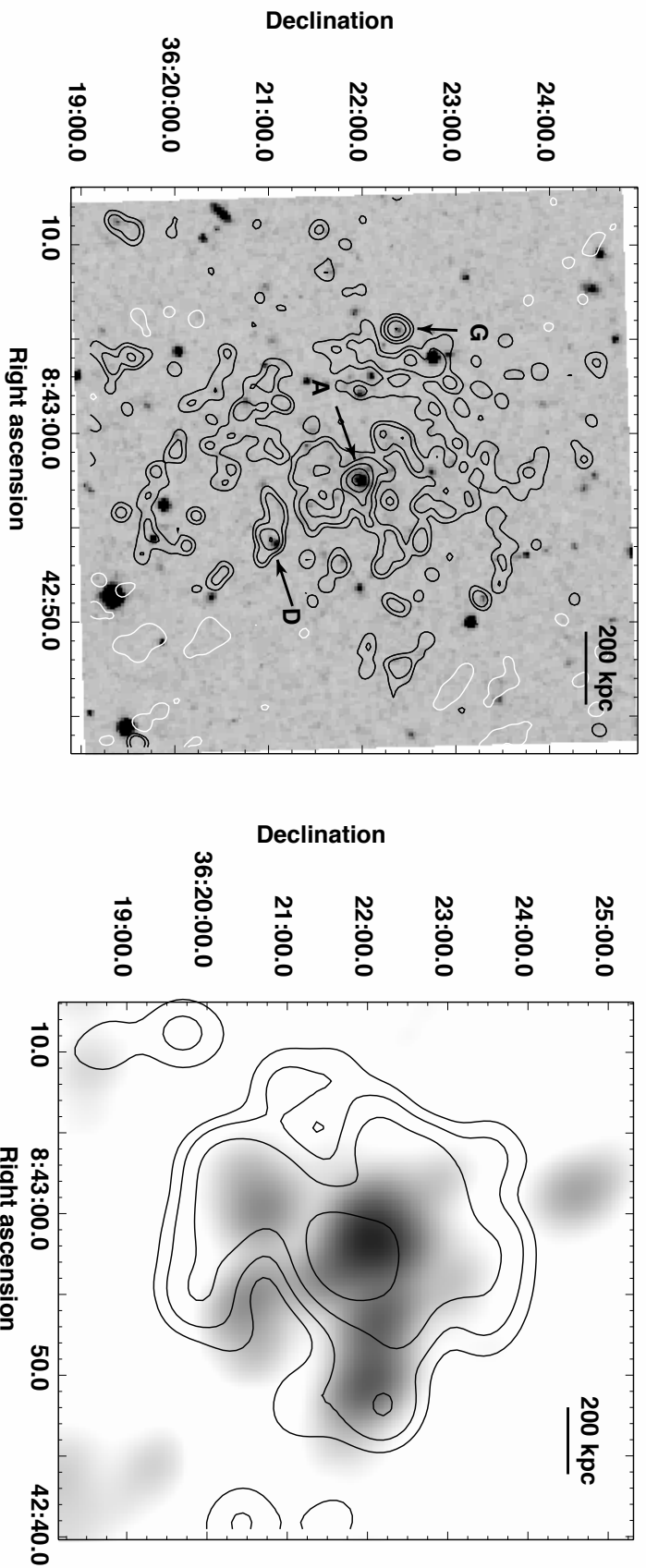
Figure 3.2: *Left* – Full resolution GMRT 325 MHz contours of the central region of A 697, superposed to the POSS–2 optical image. The image is the same as Fig. 1 (10.0″ × 9.1″, p.a. −64°, 1σ level is 45 μJy b⁻¹) and contours are spaced by a factor 2, starting from ± 0.135 mJy b⁻¹ (3σ). Individual radio sources are labelled by letters A, D and G (as in Venturi et al. 2008, Fig. 2). *Right* – Low resolution GMRT image at 325 MHz of the radio halo (obtained after subtraction of the individual sources, see Sect. 3.3.3) overlaid on the GMRT 610 MHz image (grey scale). The resolution of the 325 MHz image is 46.8″ × 41.4″, p.a. 80°, and the 1σ noise level is 150 μJy b⁻¹. Logarithmic contours are shown, starting from ±0.45 mJy b⁻¹. The 610 MHz image has a resolution of 46.4″ × 35.9″, p.a. 42°, and the 1σ noise level is 50 μJy b⁻¹.

similar structure at 325 MHz.

The total integration time of the 610 MHz observations is much shorter than that at 325 MHz (see section 3.3.1), and the u–v coverage of the short spacings is substantially worse. In Fig. 3.3 we report a comparison between the inner portions of the u–v plane at 325 and 610 MHz (left and right panel respectively); visibilities relative to baselines shorter than 1 kλ are shown[1]. For this reason, a detailed spectral index imaging was not carried out.

The total flux density of the radio halo at 325 MHz is $S_{325MHz} = 47.3 \pm 2.5$ mJy (see Sect. 3.5 for a detailed discussion on the uncertainties associated with this value); it was obtained by integrating the low resolution image (Fig. 3.2, right panel) over the region covered by the $\sim 3\sigma$ contour. The corresponding total radio power is $\log P_{325\ MHz}$ (W/Hz)= 25.07.

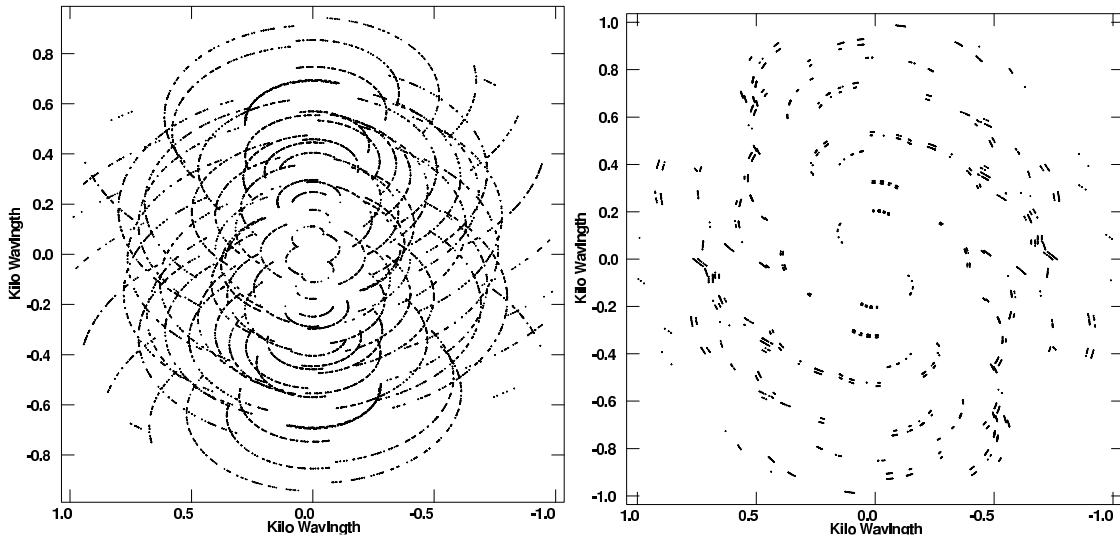Figure 3.3: Comparison between the inner portion of the u–v plane sampled by the GMRT observations at 325 MHz (*left panel*) and at 610 MHz (*right*) from which the flux density measurements of the halo has been taken. Only baselines shorter than 1 kλ have been plotted.

---

[1]The angular size of the halo ($\sim 5'$) is sampled by visibilities corresponding to baselines shorter than ~ 0.7 kλ.

3.4   The integrated radio spectrum of the halo

In order to derive the spectrum of the giant radio halo in A 697 with at least three data points, we complemented the GMRT flux density values at 610 MHz and 325 MHz with archival 1.4 GHz VLA–C public data.

3.4.1   VLA archive data at 1.4 GHz

We re–analyzed archival VLA–C observations at 1.4 GHz (Obs. Id. AJ0252; 31 March 1996). These are short observations centered on A 697, with total integration time of ~ 50 minutes and u–v range 0.3–15 kλ. After the usual a–priori calibration, the final images were obtaind after a few iterations of phase–only self–calibration. We successfully detected diffuse emission at the cluster centre. In order to account for the contribution of the point sources in the halo region, we produced an image using only baselines longer than 3 kλ, to rule out the contribution of the halo emission (resolution $\sim 9'' \times 11''$). The 1σ rms is ~ 12 μJy/b. In the central halo region we identified 7 point sources, with peak flux density exceeding 5 times the rms level; two of them were already found at 610 MHz, and labelled A (the central cD) and F in Venturi et al. (2008). We fitted all sources with individual Gaussians, and obtained a total contribution to the integrated flux density of $S_{1.4 \ GHz} = 0.97 \pm 0.05$ mJy. In Fig. 3.4 we show a low resolution image of the radio halo at 1.4 GHz (restoring beam of $35'' \times 35''$) for comparison with the 325 MHz and 610 MHz images. The crosses mark the position of the embedded point radio sources. Note that the field shown is the same as the right panel of Fig. 3.2.

At 1.4 GHz the radio halo appears considerably smaller than in the GMRT images. It is elongated in the East–West direction, in agreement with the brightest part of the 610 MHz emission. The LAS is $\simeq 190''$, corresponding to a LLS $\simeq 810$ kpc h_{70}^{-1}. Its total flux density is $S_{1.4 \ GHz} = 3.7 \pm 0.2$ mJy, corresponding to a radio power $logP_{1.4 \ GHz}$ (W/Hz)=23.95. This value was obtained by integrating this image over the same area covered by the radio halo at 325 MHz, and after subtraction of the total contribution of the embedded point sources.

Hints of diffuse emission at the centre of A 697 are visible on the NVSS 1.4 GHz image (Fig. 3.5, top panel). However, after an accurate inspection we concluded that this image is affected by secondary lobes residuals (see Giacintucci 2007). For this reason, the NVSS pointing containing the A 697 field was imaged after a new

calibration. We found out that one IF (intermediate frequency channel) was affected by strong interference, and it was necessary to remove it from the self–calibration and imaging process. The new image is reported in the central panel of Fig. 3.5: indeed, no extended emission is detected at the cluster centre at the noise level of $\sim$0.3 mJy b^{-1}. Our re–analysis confirmed that the extended structure visible in the public NVSS image is coincident with a peak of a residual secondary lobe, which crosses the image along the NW–SE direction, i.e. the same direction of the structure itself. Some residual patterns are still visibile in the recalibrated image at the 1σ level. The bottom panel of Fig. 3.5 reports the recalibrated NVSS image (contours) overlaid on the 1.4 GHz VLA–C image (grey scale). The non–detection on the recalibrated NVSS image is consistent with the VLA–C image, given the rms, peak and restoring beams in the two images (see figure caption). We integrated the flux density on the recalibrated NVSS image over the same sky portion covered by the radio halo at 1.4 GHz, and measured 2.4 mJy. Considering that the contribution of point sources in this region is 0.97 mJy (see above), we can conclude that the flux density of the radio halo on the NVSS amounts to $\simeq$ 1.4 mJy.

3.4.2   Integrated radio spectrum

The measure of the integrated spectrum of radio halos may be affected by two main factors: *(1)* the contribution to the flux density of embedded individual radio sources, and *(2)* the u–v coverage at short spacings.
Embedded individual sources are most likely of AGN origin, whose spectrum is flatter than radio halos. An inaccurate or inefficient subtraction of these sources may affect the flux density measurements at the various frequencies. On the other hand, the u–v coverage at short spacings may affect the detection of large scale structure.
We dealt with point *(1)* in Sect. 3.3.3 and 3.4.1. Point *(2)* will be the focus of Sect. 3.5.

All the available flux density measurements of the radio halo are reported in Table 3.4, along with the angular resolution of the images used for the measurements. The source is undetected on the Very Low–Frequency Sky Survey (VLSS) at 74 MHz, most likely due to the very poor sensitivity of the A 697 field.

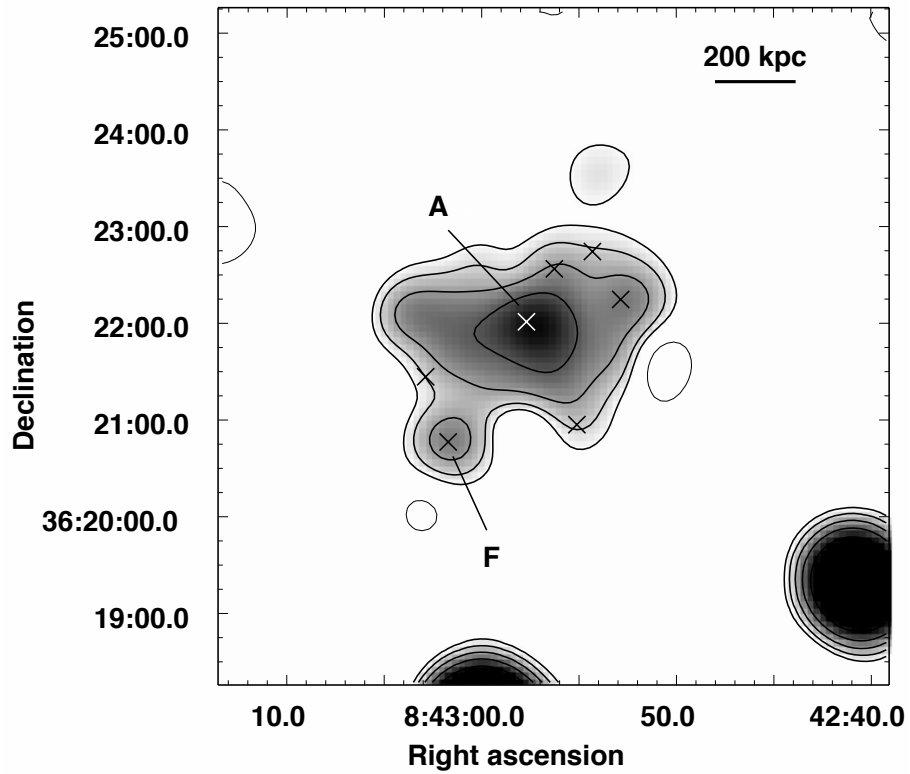The sources of uncertainty on the radio halo flux densities at 325 MHz and 1.4

Figure 3.4: Low resolution VLA–C 1.4 GHz image of the radio halo in A 697. The 1σ level in the image is 25 μJy b^{-1}. Contours are spaced by a factor 2 starting from $3\sigma = \pm\ 0.075$ mJy b^{-1}. The restoring beam is $35.0'' \times 35.0''$, p.a. $0°$. Crosses mark the position of the radio sources embedded in the halo emission.
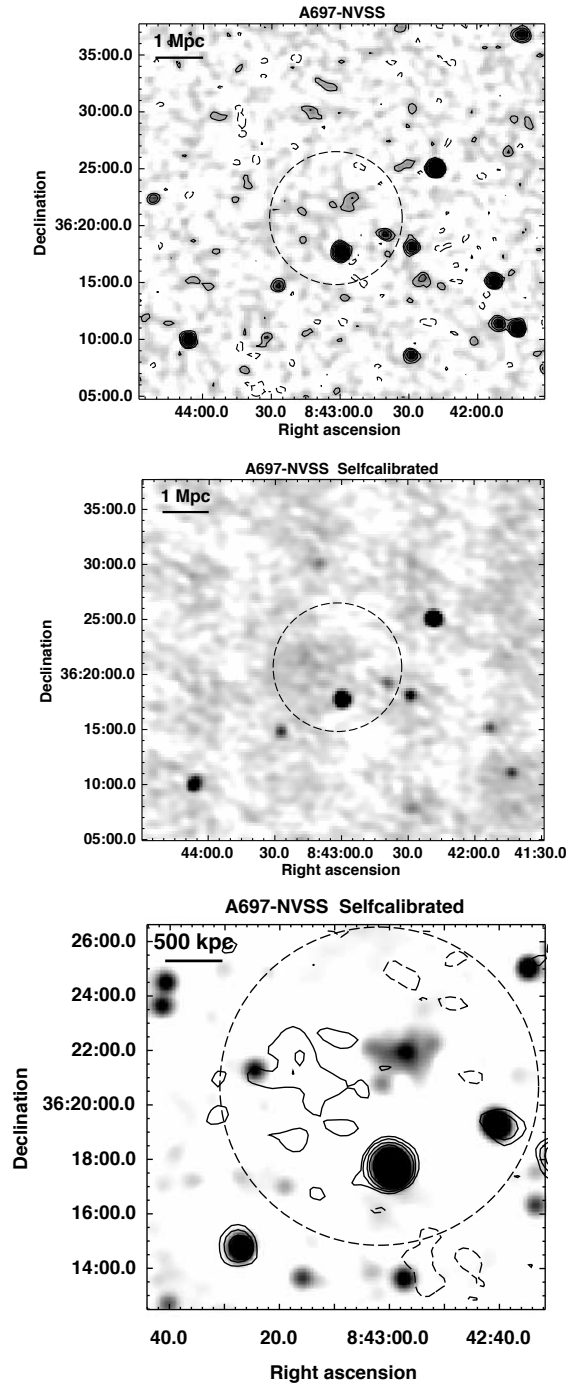
Figure 3.5: *Top Panel:* Radio contours of the A 697 field from the public 1.4 GHz NVSS image (grey scale). The 1σ level is 0.45 mJy b^{-1}. Contour levels are spaced by a factor 2, starting from ± 1 mJy b^{-1}; the resolution is $45'' \times 45''$, p.a $0°$. *Central Panel:* 1.4 GHz image (grey scale) of the NVSS pointing containing A697 after new calibration. The 1σ level is 0.3 mJy b^{-1}. The resolution is $45'' \times 45''$. *Bottom Panel:* Recalibrated NVSS image (contours) overlaid on the VLA–C array 1.4 GHz image (same as Fig. 4). The first contour is ± 0.3 mJy b^{-1}; contours are spaced by a factor of 2. The dashed circle highlights the portion of the field referred to in Sec. 3.4.1.

GHz are the calibration errors and the procedure of point source subtraction, which we estimate sum up to $\sim 5\%$. The flux density value at 610 MHz is affected by a higher uncertainty. We performed an accurate check on flux density at 325 MHz, 610 MHz and 1.4 GHz for a number of discrete sources in the central field (see Fig. 3.1), using three images with the same angular resolution as the full resolution at 1.4 GHz ($\sim 16'' \times 16''$), after correction for the corresponding primary beam. We found that the 610 MHz flux densities are systematically underestimated by $\sim 12\%$; after further inspection of the data, we concluded that this is due to an amplitude sistematic error. Note that large residual calibration errors at 610 MHz were reported also for the cluster A 3562 in Giacintucci et al. (2005). Considering all this, the 610 MHz flux density value of the radio halo in A 697 given in Venturi et al. (2008) was corrected to account for this effect (Table 4 reports the new corrected value).

The integrated radio spectrum of the halo is shown in Fig. 3.6. The red solid line is the linear fit to the data (filled triangles) weighted for the uncertainties. A single power–law fit to the data gives a spectral index $\alpha = 1.8 \pm 0.1$. For seek of completeness, we note that Giovannini et al. 2009 estimated a spectral index $\alpha_{325\ \mathrm{MHz}}^{1.4\ \mathrm{GHz}}$=1.2 using our GMRT 325 MHz flux density value preliminary presented in Venturi et al. (2009) and the 1.4 GHz value derived from the original NVSS image. As shown in Sect. 3.4.1, the NVSS value overestimates the flux density at the centre of A 697, leading to an unreliably flatter spectrum.

Table 3.4: Flux densites of the radio halo in A 697.

ν (MHz)	S_ν (mJy)	HPBW $''\times''$	Ref.
325	47.3±2.5	46.8 × 41.4	this work; Fig. 3.2
610	14.6±1.7	46.4 × 35.9	Venturi et al. 2008; see also this work Fig. 3.2
1400	3.7±0.2	35.0 × 35.0	this work; Fig. 3.4 *

* From VLA–C archival data (Obs. Id. AJ0252)

3.5 Uncertainties in the spectral slope

The combination of very low brightness emission and large angular size makes the imaging of faint radio halos a challenging process. The sampling of the u–v coverage
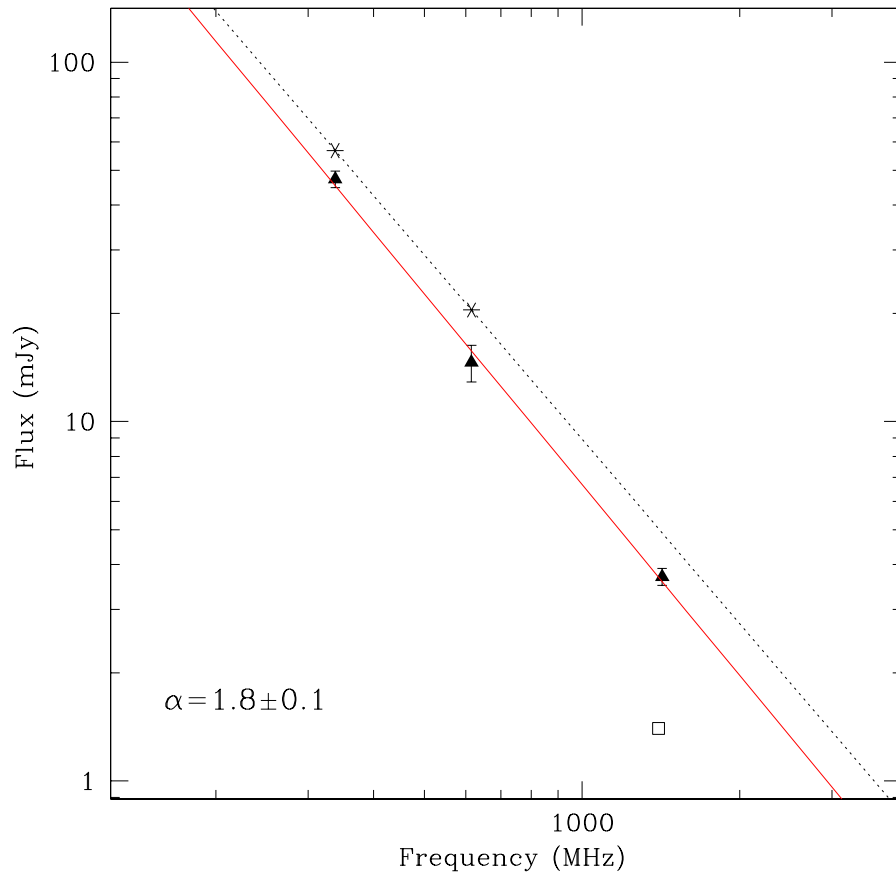
Figure 3.6: Integrated radio spectrum of the halo. The red solid line is the linear fit to the data (filled triangles), weighted for uncertainties. The dashed line connects the two values of flux density including the estimated losses at 325 and 610 MHz (stars). The open square is the estimated flux density of the radio halo on the NVSS.

at short spacings is essential for a reliable imaging of extended and diffuse radio sources, and this is particularly relevant for faint radio halos, as is the case of A 697. The most serious effect of an inadequate u–v coverage at short baselines is the loss of a fraction of the radio halo flux density, which may affect not only the imaging at an individual frequency, but also the integrated sectrum of the source. The latter effect becomes even more severe when only few data points over a small frequency range are available.

In this Section we will discuss the role of the u–v coverage in the GMRT observations of A 697 and the implications on the spectral steepness of its giant radio halo. We will show that part of the total flux density of the radio halo could not be accounted for by the GMRT observations. This effect is more relevant at 610 MHz, since Fig. 3.3 clearly shows that the inner portion of the u–v coverage is much better sampled in the 325 MHz observations. Given that an underestimate of the 610 MHz flux density would reflect into a steeper spectrum, it is crucial that we test the reliability of the spectral index derived in the present work.

To constrain the spectrum of the radio halo, we estimated the flux density losses expected both in the 325 and 610 MHz GMRT data following the *"fake radio halos"* procedure (see also Venturi et al. 2008).

In the following section we describe the main steps of this procedure and the results obtained.

3.5.1 The "fake radio halos" procedure

A *"fake radio halo"* is a model of the radio halo brightness profile, which consists of a set of optically thin concentric spheres with different radius and flux density. Integrated brightness profiles have been derived for a number of well studied radio halos (*e.g.* Govoni et al. 2001a; Cassano et al. 2007). The normalized radial profiles are reported in Fig. 3.7 (see Brunetti et al. 2007): they are quite similar and, in all cases, $\sim 50\%$ of the halo luminosity is emitted within about half the halo radius. On the basis of this observed property, in the following analysis we modeled each fake radio halo with a set of 7 concentric spheres, properly chosen to fit the radio halo brightness profile (Fig. 3.7).

The main steps of the procedure are the following:

1. We obtained families of fake radio halos with steps in total flux densities (S_{FH})

and largest angular size (LAS$_{FH}$; *i.e.,* the diameter of the largest sphere of the model). We explored a range of LAS$_{FH}$ between $240''$ to $330''$, corresponding to a linear scale in the range $1\div1.4$ Mpc h$_{70}^{-1}$ at the redshift of A 697. The total flux densities S$_{FH}$ ranges from 50 to 70 mJy.

2. Each fake radio halo was injected in the final u–v dataset by means of the task UVMOD in AIPS (run twice), which transforms the brightness distribution of the model into u–v components, adds them to the original data, and produces a "modified" u–v dataset. We chose the centre of the injections in an empty region, sufficiently far from the real radio halo emission and free of point sources.

3. Each "modified" dataset was imaged by means of task IMAGR in AIPS, with the same sets of parameters applied to the original data; we then produced final images with the same low angular resolution of the final image at 325 MHz which we used to integrate the flux density of the real halo ($\sim 47'' \times 41''$, see Fig. 3.2). Note that both the fake and the real radio halos are imaged simultaneously, allowing a direct comparison between the morphological properties of the two sources.

4. From each final low resolution image, we finally measured the LAS of the imaged fake radio halo and we integrated its flux density (task TVSTAT) over an area covered by the first 3σ contour.

In general we found that the component with the largest angular size, *i.e.,* the one with lowest surface brightness, is partially lost in the imaging process. This effect becomes more and more important for progressively lower S$_{inj}$ and/or higher LAS$_{inj}$. On the contrary, the central highest surface brightness regions are well imaged. These general results are in agreement with the findings in Venturi et al. (2008).

An injected fake halo with S$_{inj}$=60 mJy and LAS=$330''$ best reproduces the emission observed at the cluster centre, *i.e.,* S$\simeq$ 48 mJy and LAS$\simeq$ $300''$ (see Sect. 3.3.3); the relative image is shown in Fig. 3.8.

Based on these tests, we concluded that the expected flux density loss of the radio halo at 325 MHz is at most $\sim$20 %. Most of this flux density is lost in the largest and lowest surface brightness component. The LAS of the real halo is $\sim$ 10 % smaller than that injected.

3.5.2   The 610 MHz data and the "revised" spectrum

Following the same procedure, we estimated the flux density loss at 610 MHz. A fake halo with LAS=330″ (same choice as for the injection at 325 MHz) and S_{inj}=20 mJy best reproduces the radio halo observed at 610 MHz. The resulting differential flux density loss between 325 MHz and 610 MHz is ∼ 20 %. Based on these results, we estimated that the intrinsic flux density of the radio halo in A 697 is ∼ 57 mJy at 325 MHz and ∼ 20 mJy at 610 MHz (accounting for the 12% flux density correction derived in Sect. 3.4).

In Fig. 3.6 we report the integrated spectrum of the halo between 325 and 610 MHz taking into account the estimated losses in flux density (the dashed line connects the two values, represented by the star symbols). The resulting spectral index is $\alpha_{rev} \sim 1.7$. We thus safely conclude that A 697 hosts a very steep spectrum radio halo. The flux density we measured at 1.4 GHz can be considered a lower limit, the upper one being the extrapolation of the "revised" spectrum between 325 MHz and 610 MHz. This leads to an "expected" flux density value $S_{1.4\ GHz} \simeq 5$ mJy over the same region considered before.
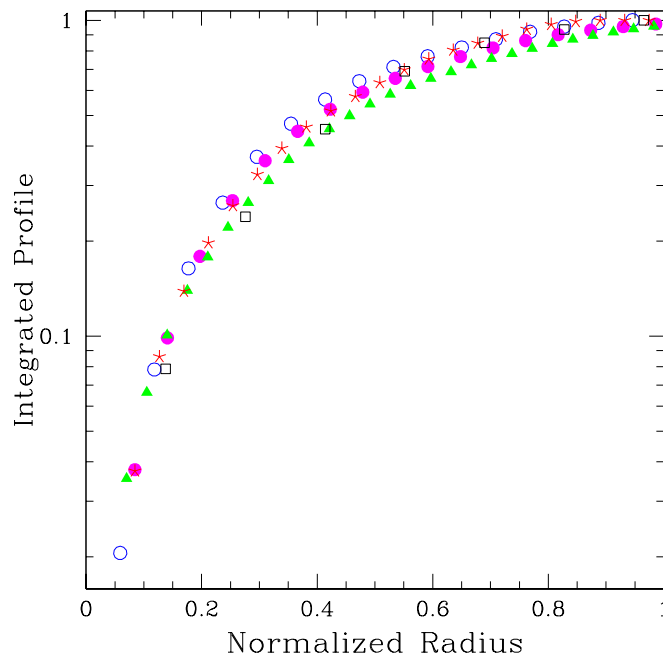

Figure 3.7: Normalized integrated brightness profiles of well-studied RHs (from Brunetti et al. 2007): A545 (boxes), A2319 (triangles), A2744 (open circles), A2163 (filled circles), and A2255 (stars).
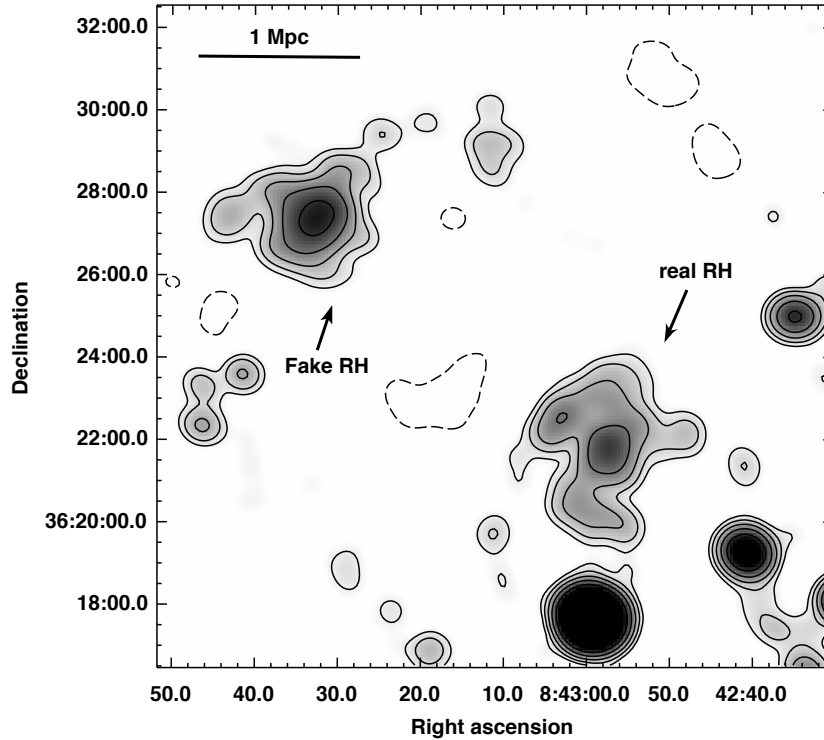
Figure 3.8: 325 MHz GMRT image obtained after the injection of a fake radio halo with S_{inj}=60 mJy and LAS=330$''$. The imaged fake radio halo best reproduces the real radio halo emission. The resolution is $\sim 47'' \times 41''$. Contours are spaced by a factor of 2, starting from $\pm3\sigma$=0.5 mJy b^{-1}.

3.6   Discussion

The radio halo in A 697 has observational properties similar to those of A 521, which we consider the prototypical example of ultra steep spectrum radio halos. In particular, it is barely detectable at 1.4 GHz with the current instruments, and with the observed values $\log P_{1.4\ GHz}$(W/Hz) =23.95 and $L_{X[0.1-2.4]\ keV} = 1.06 \times 10^{45}$ erg s^{-1}, it lies below the well–known $\log P_{1.4\ GHz}$–$\log L_{X}$ correlation for giant radio halos (Sect. 2.3, Fig. 2.2). The source becomes stronger and considerably more extended at lower frequencies. This is different from what is observed for those radio halos with spectral index $\alpha \sim 1.2 - 1.4$, whose overall morphology and size do not change appreciably moving down to lower frequencies (see for instance A 2744 and A 2219, Orrú et al. 2007; A 2319, Feretti et al. 2001; MACS J 0717.5+3745, van Weeren et al. 2009 and Bonafede et al. 2009a; RXCJ2003.5–2323, Giacintucci et al. 2009). Based on literature data, Giovannini et al. (2009) reported on four more halos with very steep integrated spectrum; however, the different resolutions and

u–v coverages, and the lack of accurate subtraction of individual embedded radio sources in heterogenous datasets, may affect the shape and spectral index of the integrated spectra.

The observational connection between major cluster mergers and radio halos is a fairly well established result, both on the basis of individual studies (examples of recent multiband analysis may be found in Govoni et al. 2004; van Weeren et al. 2009; Bonafede et al. 2009a; Giacintucci et al. 2009) and on statistical properties of large samples (see Buote 2001 ; Venturi et al. 2008; Cassano et al. 2010b; see also Section 2.3). On the other hand, it has been recently claimed on statistical basis that the majority of radio halos should be generated during more common but less energetic mergers, for example between a massive cluster and a much smaller subcluster (with mass ratio $\gtrsim$ 5) or between two similar clusters with mass M $\lesssim 10^{15} M_\odot$, which would trigger the formation of radio halos observable only up to few hundred MHz (Cassano et al. 2006 and Cassano 2009; see Section 2.4). So far, these elusive radio halos have been missed from large surveys mainly due to their steep spectrum, which requires very sensitive observations at frequencies $\nu \leq 1$ GHz. The discovery of the ultra steep spectrum radio halo in A 521 (Brunetti et al. 2008; see Section 2.3) provided observational support in favour of this idea.

3.6.1 The merger in the cluster A 697

A detailed optical analysis of A 697 was carried out in G06, who found that the cluster is significantly far from dynamical relaxation. In particular, the observed complex dynamical state of A 697 might be explained either as an ongoing process of multiple accretion of small ($\lesssim 0.2$ Mpc) clumps by a very massive cluster, or as the result of a past merger event. The scenario may be even more complicated (major merger followed by multiple accretion), as suggested by the absence of a cool core in this cluster (Bauer et al. 2005). G06 concluded that it is difficult to provide more details on the type of merger in A 697, since most likely we are viewing the system at a small angle to the line of sight. Analysis of archival *Chandra* X–ray observations (G06) revealed the presence of significant substructure in the core region, with three clumps of emission within ∼200 kpc from the centre, confirming the cluster complex dynamical state.

Giacintucci (2007) re–analysed the public archival *Chandra* ACIS–I observation

of A 697 (19.8 ks, OBSID 4271, presented also in G06). In Fig. 3.9 we report a new wavelet–reconstructed *Chandra* image of A 697, with 325 MHz contours of the radio halo superposed (same image as right panel of Fig. 3.2). The X–ray image was obtained applying the wavelet decomposition tool (Vikhlinin et al. 1997) to the cluster image in the 0.5–9 keV energy band, divided for the exposure map and background subtracted (see Giacintucci 2007 and references therein).
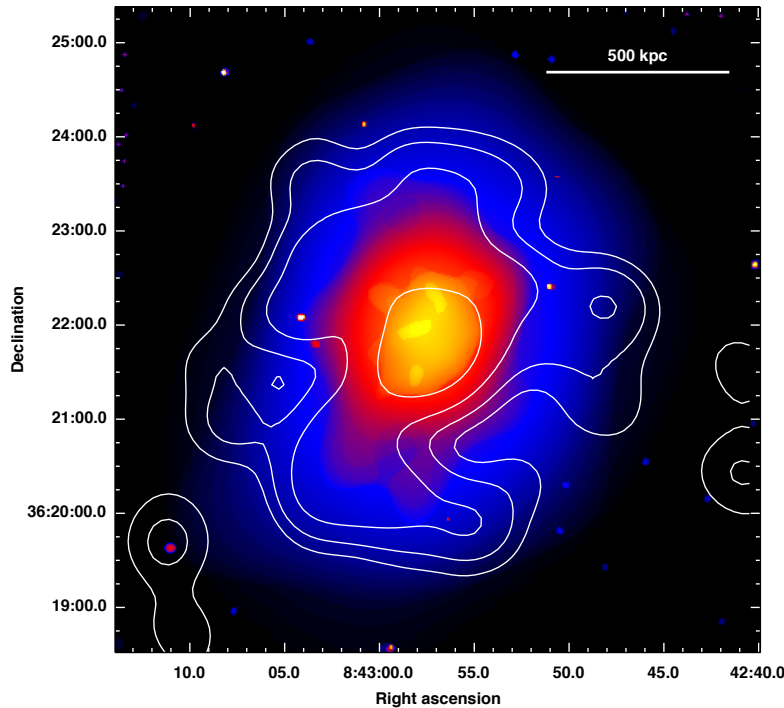
Figure 3.9: Wavelet–reconstructed *Chandra* image of A 697, in the 0.5–9 keV band. The image is corrected for the exposure and background subtracted. Overlaid are the 325 MHz contours of the radio halo. The radio image is the same as right panel of Fig. 3.2.

As clear from Fig. 3.9, the overall X–ray morphology of the cluster is elliptical, and elongated along the North–North West/South–South East (NNW/SSE) direction. The extent and shape of the radio emission are in agreement both with the size of the X–ray emitting region and with the slight elongation along the NNW/SSE axis. Moreover, the peak of the radio emission covers the inner ~ 200 kpc of the core region, where the three X–ray subclumps are located. The cluster temperature and hardness ratio distributions were derived in Giacintucci (2007), with the calibration files available at the time. Gradients between the inner $\sim$200 kpc core region and the surrounding areas were found both in the temperature and in the hardness ratio, in agreement with the proposed overall picture that A 697 is

dynamically unrelaxed. This analysis supports the multiple merger scenario, but unfortunately the short exposure time of the *Chandra* observations does not allow a more quantitative analysis.

3.6.2 Origin of the radio halo

As we mentioned in the introduction (Section 1.9.1), it is presently believed that two main physical processes may contribute to the origin of the extended diffuse synchrotron emission in giant radio halos: the injection of secondary electrons through proton–proton collisions (hadronic models, *e.g.* Dennison 1980; Blasi & Colafrancesco 1999; Pfrommer & Ensslin 2004), and the in–situ re–acceleration of relativistic electrons by MHD turbulence generated in the ICM during cluster-cluster mergers (re–acceleration models, Brunetti et al. 2001, 2004; Petrosian 2001; Fujita et al. 2003; Cassano & Brunetti 2005).

Radio halos with very steep spectrum, i.e. $\alpha \geq 1.6$, are suitable targets to constrain these models and favour a turbulent re–acceleration scenario (Brunetti et al. 2008): in fact, in the context of the hadronic scenario, clusters hosting these radio halos must contain a very large population of cosmic ray protons. The observations presented in this study suggest that Abell 697 hosts a very steep spectrum giant halo and this allows a prompt test of the hadronic model.

3.6.3 Energetics for hadronic models

In this Section we assume that the giant radio halo in A 697 is of hadronic origin and discuss the consequences of this hypothesis on the physical properties of the ICM.

The decay chain that we consider for the injection of secondary particles in the ICM due to p-p collisions is (Blasi & Colafrancesco 1999):

$$p + p \rightarrow \pi^0 + \pi^+ + \pi^- + \text{anything}$$

$$\pi^0 \rightarrow \gamma\gamma$$

$$\pi^\pm \rightarrow \mu + \nu_\mu \quad \mu^\pm \rightarrow e^\pm \nu_\mu \nu_e.$$

that is a threshold reaction that requires protons with kinetic energy larger than $T_p \approx 300$ MeV.

A practical and useful approach to describe the pion spectrum both in the high energy ($E_p > 10$ GeV) and low energy regimes was proposed in Dermer 1986 and reviewed by Moskalenko & Strong 1998 and Brunetti & Blasi (2005), and is based on the combination of the isobaric model (Stecker 1970) and scaling model (Badhwar et al., 1977; Stephens & Badhwar 1981).

The injection rate of pions is given by :

$$Q_\pi^{\pm,o}(E,t) = n_{th}^p c \int_{p_*} dp N_p(p,t) \beta_p \frac{F_\pi(E_\pi, E_p)\sigma^{\pm,o}(p_p)}{\sqrt{1 + (m_p c/p_p)^2}}, \tag{3.1}$$

where we adopted F_π as given in Brunetti & Blasi (2005) that use the isobaric model for $E_p < 3$ GeV, a scaling model for $E_p > 10$ GeV and a linear combination of the two models for intermediate energies, and where p_{tr} is the threshold momentum of protons for the process to occur.

The injection rate of relativistic electrons/positrons is given by :

$$Q_{e^\pm}(p,t) = \int_{E_\pi} Q_\pi(E_{\pi^\pm}, t) dE_\pi \int dE_\mu \times$$
$$F_{e^\pm}(E_\pi, E_\mu, E_e) F_\mu(E_\mu, E_\pi), \tag{3.2}$$

where $F_e^\pm(E_e, E_\mu, E_\pi)$ is the spectrum of electrons and positrons from the decay of a muon of energy E_μ produced in the decay of a pion with energy E_π, and $F_\mu(E_\mu, E_\pi)$ is the muon spectrum generated by the decay of a pion of energy E_π that is :

$$F_\mu(E_\mu, E_\pi) = \frac{m_\pi^2}{m_\pi^2 - m_\mu^2} \frac{1}{\sqrt{E_\pi^2 - m_\pi^2}} \tag{3.3}$$

between a kinematic minimum and maximum muon energy given by :

$$m_\mu \gamma_\pi \gamma_\mu' (1 - \beta_\pi \beta_\mu') \leq E_\mu \leq m_\mu \gamma_\pi \gamma_\mu' (1 + \beta_\pi \beta_\mu') \tag{3.4}$$

where γ_μ' is the Lorentz factor of the muon in the pion frame, $\beta_\mu' \simeq 0.2714$ (Moskalenko & Strong 1998), and from kinematics :

$$m_\mu \gamma_\mu' \beta_\mu' = \frac{m_\pi^2 - m_\mu^2}{2m_\pi}. \tag{3.5}$$

In order to simplify calculations, following Brunetti & Blasi (2005), we assume that the spectrum of muons is a delta–function :

$$F_\mu(E_\mu, E_\pi) = \delta\left(E_\mu - \bar{E}_\mu\right) , \tag{3.6}$$

where

$$\bar{E}_\mu = \frac{m_\pi^2 - m_\mu^2}{m_\pi^2} \frac{E_\pi}{2\beta'_\mu} . \tag{3.7}$$

We use the spectrum of electrons and positrons from the muon decay, $F_{e^\pm}(E_\pi, E_\mu, E_e)$, as given by Blasi & Colafrancesco (1999), and combining their results with Eqs. (3.1), (3.2) and (3.6), we obtain the rate of production of secondary electrons/positrons :

$$Q_{e^\pm}(p, t) = \frac{8\beta'_\mu m_\pi^2 n_{th}^p c}{m_\pi^2 - m_\mu^2} \int_{E_{\min}} \int_{E_*} \frac{dE_\pi dE_p}{E_\pi \bar{\beta}_\mu} \beta_p N(E_p) \times$$
$$\sqrt{1 - (\frac{m_p c^2}{E_p})^2} \sigma^\pm(E_p) F_\pi(E_\pi, E_p) \tilde{F} , \tag{3.8}$$

where $E_{\min} = 2E_e \beta'_\mu m_\pi^2/(m_\pi^2 - m_\mu^2)$, and $\tilde{F}$ is defined in Brunetti & Lazarian (2010; see their Section 3.4).

Under the assumption that secondary electrons are not accelerated by other mechanisms, their spectrum approaches a stationary distribution due to the competition between injection and energy losses (Dolag & Ensslin 2000) :

$$N_e^\pm(p) = \frac{1}{\left|\left(\frac{dp}{dt}\right)_{\text{loss}}\right|} \int_p^{p_{\max}} Q_e^\pm(p) dp. \tag{3.9}$$

where $Q_e^\pm$ is the injection rate of secondary electrons (Eq. 3.8) and the radiative losses, that dominate for $\gamma > 10^3$ electrons in the ICM, are (Sarazin 1999) :

$$\left|\left(\frac{dp}{dt}\right)_{\text{loss}}\right| \simeq 3.3 \times 10^{-32} (\frac{p/m_e c}{300})^2 \left[\left(\frac{B_{\mu G}}{3.2}\right)^2 + (1+z)^4\right]. \tag{3.10}$$

We assume a power law distribution of relativistic protons, $N_p(p) = K_p p^{-s}$, in which case the spectrum of secondaries at high energies, $\gamma > 10^3$, is $N_e(p) \propto p^{-(s+1)}\mathcal{F}(p)$, where $\mathcal{F}$ accounts for the Log–scaling of the p-p cross section at high energies and makes the spectral shape slightly flatter than $p^{-(s+1)}$ (Brunetti & Blasi 2005; Brunetti 2009).

The synchrotron emissivity from secondary $e^{\pm}$ is also obtained via standard formulae (Rybicki & Lightman 1979):

$$J_{syn}(\nu) = \sqrt{3}\frac{e^3}{m_e c^2}B\int_0^{\pi/2}d\theta sin^2\theta\int dpN_e(p)F\left(\frac{\nu}{\nu_c}\right)$$

$$\propto n_{th}K_p\frac{B^{1+\alpha}}{B^2+B_{cmb}^2}\nu^{-\alpha} \tag{3.11}$$

where F is the synchrotron Kernel, ν_c is the critical frequency, and $\alpha \simeq s/2 - \Delta$, $\Delta \sim 0.1 - 0.15$ due to the logarithmic scaling of the cross section (Brunetti 2009). We adopt a value of the spectral index of the halo $\alpha \simeq 1.75$ which implies a spectral slope of the cosmic ray protons $s \sim 3.8$.

The diffuse emission of the radio halo is centered on the cluster core region and grossly resembles the X-ray morphology both in terms of extension and elongation (Fig. 3.9). The radio profile at 325 MHz, however, is flatter than the X-ray profile.it drops by only a factor 5–6 at distance of 2.5–3 core radii ($\sim$ 500 kpc), suggesting a broad spatial distribution of the relativistic particles. Thus we used a β-model (see Section 1.2, Eq. 1.3) for the spatial distribution of the cluster thermal gas, with parameters taken from Bonamente et al. 2006 (β=0.6, $n_0 = 9.8 \times 10^-3$ cm^{-3}, r_c=42$''$, *i.e.,* $\sim$ 180 kpc, and gas temperature kT= 10 keV) and we adopt a model (*Model* 1) of the distribution of relativistic components in Abell 697 where the energy density of both cosmic ray protons and magnetic field are *constant* with radius up to a distance $= 2.5\,r_c$, and scale with that of the thermal gas at larger distances. This model gives a reasonable representation of the observed halo-radial profile up to a distance of about 2.5 r_c and, within the uncertainties, it is also in line with the observed profile at large distance (regardless of the strength of the magnetic field at $\leq 2.5\,r_c$ distance ; Figure 3.10).
In Fig. 3.11 we show the ratio of the energy density of non–thermal (relativistic protons and magnetic field) and thermal components in Abell 697 that is required assuming a hadronic origin of the radio halo. The energy density of non-thermal components is given by:

$$\epsilon_{NT} = \epsilon_B + \epsilon_p = \frac{B^2}{8\pi} + \int_{p_{\min}} N(p)E(p)dp \tag{3.12}$$

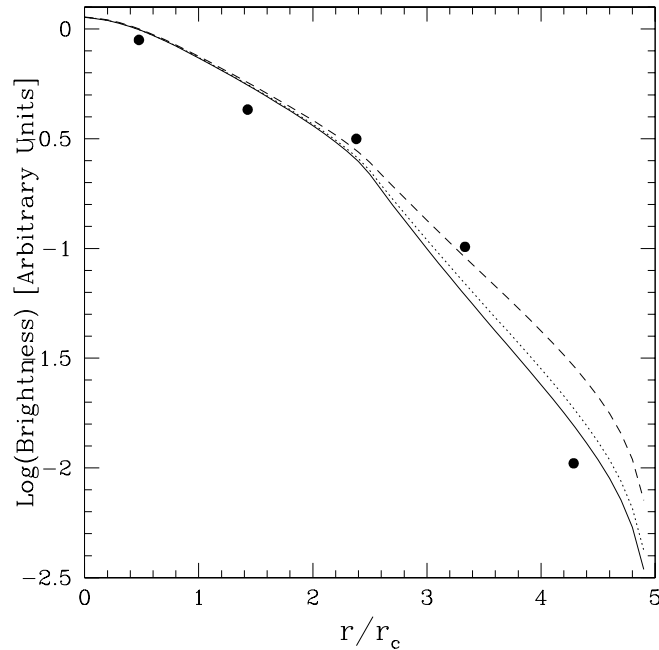where $E(p) = m_p c^2[\sqrt{1 + (p/m_p c)^2} - 1]$.

Figure 3.10: Observed radio brightness profile of the halo in A 697, extracted from the 325 MHz image (filled dots), normalized to the core radius r_c of the β-model for the ICM (with parameters taken from Bonamente et al. 2006). The lines show the brightness profile derived from *Model 1*, for different values of the magnetic field, assumed to be constant within $2r_c$ (see text): 3μG (solid line), 5 μG (dotted line), 15 μG (dashed line).

We find that for $B \leq 5\mu$G relativistic protons are required to store an energy comparable to (or larger than) that of the thermal ICM. The non–thermal energy content reaches a minimum for $B \approx 10\mu$G, $\epsilon_{NT} \approx 1/3\epsilon_{TH}$, implying an important dynamical contribution of the non–thermal components in the cluster. In addition, we point out that *Model* 1 provides only a lower limit to the energy of the non–thermal components for two main reasons :

- 1) as soon as we include also the contribution from the tail of the proton energy distribution at sub–relativistic energies (E< 1 GeV), the required energy budget is much larger than that in Fig. 3.11 due to the steep proton spectrum, $\epsilon_{CR} \propto p_{min}^{-s+3}$.

- 2) the rather unphysical assumption in *Model* 1 that the energy density of the non-thermal components are *constant* with radius (up $2.5\,r_c$) yields a lower limit to the energy density of the cosmic ray protons that is required by the hadronic scenario. Indeed as soon as the magnetic field strength in Abell 697 is allowed to decrease with distance from the cluster centre, the energy density
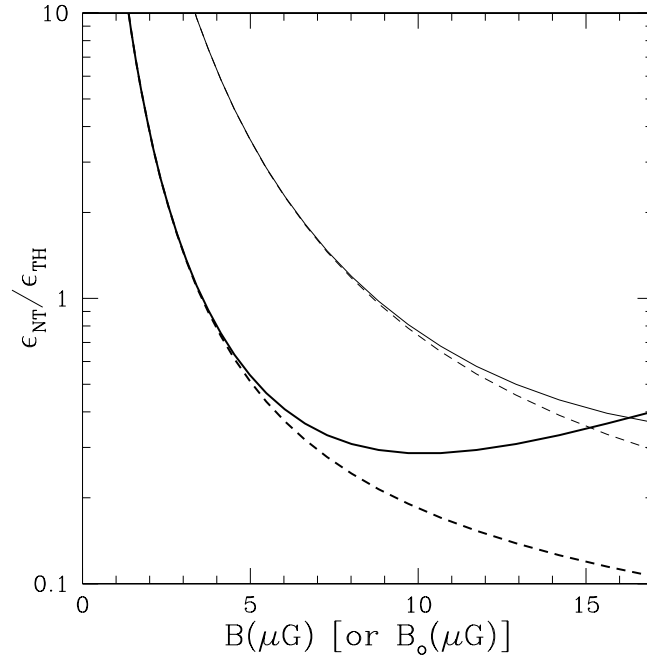
Figure 3.11: The ratios between the energy densities of relativistic protons and thermal ICM (dashed lines) and between non-thermal (relativistic protons and magnetic field) and thermal ICM (solid lines) are shown as a function of the magnetic field. All energy densities are calculated within a distance $r \sim 3\,r_c$, i.e. roughly the region filled by the radio halo. Thick lines refer to *Model* 1, in which case B is that within $2.5\,r_c$. Thin lines are obtained by assuming that the magnetic field energy-density scales with the thermal one, $B = B_o(n_{th}/n_o)^{1/2}$ (*e.g.* , Govoni & Feretti 2004), and by leaving the radial profile of relativistic protons free to vary with distance (up to $r \sim 2.5r_c$ while at larger distances it is assumed to scale with thermal one as in *Model* 1) in order to match the observed synchrotron profile; in this latter case the x–axis shows the central field value, B_o.

of relativistic protons must increase with radius and their total energy budget increases (Fig. 3.11).

We conclude that the very large energetics necessary for the non–thermal components assuming a hadronic origin of the halo disfavours this scenario.

3.7 EVLA D+C follow up at 1.3 and 1.7 GHz

The 1.4 GHz flux density measurement of the radio halo is critical for constraining its spectral shape. Although the radio halo has been detected in the archival VLA-C observations (Sect. 3.4.1), part of its flux density might have been missed by these observations, due to the poor sensitivity to extended emission in C configuration and to the short integration time (Sect. 3.5.2; Fig. 3.6). No suitable D-configuration observations are available in the VLA archive (Sect. 3.4.1). We thus started an observing program with the Expanded VLA (EVLA), in order to exploit its improved sensitivity. Combined D+C observations are the key to address this problem, since they will provide sensitivity to the low surface brightness radio halo emission (D configuration) and enough angular resolution ($\sim 10''$ reachable in C configuration) to properly remove the contribution of individual embedded sources.

The main characteristics of the EVLA observations are summarized in Table 3.5. A 697 was observed in the D configuration for a total time of 10 hours (Obs. Id. AM1011). Due to the high pressure on the EVLA dynamic scheduling in the commissioning phase, the observations have been performed in four blocks of 2.5 hours each (see Table 3.5). Here we present preliminary results obtained from the the first 5 hours only (March 27). The data reduction of the remaining observations is in progress.

The two 2.5 hours blocks of observations (March 27) were performed consecutively (from 2:50 to 7:50, UTC); thus the two datasets were combined together (by means of the AIPS task DBCON) before proceeding with the calibration. The data were calibrated in a standard way (using AIPS), with amplitude, phase and band-pass calibration carried out after accurate editing of raw data on both the primary (J1331+3030) and secondary (J0909+4253) calibration sources. The accuracy of the flux density scale is within 5%, as estimated from the variation of the gain solutions over the whole observation. To reduce the dataset size, we averaged the calibrated visibilities in time (from 3 s to 10 s integration time) and frequency (by compressing the initial 64 channels into 8 channels). The two IF are centered at frequencies of 1286 (IF1) and 1746 MHz (IF2), thus they were self-calibrated and imaged separately. The IF1 was affected by strong RFI, which compromises the quality of the image. For this reason, only the IF2 image is presented here.

Table 3.5: Summary of the EVLA observations.

EVLA configuration	Project Id.	Obs. date	ν (MHz)	$\Delta\nu$ (MHz)	t (min)	HPBW ($''\times''$, °)	Notes
D	AM1011	Mar. 27, 2010	1286/1746*	128*	2×150	36×33, -66	(a)
D	AM1011	Apr. 17, 2010	1286/1746	128	150	46	(b)
D	AM1011	Jun. 6, 2010	1286/1746	128	150	46	(b)
C	AM1030	Oct. 7, 2010	1286/1746	128	150	14	(b)

Notes to Table 3.5: * Only the high frequency dataset (IF2) was used for the analysis (see Sect. 3.7). (a) Data reduction completed, analysis in progress; the HPBW is the restoring beam of the 1.75 GHz image (Fig. 3.12). (b) Data reduction in progress; the HPBW refers to the central frequency between the two IFs.
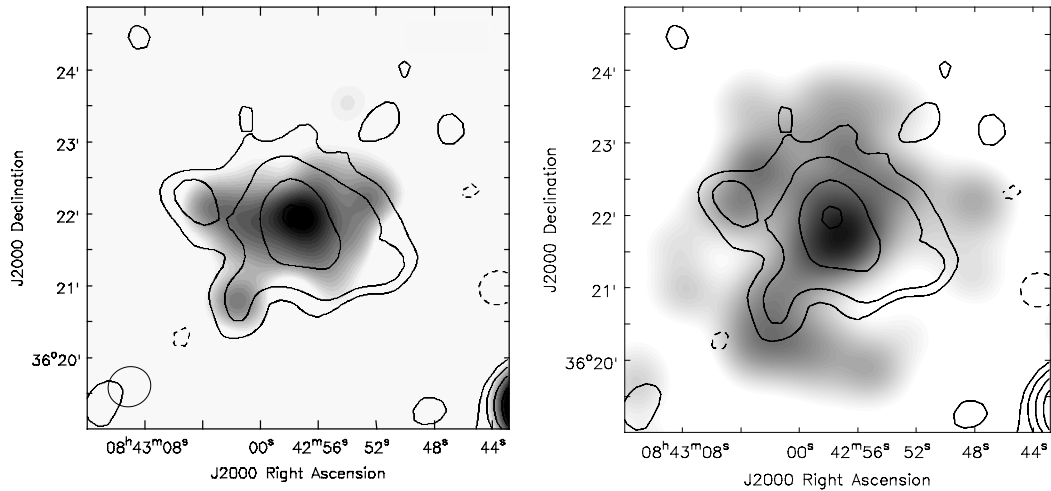
Figure 3.12: Low resolution EVLA–D 1.75 GHz contours of the radio halo in A 697. The 1σ level in the image is 38 μJy b^{-1}, and contours are spaced by a factor 2 starting from 3σ. The resolution is $36'' \times 33''$. *Left* – Contours are overlaid to the VLA–C image at 1.4 GHz, shown in grey-scale (same as in Fig. 3.4). *Right* – Contours are overlaid to the grey-scale GMRT image at 325 MHz (same as in Fig. 3.2).

The final D-configuration full resolution image ($36'' \times 33''$) is reported in Fig. 3.12, as contours. The 1σ noise level is 38 μJy b^{-1}. Contours starts at $\pm 3\sigma = 114$ μJy b^{-1}, and then scale by a factor of two. In left panel of Fig. 3.12 contours are overlaid to the VLA-C 1.4 GHz image of similar resolution ($35'' \times 35''$) (grey scale, same as in Fig. 3.4). The emission at 1.75 GHz is slightly more extended with respect to the 1.4 GHz image, both in the North and the South-West directions, due to the higher sensitivity to extended emission of the D-configuration observation. The LAS the is $\simeq 220''$ (along the North-East/South-West direction), which corresponds to a LLS$\simeq$ 935 kpc h$_{70}^{-1}$. The halo has almost the same brightness distribution around the central peak, and shows a similar feature in the East direction.

For a comparison, in right panel of Fig. 3.12 the same 1.75 GHz contours are overlaid to the 325 MHz GMRT image (in grey scale, same as in Fig. 3.2). The halo morphology at high frequency is in overall agreement with the central emission at 325 MHz; moreover, this overlay clearly shows the considerably larger extension of the steep spectrum radio halo at low frequency (as already pointed out in Sect. 3.6).

We measured the flux density of the radio halo by integrating the image over the area covered by the 3σ contour. After the subtraction of the ~ 1 mJy contribution of the embedded discrete radio sources (as estimated at 1.4 GHz, see 3.4.1 and Fig. 3.4), we find $S_{1.75\ \text{GHz}} \simeq 4.4$ mJy. This value should be still considered preliminary. Once the data reduction of the other observing blocks will be completed, we will be able to define a final value at this frequency, as well as a to derive a flux density measurement at 1.3 GHz (if data from IF1 will turn out to be usable). The new full resolution EVLA-C image will allow us to identify radio sources at the weakest flux density levels in the combined D+C image. This will allow us to derive more appropriate values of the extended radio halo flux densities at 1.3 GHz and 1.7 GHz.

3.8   Summary and conclusions

In this chapter we have presented 325 GMRT high sensitivity observations of the giant radio halo in A 697, and performed an accurate study of its integrated spectrum.

The largest extent of the radio halo at 325 MHz is $\sim 5'$ (corresponding to 1.3 Mpc h$_{70}^{-1}$), and it is considerably larger than at higher frequencies. The radio spectrum,

determined with three data points in the frequency range 325 MHz–1.4 GHz, has a spectral index $\alpha_{325\ \mathrm{MHz}}^{1.4\ \mathrm{GHz}} = 1.8 \pm 0.1$. An accurate analysis of the fraction of flux density that might be missed in our observations due to the u–v coverage at short spacings led to an estimated spectral index $\alpha_{\mathrm{rev}} = 1.7$. We thus conclude that A 697 hosts a very steep spectrum radio halo.

A qualitative analysis of the X–ray emission from the ICM confirms that this cluster is unrelaxed. Comparison with the 325 MHz emission from the radio halo shows that the non–thermal and thermal emissions have similar morphologies. Although at a qualitative level, the observations are in agreement with the idea that A 697 is the result of a multiple merger.

Similarly to the case of A 521, we showed that the very steep spectrum of the halo disfavours a hadronic origin, which would require an unplausibly large energy budget. On the other hand, models based on turbulent acceleration for the origin of radio halos predict a large number of halos in the Universe with very steep spectrum. This can be tested as soon as LOFAR (see Chapt. 6) and LWA will become operational.

Chapter 4

GMRT 150 MHz follow up of USSRHs

4.1 Low frequency radio observations: importance and issues

Radio observations at low frequencies (*i.e.,* $\nu \lesssim 330$ MHz) are particularly important to study steep spectrum ($\alpha < 1$) radio sources. Diffuse cluster sources, lobes of FRI and FRII radio galaxies, cavities filled with fossil plasma at the centre of galaxies and groups, restarted radio galaxies, are typical extragalactic radio sources best studied at such low frequencies. Only with the advent of the 74 MHz receiver on VLA antennas and the GMRT interferometer, operating down to 150 MHz, it has been possible to image such sources with high sensitivities (down to $\leq$ mJy/b) and proper angular resolution (from $\sim 10''$ to $\sim 1'$). At low frequencies, the field of view is very large and an individual observation covers several square degrees on the sky.

Observations at low frequencies raise a number of issues, mainly related to the ionosphere instability and the non-coplanarity of the sky when imaging such large areas. In particular, these effects are: (i) reduced telescope efficiency, (ii) wide-field imaging issues (as the w-term, bandwidth and time averaging smearing), (iii) poorly constrained and variable antenna beam patterns on the sky, (iv) substantial increase of radio frequency interference (RFI). Most of these effects can be corrected during data reduction if suitable algorithms are available. One of the main issues is related to the "non-isoplanaticity" of the ionosphere, *i.e.,* its ion density fluctuations on a large range of scales. These fluctuations can seriously affect wide-field very low

69

frequency ($\lesssim$ 150 MHz) observations (*e.g.* Cohen & Röttgering 2009). Different lines of sight will cross regions of the ionosphere with inhomogeneous properties, generating artifacts in the final images, especially associated with the brightest off-axis sources. Standard self-calibration algorithms can determine one correction per antenna, and cannot solve for these "direction-dependent" errors, thus dedicated techniques should be used (*e.g.* "peeling"techniques; *e.g.* Cotton et al. 2004; Intema et al. 2009).

Another important issue that affects low frequency observations is the RFI.

Due to combination of all these effects, the image background rms increase even more rapidly than the flux density of a very steep spectrum source, leading to a relative loss of dynamic range.

In light of the future high sensitivity low frequency arrays, such as LOFAR (already in its commissioning phase, see Chap. 6), LWA and SKA, dedicated algorithms are currently under development to properly correct all these effects.

4.2 The project

In light of the importance to extend our knowledge of the properties of cluster radio halos at low frequencies (*i.e.,* $\lesssim$ 330 MHz), a low frequency follow-up of a few galaxy clusters selected from the GMRT radio halo survey cluster sample (Chapter 2; Venturi et al. 2007 and 2008) has been recently carried out with the GMRT at 325 and 240 MHz (Venturi et al. 2009; Venturi et al. 2011, to be submitted).

Those deep low frequency observations allowed the discovery of the first USSRH in A 521 (Section 2.3), and of the very steep spectrum radio halo in the cluster A 697, which have been studied in detail in this thesis. Beyond these, candidate very steep spectrum radio emission has been also found at the centre of the cluster A 1682 (Venturi et al. 2009, Venturi et al. 2011 to be submitted).

We refer to Chapter 3 for a description of A 697 and for the study of its very steep spectrum radio halo. Here we summarize the properties of the remaining two clusters, and their USSRH.

- **A 521: the first USSRH.**

  A 521 is a massive and X–ray luminous ($M_V \sim 1.9 \times 10^{15}$ $M_\odot$; $L_{X[0.1-2.4keV]} \sim$ 8×10^{44} erg s^{-1}) merging cluster, located at redshift z=0.247. It host both a peripheral relic and a central giant radio halo (see Fig. 4.1, left panel), which

have been studied in detail at various frequencies (Giacintucci et al. 2008, Brunetti et al. 2008, Dallacasa et al. 2009). The relic source is detected up to 5 GHz, and its spectrum in the range 240 MHz–5 GHz is well fitted by a single power law with spectral index $\alpha \simeq 1.5$ (stars in Fig. 4.1, right panel). The central radio halo is barely detected at high frequencies (*i.e.,* 610 MHz) and becomes clearly visible only below 330 MHz (see Fig. 4.1, left panel). Its integrated spectrum is very steep, with $\simeq 1.9$ in the range 240 MHz-1.4 GHz (filled dots and upper limits in Fig. 4.1, right panel), thus it is considered the prototypical USSRH (see also Sect. 2.3).
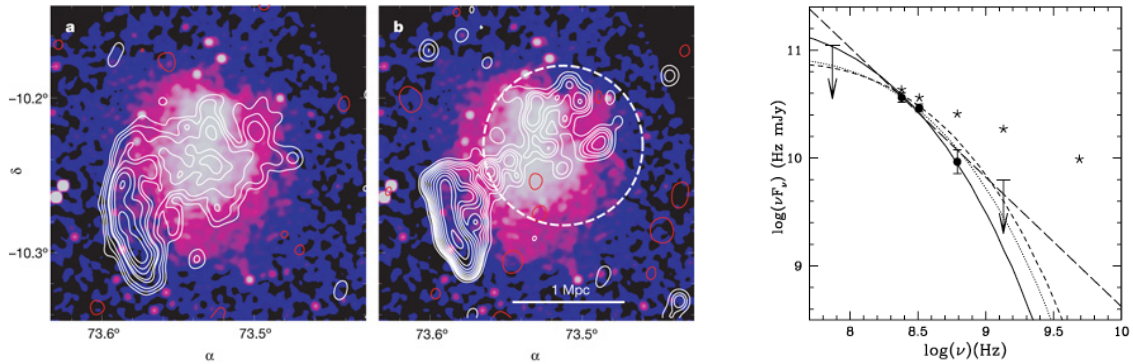

Figure 4.1: *Left* – GMRT low resolution ($35'' \times 35''$) radio contours at 240 MHz (left image) and 610 MHz (right image) of the diffuse emission in A 521 (after subtraction of discrete sources), overlaid on the Chandra 0.5-4 keV X-ray image. The rms noise levels are 220 mJy/beam and 58 mJy/beam at 240 and 610 MHz, respectively. *Right* – Energy spectrum of the USSRH in A 521 (black points). For comparison, stars represent the energy spectrum of the radio relic and the lines represent fits to the halo spectrum from the re-acceleration model (except for the long dashed lines, which refers to secondary models). From Brunetti et al. 2008.

- **A 1682: a very complex cluster**.

  A 1682 is an X-ray luminous ($L_{X[0.1-2.4keV]} \sim 7 \times 10^{44}$ erg s^{-1}) galaxy cluster at redshift z = 0.2260 ($1'' = 3.953$ kpc). X-rays and optical observations suggest the cluster is experiencing a recent merger (*e.g.* Dahle et al. 2002).

  Observations with the GMRT at 610 MHz (as part of the GMRT radio halo survey, Sect. 2.2) showed that the cluster is very complex in the radio band (Venturi et al. 2008). Figure 4.2 (right panel) shows that a few discrete extended sources characterize the central cluster radio emission, the prominent diffuse source being likely a wide angle tail galaxy. Beyond these individual sources, Venturi et al. (2008) reported on the presence of positive

residuals, providing some indication of low surface brightness cluster-scale diffuse emission in which the wide-angle-tail is embedded (Figure 4.2, right panel, blue contours). GMRT follow up observations of the cluster at 240 MHz clearly revealed the presence of a new diffuse component beyond the features already visible at 610 MHz (indicated by the arrow in right panel of Figure 4.2); this is coincident with a similar feature on the VLSS, as seen in Figure 4.2 (left panel).

Images of residual emission obtained after the subtraction of the contribution of the individual sources at both frequencies revealed the presence of residual flux density on larger scale, in a region of $\sim$1 Mpc within the centre. The estimated spectral index $\alpha_{240\text{MHz}}^{610\text{MHz}} \gtrsim 2$, suggesting that the central diffuse emission is probably another case of USSRH. (Venturi et al. 2011, to be submitted).
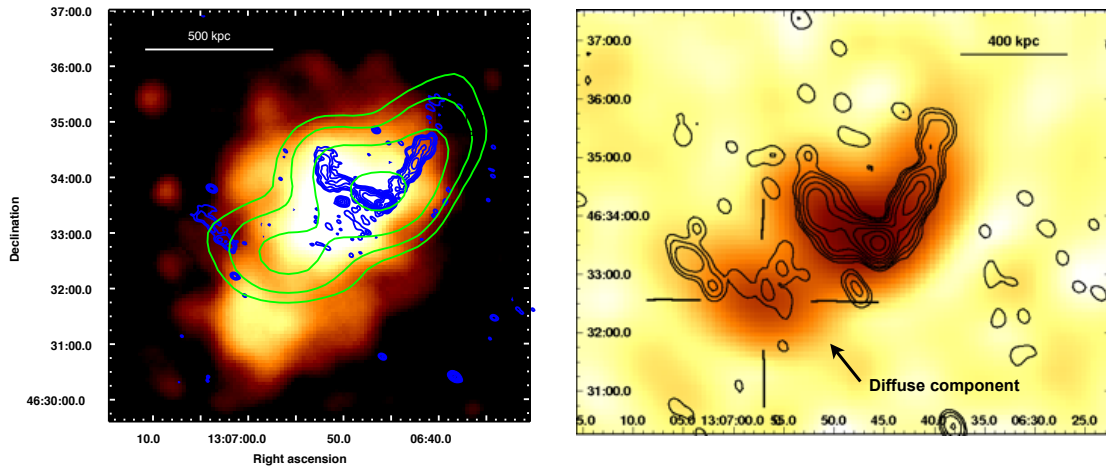

Figure 4.2: *Right panel*: 610 MHz (blue) and VLSS 74 MHz (green) radio contours of A 1682, overlaid on the X-ray Chandra image (in the 0.5-5.0 keV band). The resolution of the 610 MHz image is $6.1'' \times 4.1''$ and the first contour level is 0.2 mJy/b; the resolution of the 74 MHz image is $75'' \times 75''$ and the first contour level is 0.29 Jy/b. *Right panel*: GMRT 240 MHz contours of A 1682 overlaid on the VLSS 74 MHz image (yellow scale). The resolution of the 240 MHz image is $18'' \times 13''$, the rms (1σ) level is 0.7 mJy/b and the first contour is 2.1mJy/b. From Venturi et al 2011, to be submitted.

For all the three clusters, high sensitivity GMRT follow-up observations at 150 MHz were performed, in order to constrain the low frequency end of the spectra of the two USSRH and to carry out an appropriate study of the candidate steep spectrum diffuse emission in A 1682.

In this chapter we introduce the observations of all the clusters and we describe the data reduction. Preliminary images and results are presented for A 697 and A 521. Data reduction for A 1682 is in progress.

4.3 GMRT 150 MHz observations

A GMRT observation at 150 MHz covers a large field of view (the primary beam is 3.1°), and samples a wide range of spatial frequencies, that allows to produce images in a range of angular resolutions ($\sim 20'' - 7'$). The largest detectable structure is $\sim 1.1°$ (see Table 2.1).

In Table 4.1 we report the main parameters of the GMRT 150 MHz observations. In order to achieve high sensitivity and to ensure an appropriate uv-coverage, each cluster was observed for a total time of 10 hours. An example of the uv-coverage for these observation is shown in Fig. 4.3. All the observations were performed recording only one sideband, in the default spectral line mode, with the 8 MHz band divided into 128 channels, each 62.5 kHz wide. All the clusters have been observed in the nighttime, in order to minimize the radio frequency interference (RFI) as well as to avoid interference by the sun.

Table 4.1: Summary of GMRT 150 MHz observations

Cluster name	RA_{J2000}	DEC_{J2000}	z	Obs. Date	ν (MHz)	$\Delta\nu$ (MHz)	Obs. time (hours)
A 0521	04 54 09.1	-10 14 19	0.2475	2009, Aug 16	153	8	10
A 1682	13 06 49.7	+46 32 59	0.2260	2009, Aug 17	153	8	10
A 0697	08 42 53.3	+36 20 12	0.2820	2009, Aug 30	153	8	10

4.4 Data reduction at 150 MHz

The 150 MHz dataset of A 697 was reduced and analyzed using the NRAO Astronomical Image Package (AIPS). Sources 3C 147 and 3C 286 were observed at the beginning and the the end of the observing run, respectively, and were used as flux density and bandpass calibrators. The source 0735+331 was used as phase calibrator.

Initial editing of all visibility data was performed, including the removal of dead or malfunctioning antennas, bad baselines and timeranges, systematic removal of
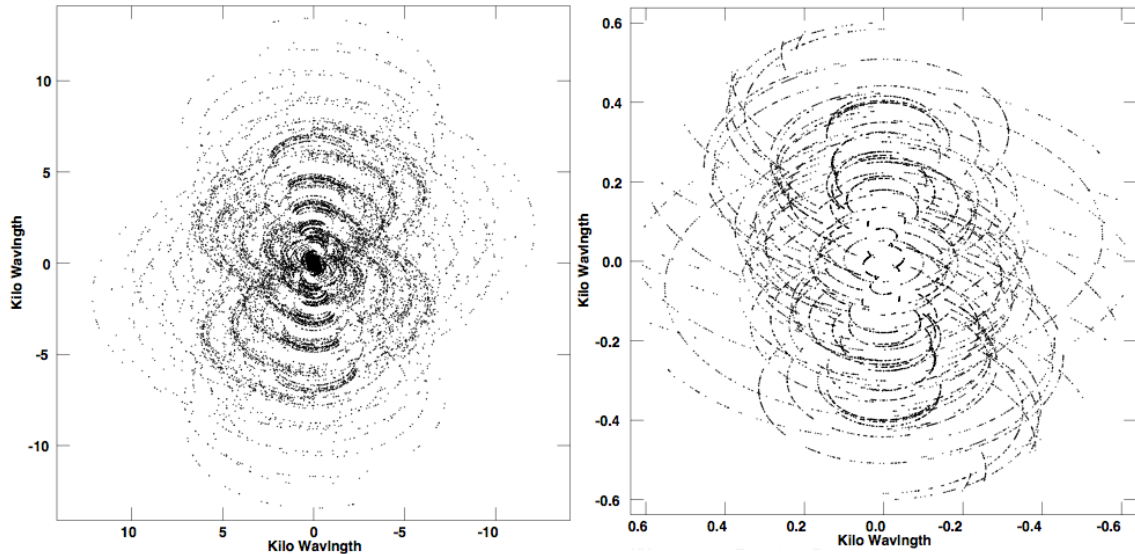
Figure 4.3: Example of uv-coverage for 10 hours GMRT observations at 150 MHz. In the left panel is shown the whole uv-plane sampled. The inner portion, showing only baselines shorter than 0.6 kλ (*i.e.,* corresponding to the radio halo angular scale) is plotted in the right panel.

the first few seconds of each observing scan due to potential system instabilities. Standard procedures of absolute flux density, gain, and bandpass calibration were carried out. A channel free of RFI was chosen to normalize the bandpass for each antenna. The data for antennas with high errors in antenna-based solutions were inspected and flagged over certain timeranges. Channel and time based editing of data corrupted by strong RFI were performed automatically, using a median filter with a 5σ threshold (by means of the AIPS task FLGIT). Low level RFI and data affected by ionospheric scintillation were then manually edited out (using AIPS tasks SPFLG, TVFLG, UVFLG).

Extended emission is detected on the shortest baselines, which are also more affected by RFI. Particular care is thus required, and manual editing was preferred with respect to a priori automatic RFI editing algorithms, to avoid possible loss of sensitivity due to automatic removal of short baselines.

The RFI at 150 MHz is particularly severe, much worse than at higher frequencies. In Figure 4.4 examples of typical RFI for a short (left panel) and a long (right panel) baseline in the raw data (before any editing) are shown. Note in particular the very strong broad band RFI affecting short baselines in 10 consecutive channels, and drifting over 2 MHz in frequencies over the total $\sim$ 6 hours on source time.

Further narrow band RFI affected some channels for limited amount of time. A plot of the raw visibility amplitudes versus uv–distance for one channel is shown in Figure 4.5 (top panel): strong RFI are visible at various uv–distances, ranging from hundreds to almost ten thousands Jy. For comparison, the same plot for the final (after editing and calibration) dataset is also shown (bottom panel).

After the bandpass calibration, the central channels were averaged into 22 channels,
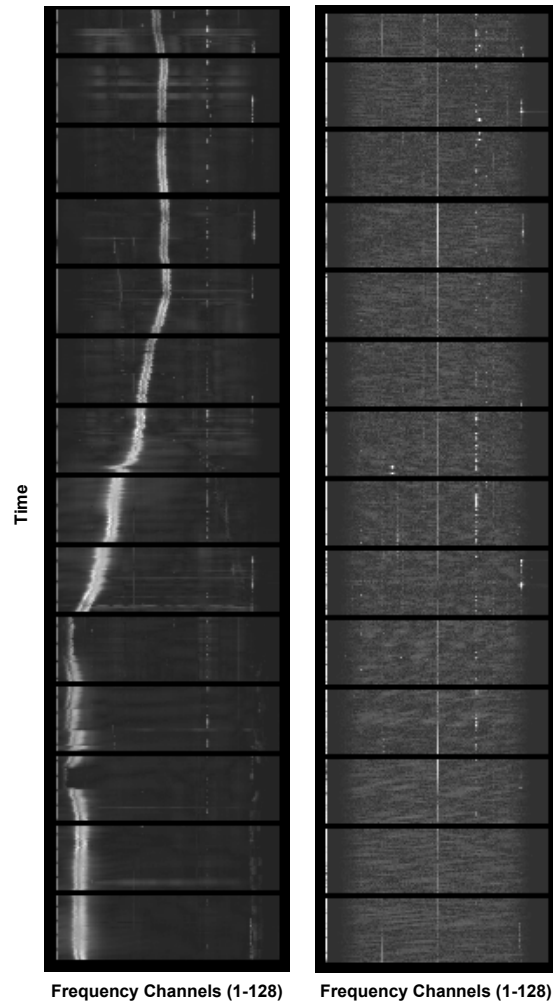
Figure 4.4: Examples of RFI affecting the raw data at 150 MHz. The images represent the distribution of the u-v data (amplitudes), in a grid with spectral channels on the x-axis and time on the y axis. A short and a long baseline are shown on the left and right panel, respectively.

each 0.25 MHz wide, for a total final bandwidth of 5.6 MHz (the few first and last channels being discarded as they are noisy). This choice allowed to reduce the data set size, while avoiding the significant bandwidth smearing over the whole primary

Figure 4.5: Visibility amplitudes in kJy (top) and Jy (bottom) versus uv-distance (kλ), before (top) and after (bottom) editing of RFI.

beam.

In each stage of self-calibration, we used the wide field imaging technique, to minimize the effects of non coplanar baselines. We covered a field of view of $\sim$5$\times$5 square degrees, with 121 facets (each wide $\sim$0.6°). This allowed to remove the sidelobes of strong sources located far away from the field centre, outside the GMRT primary beam ($\sim$3°, see Table 2.1).
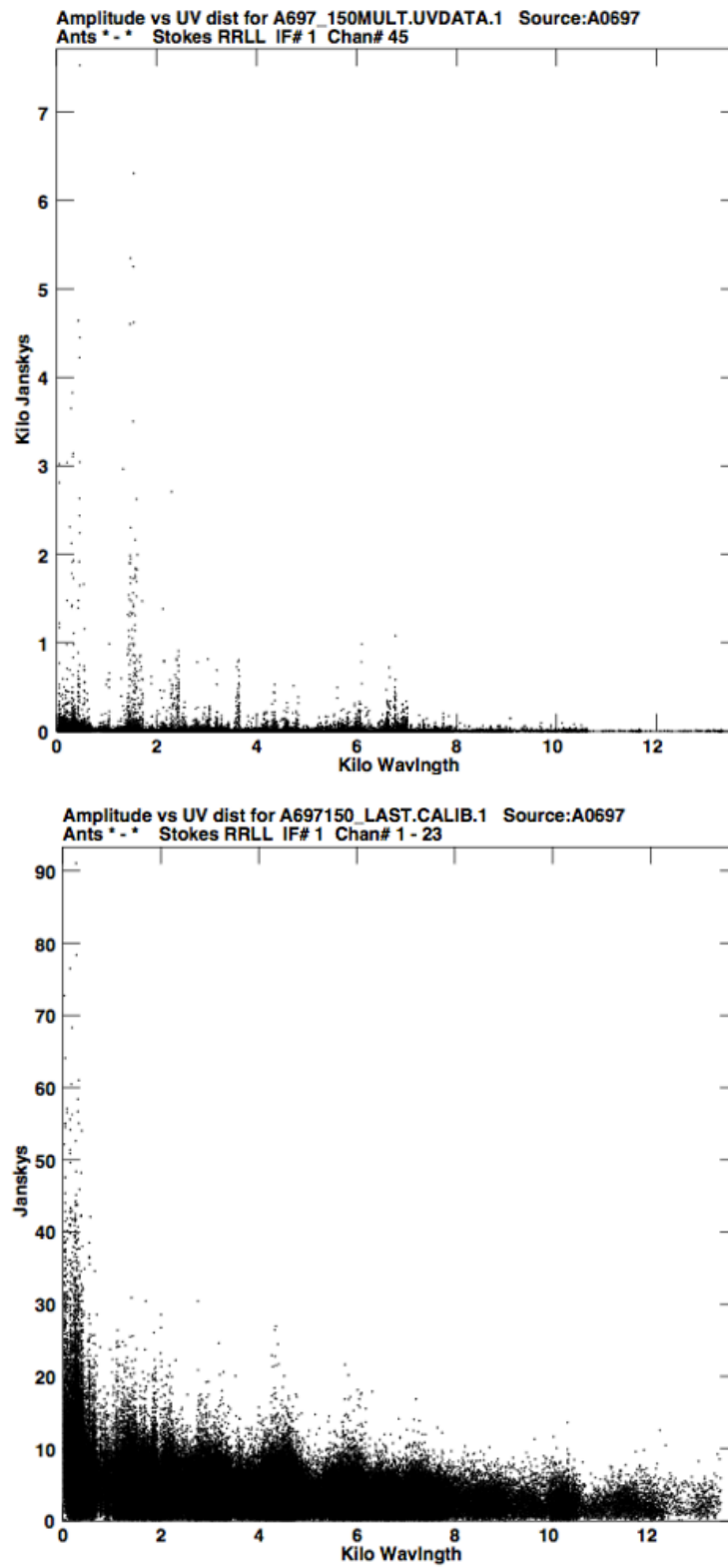We found that ionospheric effects only modestly affect the image, thus we used a standard self-calibration procedure (no peeling technique was needed, Sect. 4.1).

A few rounds of phase-only self-calibration were performed. During this process, the source model was temporarily subtracted from the visibility data, followed by flagging of excessive residual visibility amplitudes.
Preliminary clean images were then produced. The 1σ rms level reached in the full resolution ($23.9'' \times 19.7''$) image is around 1 mJy b^{-1}. The uncertainty in the calibration of the absolute flux density scale is $\lesssim$ 15%.

4.5   A 697

4.5.1   The radio halo at 150 MHz

The top panel of Fig. 4.6 shows the preliminary full resolution ($\sim 26'' \times 19''$) contours of the central $24' \times 24'$ squared region around A 697 ($\sim 6 \times 6$ Mpc^2, *i.e.,* about the cluster virial radius; see Sect. 3.3.2). The rms level in the image is 1 mJy b^{-1}. The diffuse radio emission associated with the radio halo is visible around the cluster centre.

In the bottom panel of Fig. 4.6, a low resolution ($\sim 47'' \times 41''$) image of the radio halo region is shown as contours (starting from $\pm 2.5\sigma = 5$ mJy b^{-1}), overlaid to the 325 MHz GMRT image (in grey scale), obtained after the subtraction of discrete radio sources (same as in Fig. 3.2 in Sect. 3.3.3), and convolved with the same beam. The morphology of the diffuse emission is rather patchy, mostly due to the relatively low surface brightness with respect to the rms noise. The emission at 150 MHz is mainly elongated in the South-East/North-West direction. In addition to this main feature, positive residuals of emission indicate an extension in the East-West direction. These residuals are spread around an area covered by the halo at 325 MHz image, and we believe that they are part of the radio halo. The halo is very extended, with largest linear size of $\sim$1.3-1.4 Mpc. Compared to the 325
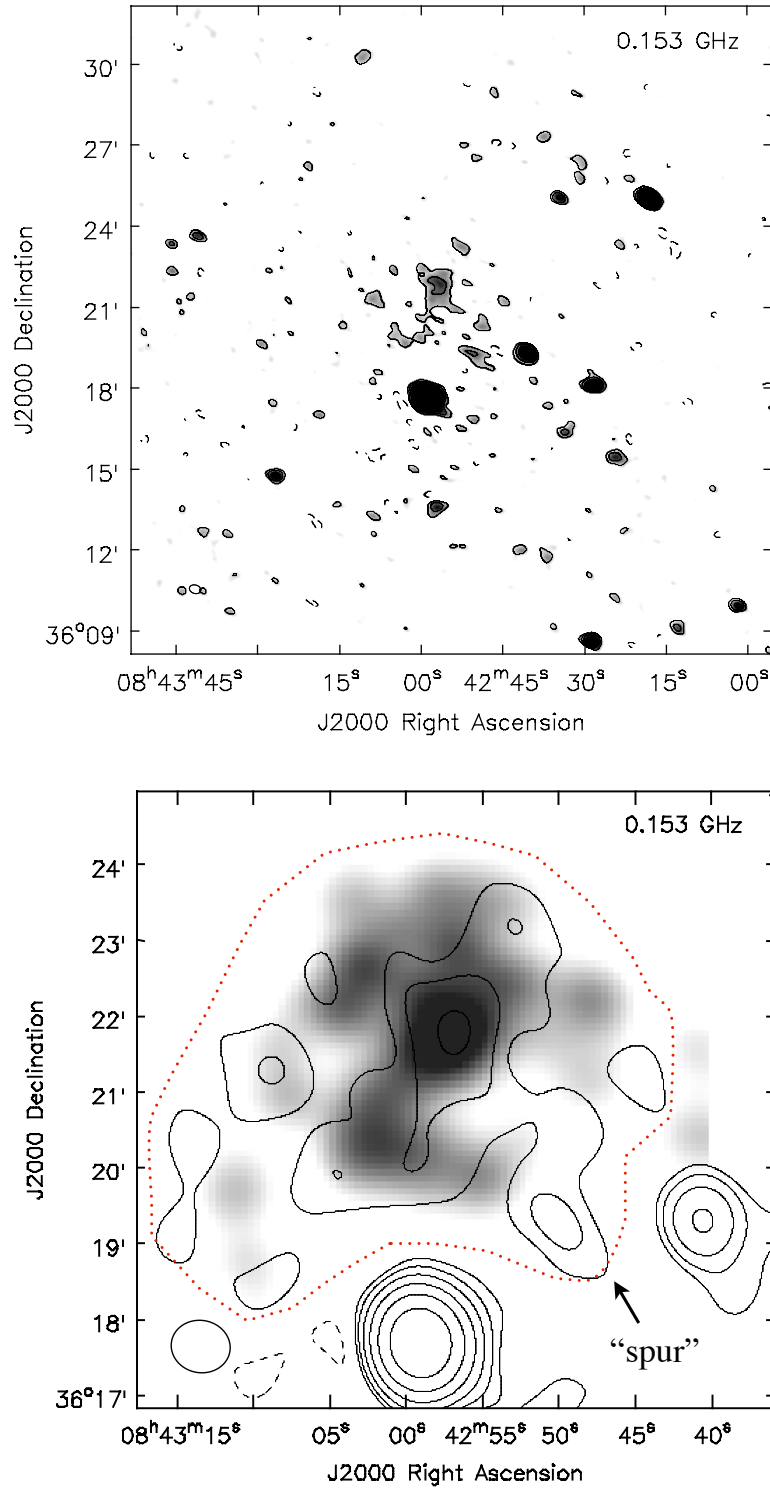
Figure 4.6: *Top panel* GMRT 150 MHz image of the central field of A 697. The resolution is $\sim 26'' \times 19''$. Contours are spaced by a factor 2, starting from $\pm 3\ \sigma$ level (i.e. ~ 3 mJy b^{-1}). *Bottom panel* GMRT 150 MHz contours of the radio halo in A697, overlaid on the GMRT 325 MHz image (grey scale); the two images has the same restoring beam ($\sim 47'' \times 41''$). Contours starts from $\pm 2.5\ \sigma$ level (i.e. ~ 5 mJy b^{-1}), and are spaced by a factor 2.

MHz image, it has a similar morphology in the central ~ 1 arcmin, and also shows a similar feature in the southern part. The data reduction is still in progress, aiming at refining the phases and lowering the rms noise level in the central cluster region, and better image the radio halo in its full extent (*e.g.* after subtraction of the discrete sources at the cluster centre, as done at 325 MHz in Sect. 3.3.3).

In order to derive a flux density measurement of the radio halo emission, we have to note that:

(i) the total contribution of discrete sources embedded into the diffuse halo emission (sources A, D, G identified at 330 MHz, Sect. 3.3.3) is estimated to be ~ 20 mJy at this frequency. We subtract such amount from the total flux density measurements of the halo region (obtained by integrating the low resolution image over the the area indicated by the dotted line in Fig. 4.6);

(ii) there is a spot of emission which we term "spur" in the South-West region of the cluster, which is not visible at higher frequencies. The "spur" is not associated with any background/foreground optical counterpart: there are no object in the SDSS images in the area covered by its emission. Its radio spectrum is very steep, and its nature is unclear. The total flux density associated with this feature is ~ 90 mJy (measured on the low resolution image; Fig. 4.6, bottom panel).

The flux density to be considered for the halo emission at 150 MHz is $S_{150\mathrm{MHz}}=252\pm38$ mJy, if we include the whole patchy diffuse emission, while it is $S_{150\mathrm{MHz}}=164\pm25$ mJy in case we exclude the "spur" contribution.

4.5.2 Spectrum of the radio halo

We combine the new 150 MHz measurements with the flux densities at 325 MHz, 610 MHz and 1.4 GHz (see Sect. 3.4, Table 3.4) to derive the integrated spectrum of the radio halo in the frequency range 150 MHz–1.4 GHz. The new spectrum is shown in Fig. 4.7. The value obtained by integrating over the whole diffuse emission (including the spur "spur; circle point in Fig. 4.7) is still consistent with a single power law with $\alpha \simeq 1.7$. This is in agreement with what found in our previous analysis (Sect. 3.5.2). If we do not consider the "spur feature as part of the diffuse halo emission (square point in Fig. 4.7), the spectrum of the radio halo may show a flattening at low frequencies. After further improvements of the image and appropriate subtraction of discrete sources, we will be able to clarify this point.
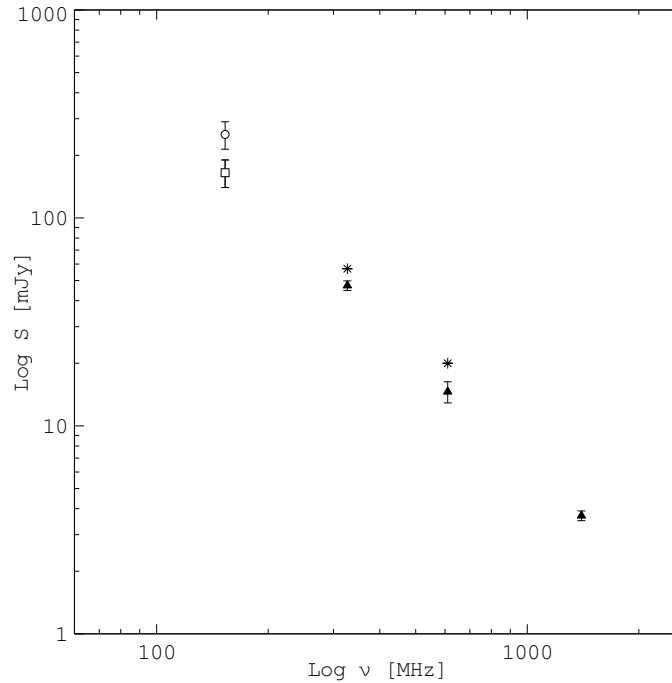
Figure 4.7: Integrated radio spectrum of the halo. The flux density values at 325, 610 and 1400 MHz (triangles and stars) are from Sect. 3.4 and Tab. 3.4, same as in Fig. 3.6. The square and the circle indicates the the preliminary values at 150 MHz, obtained by excluding or including the "spur" contribution from the radio halo emission, respectively (see text, Sect. 4.5.1 and 4.5.2).

4.5.3 The field sources

Figure 4.8 shows the full resolution image of the whole $\sim 5° \times 5°$ area covered by our observations. The angular resolution is $24'' \times 20''$ (p.a. 71°). The average 1σ rms level is around 1 mJy b^{-1}. Only the brightest sources (*i.e.,* with peak flux density $\gtrsim$ 10 mJy) are represented by the color scale in this image. However, the presence of strong point sources in the field limits the local dynamic range around them. The dashed circle indicates the area corresponding to the A 697 virial radius ($R_V = 2.9$ Mpc).

It is clear from Fig. 4.8 that low frequency GMRT observations may have a number of byproducts. In fact, a large number of radio sources have been detected, and may be used for many purposes, as for example: *(i)* study of individual objects falling in the field of view; *(ii)* study of extended radio source, like doubles (FR-II type); *(iii)* source counts at 150 MHz. In particular, source counts studies at $\nu \sim 150$ MHz are stuck to the Cambridge surveys, whose sensitivity is about two orders of

magnitude worse (*e.g.* Hales et al. 2007), and with a broader beam ($> 1'.2$). At the moment, a survey is under realization at the GMRT (TGSS[1]), with expected rms noise of ~ 1 mJy.

We can derive radio source counts from our image (Fig. 4.8); we considered a square area of 2000×2000 pixels corresponding to 2.2 square degrees (indicated by the dashed square in Fig. 4.8). The area was chosen at the pointing centre in order to minimize the noise increase with distance from the pointing when the primary beam correction is considered. We found 744 sources with peak exceeding 5 times the local rms noise, typically of 0.72 mJy. All the sources were fitted with 2-D Gaussian components allowing the AIPS task SAD (Search And Destroy) to solve for position, peak and integrated flux densities and major and minor axes, along with the p.a. of the major axis. We run SAD down to 3 sigma peak flux density, but among the sources found by the algorithm we selected only those with peak intensity > 3.6 mJy. Source counts were computed considering the integrated flux density, in order to take into account source extension. Components were plotted onto contours and inspected to find the very few cases in which a single source is accounted for by two or more Gaussian components. All flux densities are corrected for the primary beam attenuation, whose effects are an increased rms noise level at the edges of the area considered here.

The source counts are presented in Fig 4.9 and possess the well known characteristics seen at higher frequencies. A single power law is not adequate to represent the observations. The profile is complex, showing a flattening at low flux densities ($\lesssim 10$ mJy, due to incompleteness), a "knee" around 20 my, and a steepening above 800 mJy. This preliminary result will be complemented by a similar analysis on the fields around the other two clusters observed.

Beyond the many point sources, the field image is populated by a large number of double-lobed radio galaxies. Figure 4.10 reports some examples: a narrow angle tail radio galaxy (upper panels), an asymmetric double source (middle panels), and a classical double-lobed source (lower panels). The images illustrate how the combination of angular resolution and low frequency of these observations is helpful in classifying the morphology of extended radio galaxies.
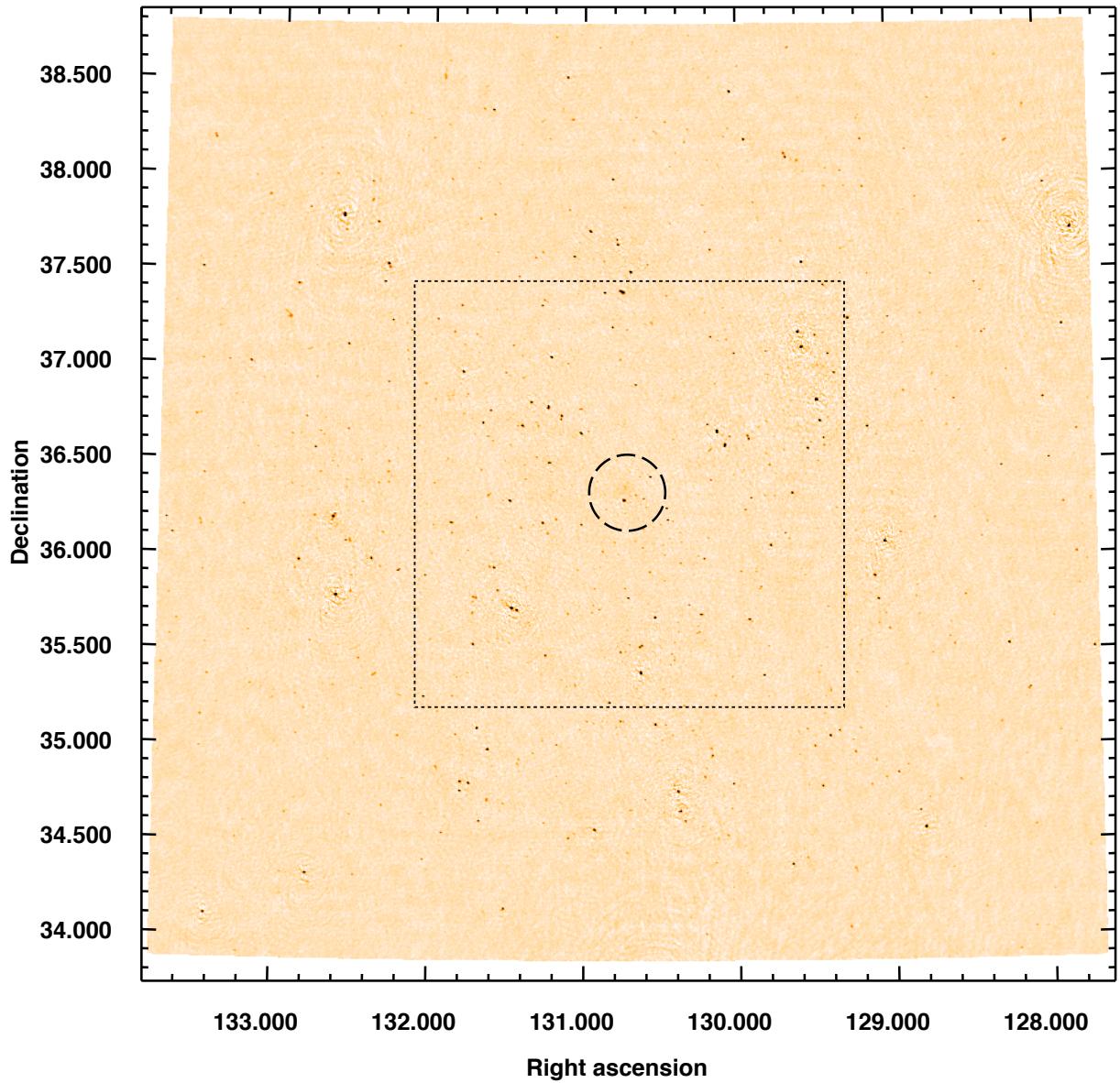
---

[1]http://tgss.ncra.tifr.res.in/

Figure 4.8: GMRT 150 MHz image of the entire imaged area centered on A 697. The dashed circle indicates the area corresponding to the cluster virial radius ($R_V = 2.9$ Mpc); The dashed square corresponds to the area chosen to derive source counts (see Sect. 4.5.3).
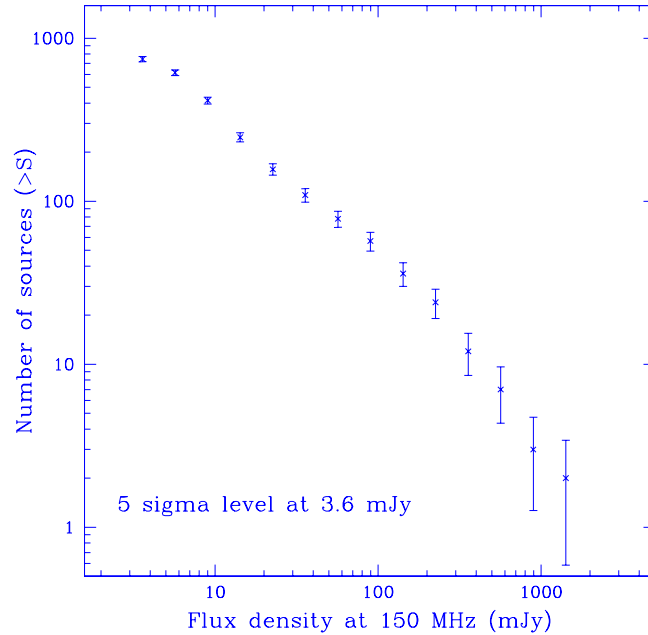
Figure 4.9: Source counts, shown in the classical LogN–LogS diagram, derived from the 2.2 square degrees area (see text, Sect. 4.5.3), and logarithmically binned in flux density (ΔLogS=0.2). All the 774 sources are plotted. Incompleteness is evident in the last bin at least.

4.5.4 A candidate diffuse source

Among the many extended sources imaged at 150 MHz, we found an intriguing diffuse source, which we call GMRT–J085210+363503 (referred to the coordinates of the center of the emission). The full resolution contours of this source are shown in Figure 4.11 (right panel). The source is located far from from the A 697 centre, at a projected distance of $1.88°$ in the South-East direction. It has a regular and very elongated shape, mainly extended in the North-West/South-East direction. The largest angular scale of the source is ~ 7.5 arcmin along the major axis, and $\sim$2-2.4 arcmin along the transversal direction, as measures from the first 2.5σ contour. The flux density is ~ 230 mJy, obtained by integrating the area within the first 2.5σ contour. No obvious residuals are present in the clean image, thus we believe that this is real diffuse emission, not due to artifacts in the image.

In search for further information, we inspected the NVSS, FIRST and WENNS images in this region. The diffuse source is not detected in any of these images. Labels S1, S2, S3, S4 in Fig. 4.11 indicate the point sources identified in the FIRST, NVSS, and WENSS catalogues.
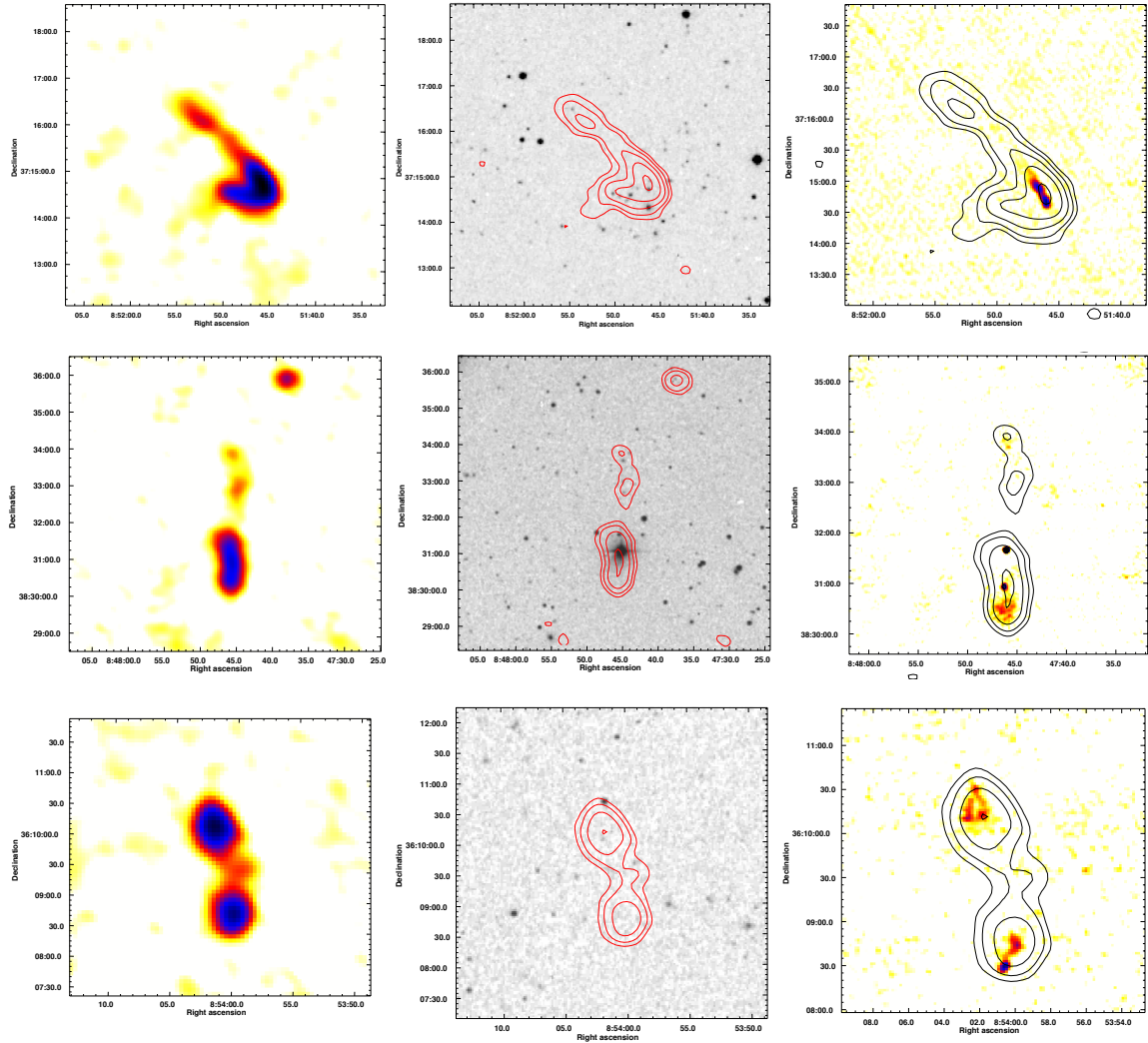
Figure 4.10: GMRT 150 MHz full resolution images of three extended radio galaxies in the observed field. Images are not corrected for the primary beam; the local rms around each source is $\sim$0.5 mJy beam^{-1}. *Left panels*: images in color scale. *Central panels*: 150 MHz contours, spaced by a factor of 2, starting from $\pm 4\sigma$=2 mJy beam^{-1}, overlaid to the DSS–2 optical frame. *Right panels*: same contours are overlaid to the FIRST 1400 MHz image.

We searched in the NED (NASA Extragalactic Database[2]) catalogue for possible optical counterparts. The diffuse and extended nature of the source makes it difficult to associate it with an individual galaxy, and indeed no obvious optical counterpart was found (see left panel of Fig. 4.11). GMRT–J085210+363503 might be a cluster radio relic. We found two galaxy clusters within an area of 30′ from the centre of the source: NSC J085025+345720 (at z=0.16) to the South-East, and ZwCl 0850.6+3536

Figure 4.11: *Right panel*: 150 MHz image of the candidate diffuse source GMRT–J085210+363503. The resolution is $23.9'' \times 19.7''$. The local rms noise level is ~ 0.8 mJy b^{-1}. Contours are spaced by a factor of $\sqrt{2}$, starting from $\pm 2.5\sigma$. The image is corrected for the GMRT primary beam. *Right panel*: the same contours as in right panel (shown in red) are overlaid to the DSS–2 optical frame.

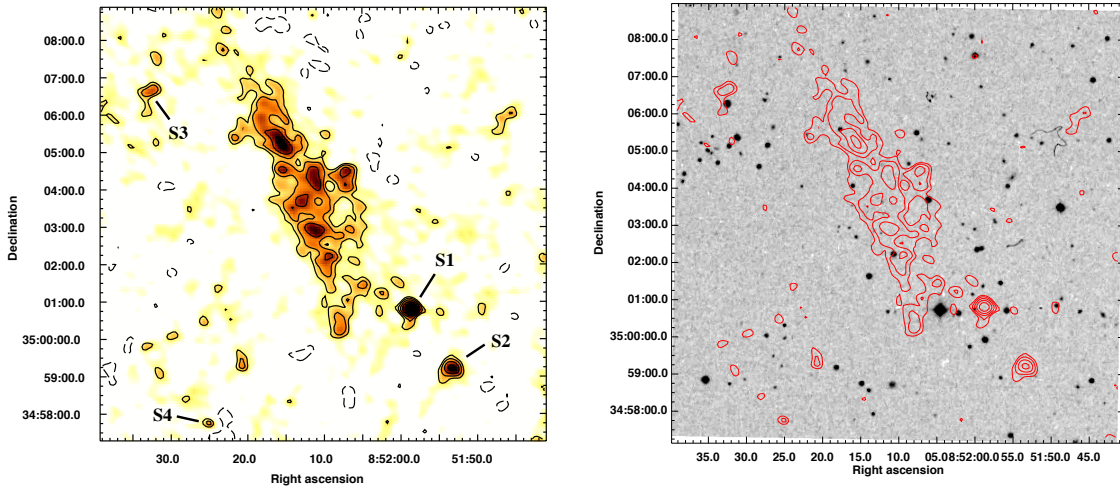to the North-West (with no redshift information available). However an association to these clusters is unlikely, due to their very large projected distance. Source S1 (Fig. 4.11) is located South-East to the extreme end of the diffuse source, and one possibility might be that GMRT–J085210+363503 is a tail of old radio emission associated with S1. However, it has no obvious optical galaxy counterpart; three SDSS sources located within the radio contours are unidentified, and no redshift information is available.

A connection to A 697 is ruled out since, at the cluster redshift, the projected distance of the source from the cluster ($\sim 1.88°$) corresponds to ~ 28 Mpc.

Future deep multifrequency radio observations pointed on this region will allow a proper imaging of this candidate diffuse radio source, and to study its properties.

4.6   A 521: preliminary images

Following the same procedure described in Sect. 4.4, we reduced the dataset of A 521, and obtained a preliminary image, after a few rounds of phase only self-calibration. The rms noise is still relatively high ($\simeq 1.5$ mJy/b at the center), and further self-calibration and editing of residual RFI is needed. This procedure is in progress.

In Fig. 4.12 we show the 150 MHz full resolution ($27.1'' \times 19.4''$) image of the A 521 field ($\sim 30' \times 30'$ around the cluster virial region, same as in Fig. 1 of Giacintucci et al. 2008). As seen at higher frequencies (Giacintucci et al. 2008), the field is dominated by the two extended radio galaxies (J0453–0957 and J0454–1006, located North of the cluster), and the cluster radio relic.
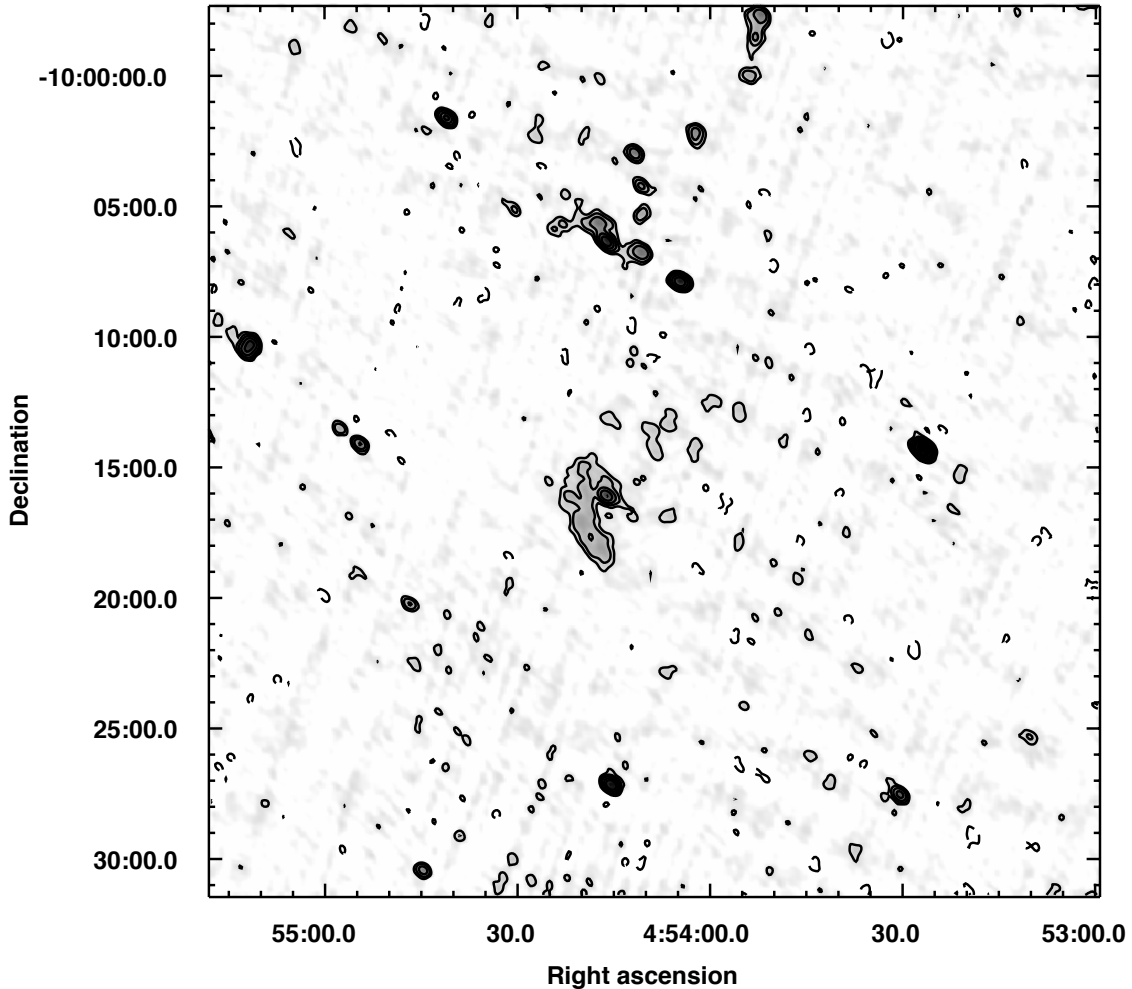
Figure 4.12: GMRT 150 MHz preliminary image of the central $\sim 30' \times 30'$ field around the cluster A 521. The resolution is $27.1'' \times 19.4''$. Contours are spaced by 2, starting from $\pm 3\sigma = 4.5$ mJy/b.

Fig. 4.13 (left panel) zooms in the central cluster region. The radio relic dominates this image. The dashed circle indicates the area corresponding to the radio halo (as detected at 240 MHz; see Fig. 4.1, left panel). The USSRH is barely detected in this image, due to the still relatively high rms; only the peaks of is low surface brightness diffuse emission are visible at this stage of the data reduction.
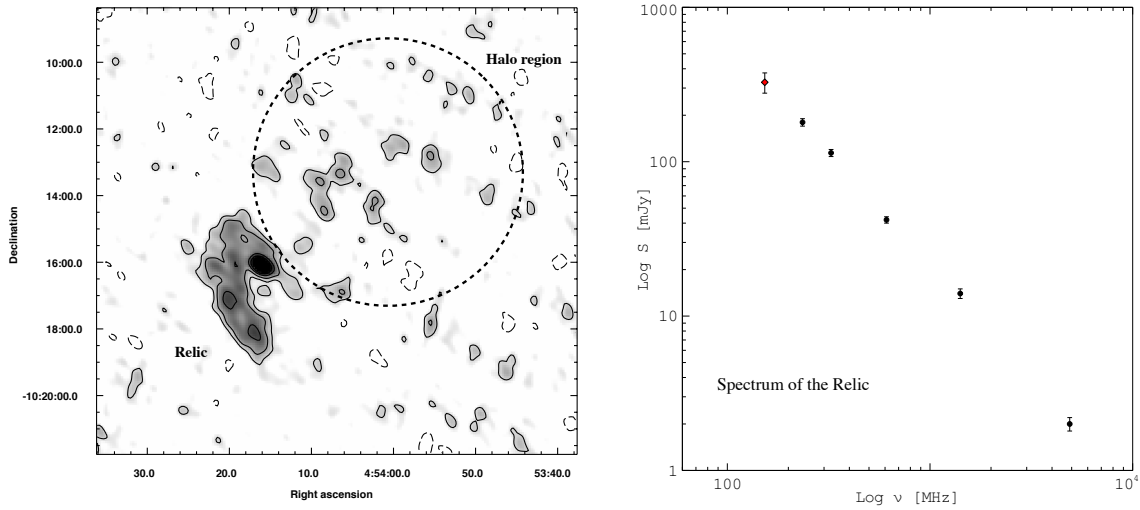
Figure 4.13: *Left*: GMRT 150 MHz preliminary image of the central cluster area A 521; contours starts from $\pm 2.5\sigma = 3.75$ mJy/b, and are spaced by a factor of 2. The dashed circle indicate the area covered by the radio halo. *Right*: Integrated spectrum of the radio relic. Black circels are the flux densities taken from Giacintucci et al. 2008; the red diamond is the preliminary flux density of the relic at 150 MHZ.

Although the image is still in a very preliminary stage, we can derive a measurement of the radio relic flux density at 150 MHz. By integrating the image over the relic region (following the first 2.5σ contour, and excluding the embedded source), we find $S_{150\text{MHz}}=327\pm49$ mJy. This value is consistent with the power law spectrum with $\alpha \sim 1.5$ observed in the frequency range 240 MHz – 5 GHz (see right panel of Fig. 4.13; Giacintucci et al. 2008). This suggests that the flux density scale at this frequency is correct, and we believe that the steep spectrum of the relic is a single power law at least down to 150 MHz. Further consistency checks are in progress.

We finally note that, with this new measurement at 150 MHz, the spectrum of the radio relic in A 521 is sampled over about 2 order of magnitudes in frequency. At present, such a wide spectral coverage is available only for the prototypical radio relic 1253+275 in Coma (see Sect. 1.6, left panel of Fig. 1.4; Thierbach et al. 2003).

Chapter 5

The shock front and the diffuse radio emission in Abell 754[*]

5.1 Introduction

As seen in Section 1.8 there is growing observational evidence of connection between cluster mergers and diffuse cluster radio emission. In particular cluster mergers generates shocks and turbulence in the ICM, that are expected to amplify the cluster magnetic fields and accelerate or re-accelerate cosmic ray particles from the thermal ICM or preexisting relativistic particles (Section 1.8).

Shock fronts represent a unique observational tool to study the physical processes in the ICM. They create sharp discontinuities in the cluster X-ray surface brightness images and allow to measure the gas velocities in the sky plane using X-ray imaging spectroscopy (*e.g.* Markevitch et al. 1999). Only four merger shock *fronts* have been reliably detected so far, (in 1E 0657–56, Markevitch et al. 2002, in A 520 Markevitch et al. 2005, in A 2146, Russell et al. 2010). This is due the still low sensitivity of X-ray instruments in the low surface brightness regions where the fronts are expected to form, combined with projection effects (see Section 1.8.1).

In this chapter, we present a detailed multiband analysis of the merging cluster Abell 754. We report on the detection of a new shock front, based on the analysis of *Chandra* observations. Moreover, we study the spectrum of the diffuse cluster radio emission at its centre, on the basis of new low frequency 330 MHz GMRT observation and VLA archival data at 1.4 GHz. Finally we study the connection

---

[*]Macario et al. 2011, ApJ, 728, 82

between the shock and the diffuse cluster radio emission.

5.2 The prototypical merging cluster A754

A754 is a rich nearby cluster at $z = 0.0542$ (Struble & Rood 1999) undergoing of a violent merger. It has been actively studied in the optical and X-ray bands, and is considered the prototype of a major cluster merger. Previous studies revealed that the cluster has a complex galaxy distribution (Fabricant et al. 1986, Zabludoff & Zaritzki 1995), X-ray morphology, and gas temperature structure (Henry & Briel 1995; Henrikesen & Markevitch 1996; Markevitch et al. 2003b, hereafter M03; Henry et al. 2004). These data indicate that A754 is undergoing a major merger of two components along an east-west axis, probably with a non-zero impact parameter. Hydrodynamic simulations were able to reproduce most of the observed X-ray features in A754 by considering an off-axis collision between two subclusters with a mass ratio of 2.5:1 (Roettiger et al. 1998). *Chandra* data suggested that the merger may be more complex, possibly involving a third subcluster or a cloud of cool gas decoupled from its former host subcluster (M03).

Krivonos et al. (2003) reported an edge-like surface brightness feature in the *ROSAT* PSPC image of the cluster, located east of the core, which looked like a shock front. They modeled it with a radial density profile with a jump, deriving a Mach number $M = 1.71^{+0.45}_{-0.24}$ from this jump under the assumption that this is indeed a shock front. This brightness feature was also apparent in the *Chandra* image by M03, but it was at the edge of the *Chandra* field of view, which did not allow its detailed study. Henry et al. (2004) presented a temperature map of the cluster from an *XMM-Newton* observation. The presumed post-shock region was shown to be hot, as expected for a shock front. However, because the X-ray brightness ahead of this front is very low, the *XMM* observation did not have sufficient sensitivity to determine the temperature in the pre-shock region, in order to detect the expected temperature jump. They were only able to derive a temperature in the annulus around the cluster that included the pre-shock region (region 12 in Fig. 6 of Henry et al. 2004), but that annulus is dominated by emission from regions on the other side of the cluster, unrelated to the shock front. We note that many features that look like shocks in the X-ray images turned out to be "cold fronts" (Markevitch & Vikhlinin 2007), and the difference between these phenomena is the sign of the

temperature jump at the feature. Here we present a direct temperature measurement in the pre-shock region from a new *Chandra* observation.

A754 also exhibits evidence for ultrarelativistic electrons and magnetic fields that coexist with the ICM. Fusco-Femiano et al. (2003) reported a 3σ hard X-ray excess at $E > 45$ keV with *BeppoSAX*, which may come from inverse Compton scattering of the Cosmic Microwave Background (CMB) photons on relativistic electrons. A clear evidence of nonthermal emission in A754 comes from the radio observations. A radio halo was detected at 74 MHz, 330 MHz and 1.4 GHz with the VLA (Kassim et al. 2001, hereafter K01; Bacchi et al. 2003, hereafter B03, and references therein). Moreover, the presence of two peripheral radio relics were reported in K01, East and West of the radio halo. Only the eastern emission was seen in B03. The whole cluster diffuse radio emission has been recently studied in the frequency range 150–1360 MHz by Kale et al. (2009).

At the redshift of A 754 (z=0.0542), the cosmology adopted in this work leads to a linear scale $1'' = 1.054$ kpc.

5.3 Chandra observations and data analysis

A754 was first observed with *Chandra* ACIS-I in October 1999 (OBSID 577). The pointing was centered on the cluster center and used by M03 to study the temperature structure. In Febraury 2009, a new long *Chandra* ACIS-I observation (OBSID 10743) was pointed on the putative shock front, in order to derive the temperature profile across the shock. The new exposure partially overlaps the old one (see Fig. 5.1), thus in this analysis we use both observations for the spectral analysis of regions where they overlap.

Both datasets were processed and cleaned in a standard way (e.g., Vikhlinin et al. 2005). The data were cleaned of flares and the blank-sky datasets were normalized as described in Markevitch et al. (2003a). OBSID 577 had little flare contamination and the final clean exposure was 39 ks. No background flares were present in the new observation, so we used the full exposure of 95 ks. The old observation was taken in FAINT mode, while the new one in VFAINT, which allowed additional background filtering to be applied. The detector + sky background was modeled using the blank-sky background datasets corresponding to the dates of observations (periods B and E, respectively). We normalized the blank-sky backgrounds using

the the ratio of counts in the high-energy band 9.5–12 keV, which is free from sky emission. This correction was within 10% of the exposure ratios, as expected. We have verified the use of the blank-sky background for the background-critical OBSID 10743 by extracting spectra from regions free of the cluster emission in the ACIS-I chips and in chip S2. For both these spectra, residuals after subtracting the blank-sky background as described above were consistent with zero.

All point sources were masked out for the extraction of brightness profiles and spectra. The instrument responses for spectral analysis were generated weighting the detector ARF and RMF with the cluster brightness within each spectral extraction region (Vikhlinin et al. 2005). We used the most recent calibration products — namely, version N0008 for the telescope effective area, N0006 for the CCD quantum efficiency and gain files, and N0005 for the ACIS time-dependent low-energy contaminant model. We also assessed the systematic uncertainty of our results by using a newer, experimental update to the ACIS contaminant model (A. Vikhlinin, private communication; see below).

Figure 5.1 shows a slightly smoothed ACIS image of the cluster in the 0.5–4 keV band, obtained by co-adding the two observations and correcting for exposure nonuniformity. As found by previous studies, the cluster undergoes a complex merger with the main axis along the NW-SE direction. The image clearly shows a brightness edge to the east of the dense elongated core, perpendicular to the merger direction. This is the putative shock front reported by Krivonos et al. (2003). The new observation provides sufficient statistics to determine the exact nature of this feature.

5.3.1 Density profile across the edge

Figure 5.2 shows a radial X-ray surface brightness profile across this edge, extracted in a 25° sector shown in Fig. 5.1. To facilitate proper geometric modeling, the sector is centered on the center of curvature of the brightness edge (dashed white circle in Fig. 5.1) and encompasses its most prominent segment (avoiding the apparent decrease of the edge brightness contrast at greater opening angles). All point sources were carefully masked. The energy band for the profile was restricted to 0.5–4 keV to minimize the dependence of X-ray emissivity on temperature and maximize the signal-to-noise ratio. Only OBSID 10743 is used for the brightness profile, since

the earlier observation does not cover the pre-shock region. The exposure of this observation alone is more than sufficient for the post-shock region. We consider only the region outside the bright elongated core, which is obviously unrelated to the shock.

The brightness profile across the edge (Fig. 5.2a) exhibits the typical shape of a projected spherical density discontinuity (Markevitch et al. 2000), and we fit it with such a model, under the assumption that the curvature along the line of sight is the same as in the image plane. The model radial density profile that we use consists of two power laws, $\rho \propto r^{\alpha_1}$ and $\rho \propto r^{\alpha_2}$, on two sides of the edge, with an abrupt jump at the edge (Fig. 5.2b). For each set of the profile parameters, we projected the corresponding emission measure profile onto the image plane and fit to the observed X-ray brightness profile (Fig. 5.2a), treating the slopes and the radius and amplitude of the jump as free parameters. The fit was restricted to the interesting radial range — staying as close as possible to the edge on the inside in order to avoid contamination from unrelated core structure, but extending as far as possible on the outside for proper deprojection (see dashed ticks on the outer sides of the sector in Fig. 5.1). As seen from Fig. 5.2a, the model well fits the data, with $\chi^2 = 57.7$ for $37-5$ degrees of freedom, providing an adequate qualitative description of the profile. The best-fit density jump, after a 3% correction of the $0.5 - 4$ keV Chandra brightness for the measured temperature difference across the edge (see Sect. 5.3.2 below), is $\rho_2/\rho_1 = 1.80^{+0.20}_{-0.15}$. The confidence interval is evaluated by allowing all other model parameters to be free.

5.3.2   Temperature profile across the edge

We now extract spectra from several radial bins in the same sector across the density edge to determine the gas temperature jump across the edge. There is enough statistical accuracy to divide the low-brightness region outside the edge into two bins, and the inner brighter region into three bins, avoiding getting to close to the cluster cool elongated core. Ticks inside the sector in Fig. 5.1 mark the five radial bins; the best–fit position of the density jump is indicated by the longer red ticks. The first high-brightness region adjacent to the jump extends across the best-fit jump position a bit, in order to avoid contaminating the adjacent low-brightness region by any irregularities in the edge shape. The spectra were fit in the 0.8–9 keV band with
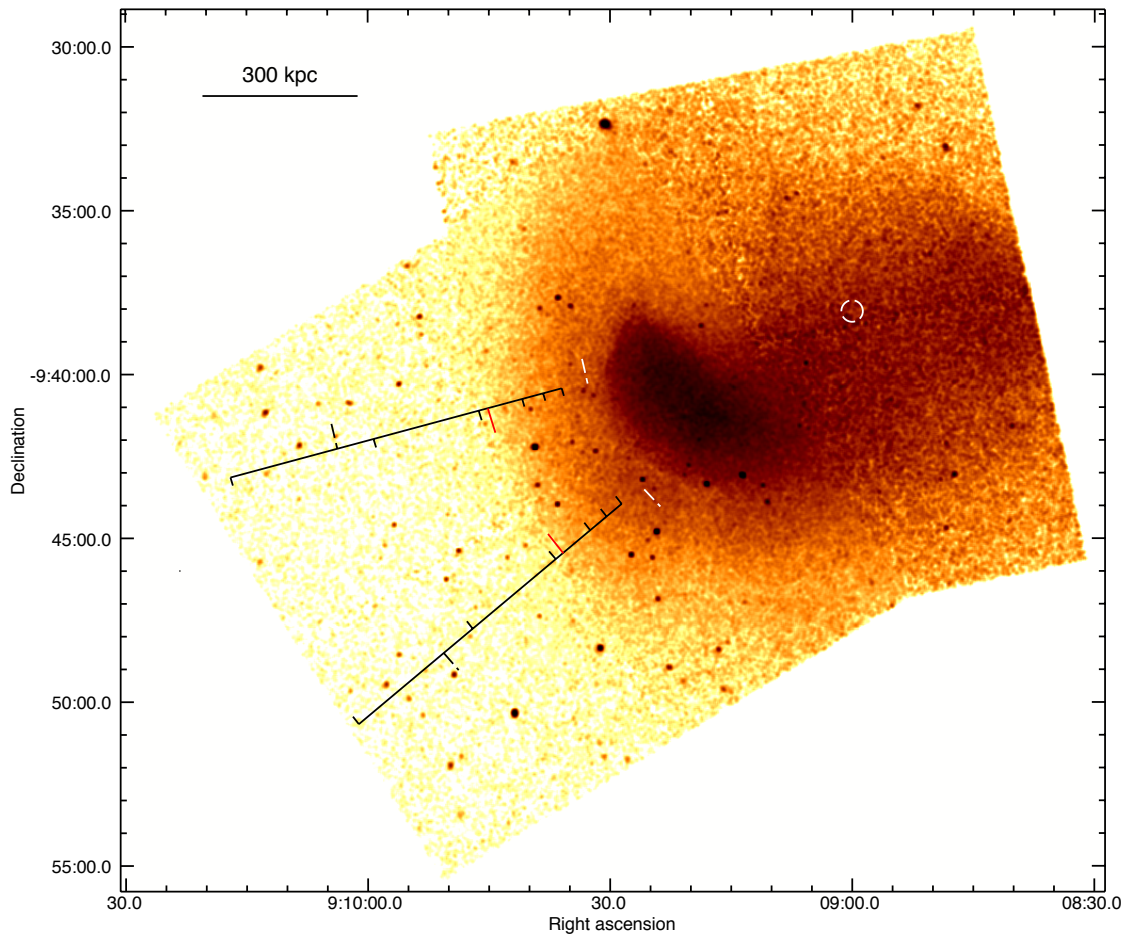
Figure 5.1: *Chandra* slightly smoothed 0.5–4 keV image of A754 from a sum of the new 95 ks exposure and the archival 39 ks observation. Also shown is the $25°$ sector used to extract the X-ray surface brightness profile and for the spectral analysis (see Sect. 5.3.1 and Sect. 5.3.2). Dashed ticks outside the sector mark the radial range used for the profile fitting; small ticks inside the sector mark the radial bins chosen to derive the temperature profile; bigger red ticks indicate the best–fit density jump, measured from its center of curvature (marked by the dashed circle).

Table 5.1: X-ray temperature fits

Region	obsid 577	obsid 10743	Simult. fit	χ^2/ d.o.f. [*]
Current (N0005) ACIS contaminant model:				
1	$17.6^{+6.6}_{-4.4}$	$9.0^{+1.0}_{-0.7}$	$10.1^{+1.0}_{-0.9}$	60.6/76
2	$9.6^{+2.2}_{-1.7}$	$14.2^{+2.5}_{-2.1}$	$12.5^{+1.9}_{-1.8}$	86.7/58
3	$8.7^{+2.2}_{-1.5}$	$16.4^{+3.7}_{-2.8}$	$13.3^{+2.5}_{-1.9}$	79.6/76
4	...	$7.4^{+2.3}_{-2.0}$	...	60.9/78
5	...	$4.5^{+2.4}_{-1.5}$	...	17.4/26
3 deproj ..	...	...	$16.4^{+5.1}_{-3.5}$	79.4/76
Experimental ACIS contaminant model:				
3	$8.7^{+2.2}_{-1.5}$	$14.2^{+2.8}_{-2.4}$	$12.2^{+2.1}_{-1.8}$	74.5/76
4	...	$6.6^{+2.3}_{-1.5}$	...	61.6/78

Notes to Table 5.1: [*] For post-shock regions 1, 2, 3, the χ^2/ d.o.f. (degrees of freedom) values refer to the simultaneous fits.

XSPEC, using the absorbed thermal plasma model WABS(APEC), with elemental abundances as free parameters, fixing the absorption column to the Galactic value ($N_H = 4.82 \times 10^{20}$ cm^{-2}, Kalberla et al. 2005). We also tried to free N_H, and all fits were consistent with the Galactic value. All fits had acceptable χ^2 values (see Table 5.1). The systematic uncertainty of background modeling was evaluated by varying the blank-sky background normalization by $\pm 2\%$ (68%, Hickox & Markevitch 2006) and added in quadrature to the statistical uncertainties. It was negligible for the brighter regions inside the edge, but similar to the statistical uncertainty for the two low-brightness bins (the observation exposure was selected to achieve this).

Solid crosses in Fig. 5.3 show the resulting temperature values, using the simultaneous fit to both observations for the inner regions and OBSID 10743 for the outer regions. The figure shows a clear temperature jump of the sign that corresponds to a shock front.

Table 5.1 gives separate fits for two pointings; the regions are numbered in order of increasing radius in Fig. 5.3. We note that two *Chandra* observations are in mild disagreement for the post-shock regions (though none deviates by more than 2σ from the simultaneous fit). This may be caused by residual calibration problems — these regions are at the edge of the ACIS-I field of view in OBSID 577, while at the center in OBSID 10743. In addition, these observations are separated by 10 years. We tried an experimental update to the recently released time dependence of the
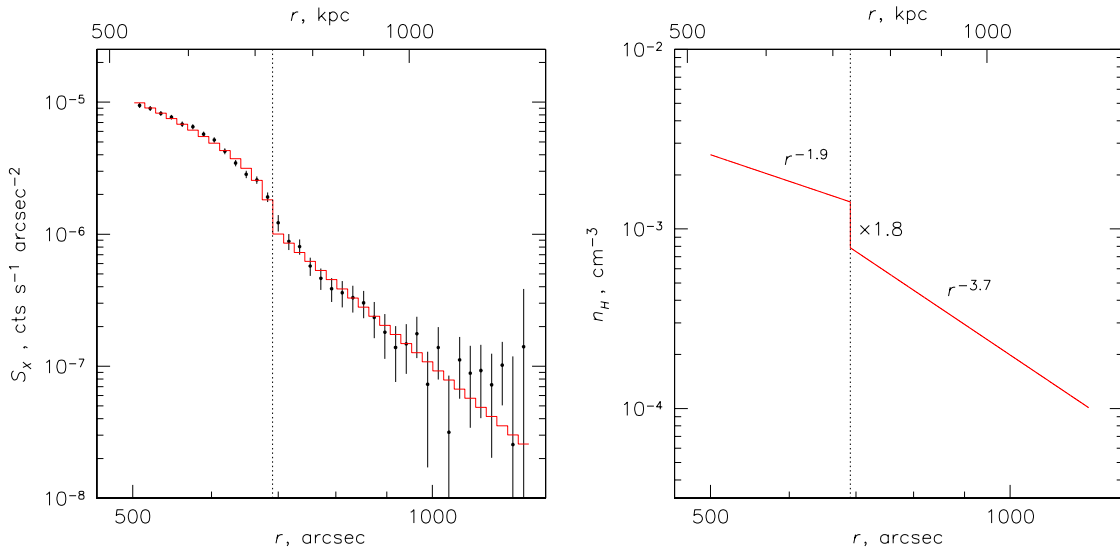
Figure 5.2: (*a*) The 0.5-4 keV surface brightness profile across the front in the sector shown in Fig. 5.1 (see text). Errors are 1σ; histogram shows the best-fit model that corresponds to the radial density profile shown in panel (*b*). The dashed line marks the best-fit position of the shock front (measured from its center of curvature).

time-dependent ACIS-I contaminant model (A. Vikhlinin, private communication) to see if it changes the results qualitatively, for the two bins adjacent to the front. The results are shown in Table 5.1. The disagreement is slightly reduced. Most importantly, the temperature jump does not change qualitatively, and is also seen in the recent observation alone, using either calibration. To the extent the results from different spatial regions can be compared, our post-shock high temperatures are in broad agreement with those derived with *XMM* by Henry et al. (2004).

Thus, the temperature profile confirms that the brightness edge is a shock front. From the Rankine-Hugoniot jump conditions, we can use our best-fit gas density jump to derive a Mach number of this shock. Assuming monoatomic gas with $\gamma = 5/3$, we obtain $M = 1.57^{+0.16}_{-0.12}$

The temperature jump can give an independent Mach number estimate, though usually with a lower accuracy. To check for the consistency of these estimates, we first get a deprojected temperature in the first post-shock radial bin, since in the spherical geometry, the temperature we measure there is affected by projection of the cooler emission from the outer, pre-shock bins. (At the same time, the pre-shock temperature profile appears consistent with isothermal, so the true temperature should be close to the projected one, to a sufficient accuracy). From the best-fit
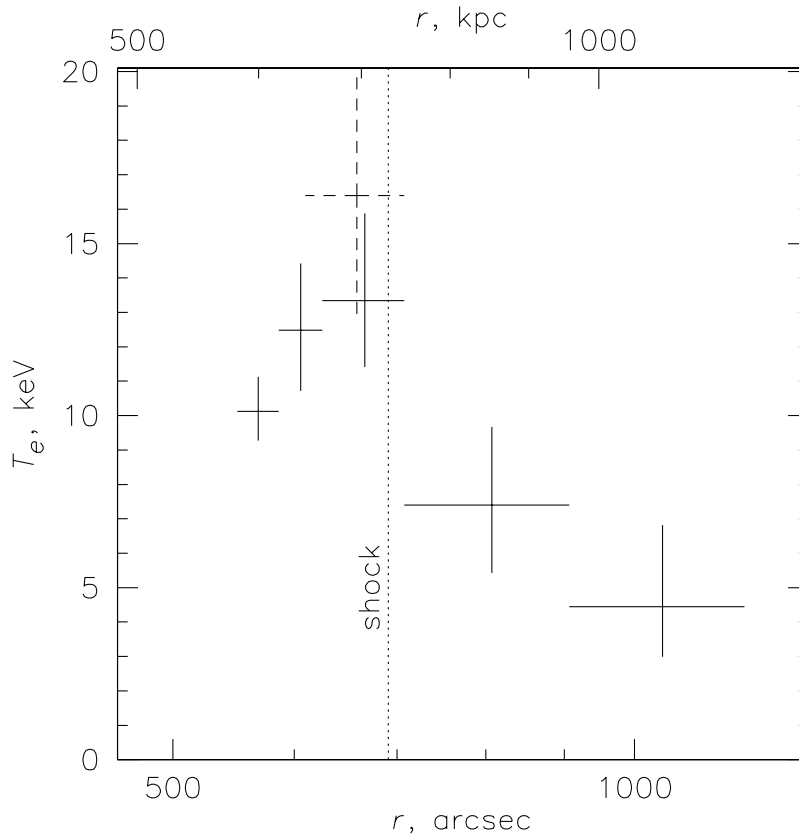
Figure 5.3: Temperature profile across the shock (errors are 68%). Solid crosses show projected temperature fits; dashed line for the first post-shock region shows a deprojected temperature (modeling the projected contribution of the pre-shock gas based on the best-fit density model). For post-shock regions, simultaneous fits for two observations are shown, while two outer regions are covered only by the recent observation (see Table 5.1 for more details). Dotted vertical line shows the position of the shock front from the density fit (see Fig. 5.2).

density model, we estimate a projected emission measure fraction in bin 3 from the outer regions 4 and 5 in Fig. 5.3 to be 21% and 3%, respectively. Neglecting the latter and fitting the spectrum for region 3 using an additional thermal model with the normalization and temperature (including its uncertainties) corresponding to region 4, we obtain a "deprojected" temperature shown by the dashed cross in Fig. 5.3.

The ratio of the post-shock to pre-shock temperatures is thus $2.2^{+1.1}_{-0.7}$, which corresponds to $M = 2.1^{+0.7}_{-0.6}$ (68%), consistent (within its expected larger uncertainties) with the value from the density jump obtained above.

5.4 Radio observations

In this section, we present our GMRT observations of A754 at 330 MHz, and analysis of the archival VLA data at 1.4 GHz. Details of observations are summarized in Table 5.2, which reports the telescope, project code, observing date, frequency, total bandwidth, total time on source, synthesized half-power bandwidth (HPBW) of the full array, rms level (1σ) at full resolution, $u - v$ range, and the largest detectable structure (LDS).

Table 5.2: Summary of the radio observations.

Radio telescope	Project code	Observation date	ν (MHz)	$\Delta\nu$ (MHz)	t (min)	HPBW, p.a. (full array, $''\times''$, °)	rms (μJy beam^{-1})	u-v range (kλ)	LDS (′)
GMRT	08GBA01	June 23, 2005	325	32(16)*	150	10.0×9.1, -64	450	~ 0.08–25	~ 32
VLA-D	AF372	Sept. 25, 2000	1365/1435**	50	160	64.5×38.8, 5	50	~ 0.13–4.7	~ 15

Notes to Table 5.2: * Only the USB dataset was used for the analysis (see Sect. 5.4.1). ** Only the the lower frequency IF was used for the analysis (see Sect. 5.4.2).

5.4.1 GMRT observations at 325 MHz

A754 was observed with GMRT at 325 MHz in June 2005 for a total time on source of 2.5 hr (Table 5.2). The observations were carried out using the upper and lower side bands simultaneously (USB and LSB, respectively), for a total observing bandwidth of 32 MHz. The default spectral-line observing mode was used, with 128 channels for each band and a spectral resolution of 125 kHz/channel. The LSB dataset was corrupted and could not be processed, so only the USB data, which are centered at approximately 330 MHz, were used to produce the images presented here. The dataset was calibrated and analyzed using the NRAO Astronomical Image Processing System package (AIPS).

Due to the large field of view of GMRT at 330 MHz (primary beam $\sim 1.8°$), we used the wide-field imaging technique at each step of the phase self-calibration process, to account for the non-planar nature of the sky. We covered a field of $\sim 2.7° \times 2.7°$ with 25 facets. The final images were produced using the multi-scale CLEAN implemented in the AIPS task IMAGR, which results in better imaging of extended sources compared to the traditional CLEAN (e.g., Clarke & Ensslin 2006; for a detailed discussion, see Appendix A in Greisen, Spekkens, & van

Moorsel 2009). We used three circular Gaussians as model components. One of the Gaussian was chosen to have zero width to accurately model point sources and small-scale structures, and the other two have a width of $20''$ and $45''$ respectively, to progressively highlight the extended emission during the clean.

Beyond the image at full resolution ($10.0'' \times 9.1''$), we produced images with lower resolution (down to $\sim 100''$), tapering the $u - v$ data by means of the parameters `robust` and `uvtaper` in the task IMAGR. Even though only half of the data was usable, the sensitivity of the final images is quite good — the rms noise level (1σ) ranges from 0.45 mJy beam^{-1} in the full resolution image to $\sim$1 mJy beam^{-1} in the lowest resolution images. We estimate that the flux density calibration uncertainties are within 5%.

5.4.2 VLA archive data at 1.4 GHz

VLA observations of A754 at 1.4 GHz (project AF372) were presented by B03. We extracted these observations from the archive and re-analyzed them in order to ensure the best possible comparison with our GMRT data. The observations were obtained using the D configuration and two IFs, centered at 1365 MHz and 1435 MHz (see Table 5.2 for details on the observations). Standard calibration and imaging were carried out using AIPS. The dataset was self-calibrated in phase only. The higher frequency IF was found to be affected by strong radio interference, which compromises the quality of the images produced using both IFs. For this reason, only the low-frequency IF was used for the analysis presented here. The final images were obtained implementing the multi-scale clean option in IMAGR, as for the 330 MHz data (see Sect. 5.4.1).
The rms noise in the image at full resolution is 50 μJy beam^{-1} (Table 5.2). A slightly higher noise ($1\sigma \sim 60 - 70$ μJy beam^{-1} was achieved in the low-resolution (HPBW$\sim$70$''$) images. The average residual amplitude errors in the data are of the order of 5%.

5.5 The cluster field at 330 MHz

A high resolution ($15'' \times 8''$) GMRT image at 330 MHz of the central field containing A 754 is presented in Fig. 5.4. The area shown is $\sim 45' \times 45'$ ($\sim 2.8 \times 2.8$ Mpc). Three radio galaxies with spectacular extended morphology are marked by the boxes. In

Fig. 5.5 the contours of the radio emission of these galaxies at 330 MHz are overlaid to the optical DSS-2 frame. The galaxies in the first two panels have bent radio jets and a typical narrow-angle tail structure, while the one on the right panel is a head-tail radio galaxy. All these tailed galaxies are located within the cluster virial radius (~ 3 Mpc), tracing the high dynamical activity of this merging system.
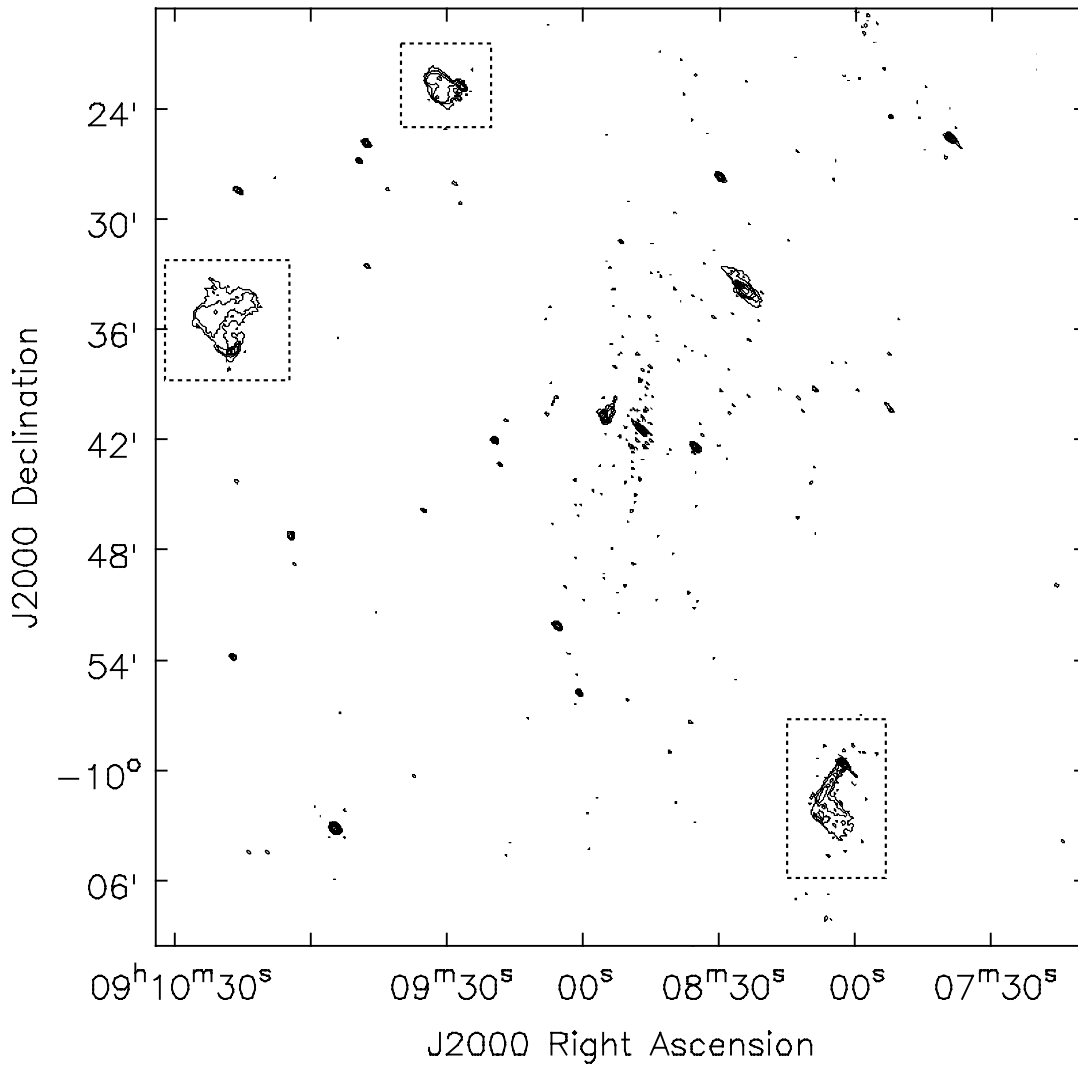

Figure 5.4: GMRT 330 MHz contours of the central $\sim 45' \times 45'$ field around A 754. The resolution is $15'' \times 8''$. Contours are spaced by 2, starting from $\pm 5\sigma = 2$ mJy/b.
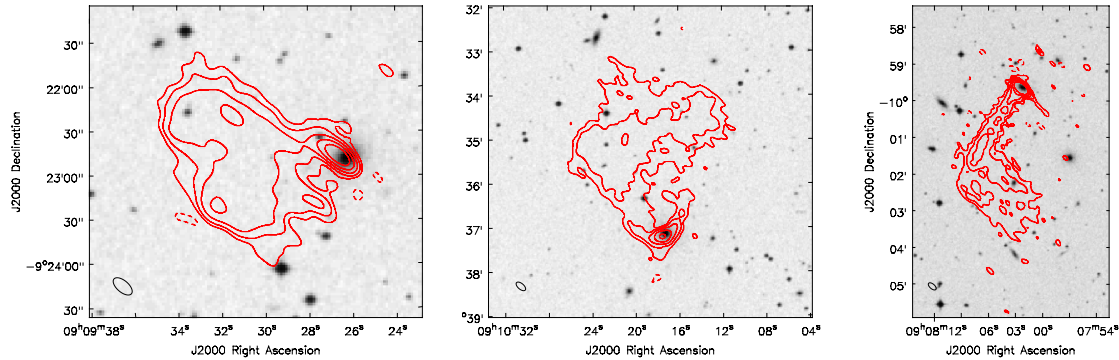
Figure 5.5: GMRT 330 MHz contours of the three tailed radio galaxies in the A 754 field. The resolution is $15'' \times 8''$. Contours are spaced by 2, starting from $\pm 5\sigma = 2$ mJy/b.

5.6 Radio analysis of the diffuse emission

5.6.1 The images

In Fig. 5.6, we present the new [1] GMRT image at 330 MHz at the resolution of $63'' \times 52''$ (upper panel) and the VLA 1365 MHz image at full resolution (HPBW$=64'' \times 39''$), overlaid on the optical POSS-2 red frame of A 754 (lower panel). The first positive contour corresponds to the 3σ level in both images (i.e., 3.3 mJy beam^{-1} at 330 MHz and 0.21 mJy beam^{-1} at 1365 MHz). Several discrete radio sources are located in the cluster area. Some of these sources are embedded within the diffuse emission. We identify all the radio galaxies found by B03. Following their same notation, these are labelled from S1 to S8 in both images. The point source S5 is undetected at 330 MHz.

In order to properly image the cluster diffuse emission, we subtracted all the discrete radio galaxies in the cluster region from the $u - v$ data at both frequencies. We first subtracted the brightest radio sources in the field (including the extended radio galaxy north–east of S1 in Fig. 5.6), to simplify the detection and subtraction of the fainter discrete galaxies embedded in the diffuse emission (from S1 to S8). We finally produced a set of low-resolution images from the "subtracted" data sets at both frequencies, to highlight the extended emission only.

Our results are shown in Fig. 5.7. The upper panel shows contours of our VLA low-resolution image at 1365 MHz (HPBW$=70'' \times 70''$), before the subtraction of

---

[1]These observations, available from the GMRT public archive, has been also recently used by Kale et al. 2009, for their low frequency study of A 754. However, they do not show the radio images obtained from these data.
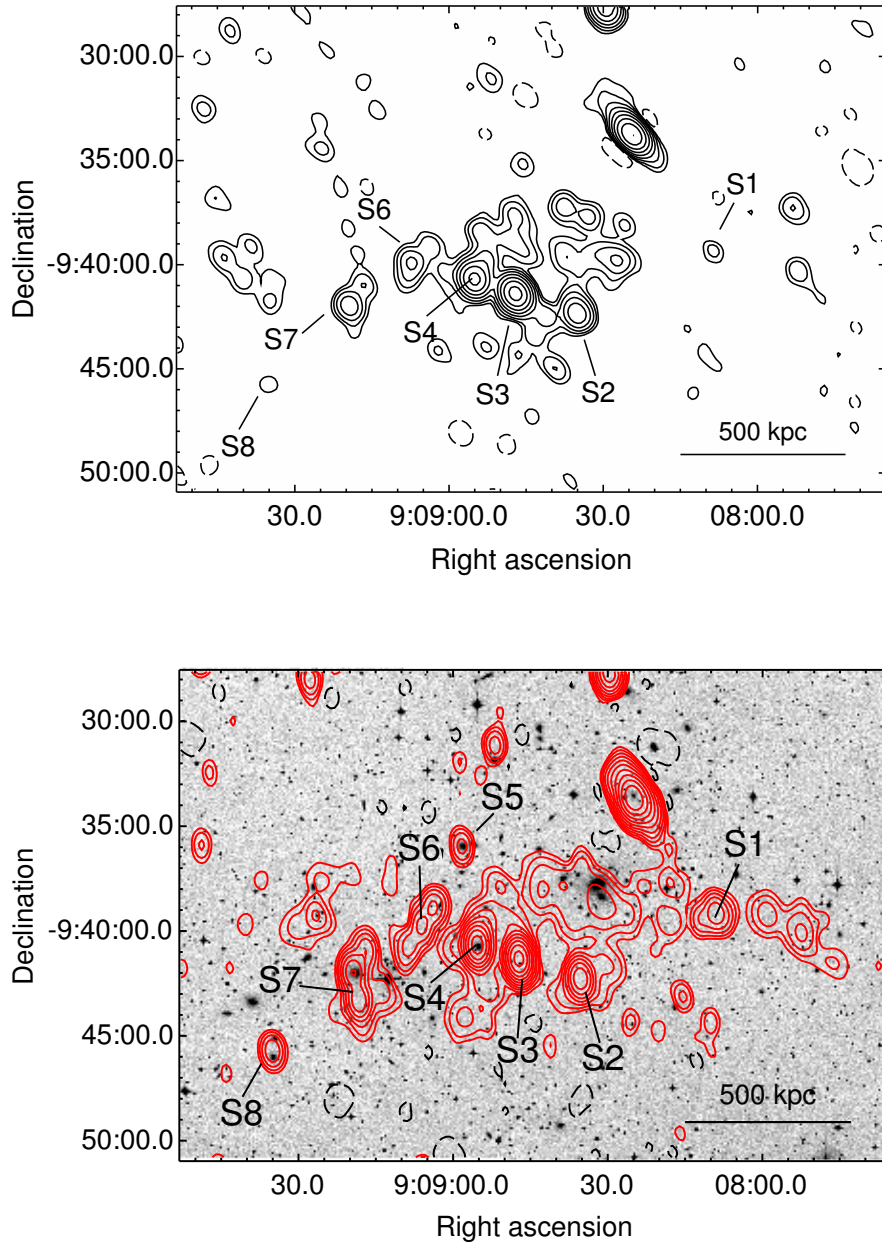
Figure 5.6: *Upper panel*: GMRT 330 MHz image of A 754 at the resolution of $63.5'' \times 52.1''$, p.a. $30°$. The 1σ level is 1.1 mJy beam^{-1}. Contours start at -3.3 mJy beam^{-1} (dashed) and $+3.3$ mJy beam^{-1}, and then scale by a factor of 2.
Lower panel: VLA full-resolution image at 1365 MHz (contours), overlaid on the optical POSS-2 red image of A 754. The restoring beam is $64.5'' \times 38.8''$, p.a. $5°$, and the 1σ noise level is 50 μJy beam^{-1}. Contours are spaced by a factor of 2, starting from ± 0.15 mJy beam^{-1} (negative contours are shown as dashed). In both images, labels indicate the discrete radio galaxies identified at 1.4 GHz by B03.
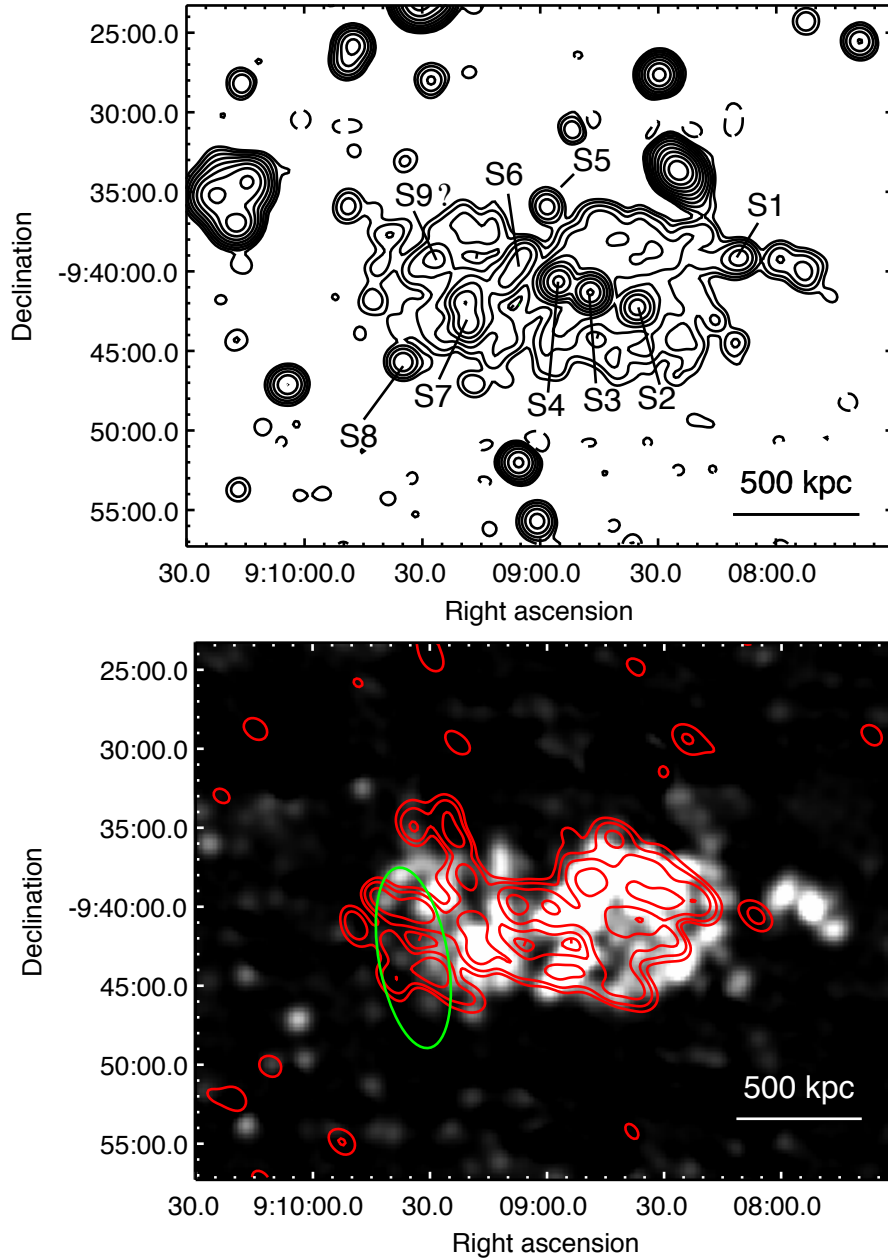
Figure 5.7: *Upper panel*: VLA low-resolution image at 1365 MHz. The restoring beam is $70'' \times 70''$, p.a. 0; contours are spaced by a factor 2 starting from $\pm 3\sigma$, the 1σ level is $60~\mu$Jy beam^{-1}. Labels indicate the discrete radio galaxies identified within the diffuse emission. Negative contours are shown as dashed. Ticks mark contours that correspond to holes in the radio brightness.

Lower panel: diffuse emission after the subtraction of all identifiable discrete sources. Red contours show a low-resolution GMRT image at 330 MHz with a restoring beam of $109'' \times 74''$, p.a. $43°$ and the 1σ noise level of 1 mJy beam^{-1}. Contours are spaced by a factor of 2, starting from 3σ. Greyscale shows a low-resolution VLA image at 1365 MHz — same as in left panel but without the discrete sources. The peak flux density is 3.77 mJy beam^{-1} and the lowest level of greyscale corresponds to $\sim 2\sigma$. The green ellipse is the area covered by the 2σ contour (0.4 Jy beam^{-1}) of the radio relic in the VLA image at 74 MHz (K01). Ticks mark contours that correspond to holes in the radio brightness.

discrete radio sources [2]. The rms noise of the image is 60 μJy beam^{-1} (1 σ); this is significantly lower with respect to the noise level reached by B03 in their image of same resolution (see Fig. 3 of B03). In the lower panel of Fig. 5.7 we present images of the diffuse emission only, obtained after the subtraction of discrete sources as described above. The GMRT 330 MHz intensity contours at the resolution of $109'' \times 74''$ are overlaid on the VLA 1365 MHz image (grayscale), produced with a restoring beam of $70'' \times 70''$. Both images show the very large extent and complexity of the diffuse emission in A754. The diffuse source spans ~ 1.4 Mpc in the east-west direction and ~ 750 kpc along the north-south axis, as measured from the 3σ contour level at 330 MHz. The 1365 MHz image reveal a ridge in the radio brightness, extended westbound the 330 MHz contours. On the other hand, the high frequency emission is less extended in the eastern region (see below). We point out that these are reliable features, not due to a shift between the two images. Indeed we carefully checked the astrometry of our radio images at both frequencies, by comparing the positions of the peaks of the radio sources with that of the optical counterparts.

The green ellipse in Fig. 5.7 (lower panel) represents the 2σ contour (0.4 Jy beam^{-1}) of the eastern radio relic found in the 74 MHz VLA image by K01. The 330 MHz diffuse emission extends eastward to the outer side of this relic. Interestingly, we notice that the shock front found in Sect. 5.3.2 coincides with the edge of the emission at 330 MHz (see Fig. 5.8), possibly suggesting a connection between the radio edge and the shock (see Sect. 5.7). We note that this is only the second cluster in which a clear coincidence between a shock and a diffuse radio edge has been reported so far (the other being A 520, Markevitch et al. 2005).
We detect significant emission at 1365 MHz only in part of the region covered by the green ellipse (see Fig. 5.7). Our VLA images at 1365 MHz show more diffuse emission, south of the S2-S4 sources, with respect to B03. This is most likely due to differences in the editing of the data, in the imaging procedure (multi-scale clean, see Sect. 5.4.2) and in the accuracy of the subtraction of discrete sources (see also the comment in B03); our final rms value is indeed a factor 1.6 better.
We do not detect any radio emission in the region of the western relic found by K01.

---

[2] Here S9 ? indicate the peak of emission visible to the north–east of S7 in Fig. 5.6. This apparently coincides with an optical counterpart, and might be an additional point source; however we considered it as a peak of the diffuse emission and we did not subtract it from the data.
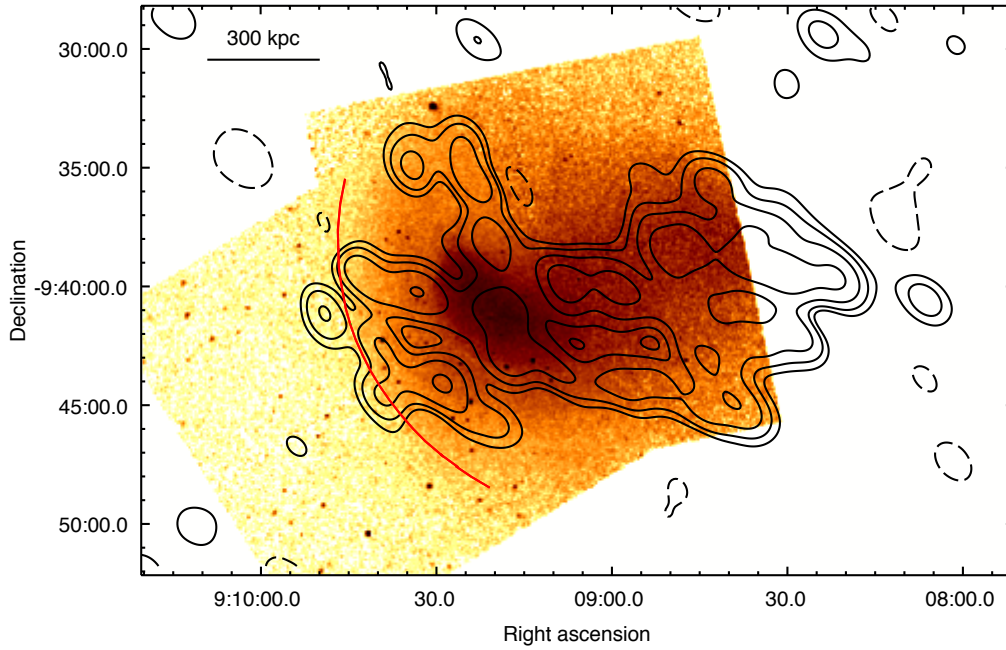
Figure 5.8: GMRT low resolution radio contours (same as in Fig. 5.7, lower panel), overlaid on the *Chandra* image of A754 (same as Fig. 5.1, see Sect. 5.3). The dashed contours show the 3σ negative values; the red arc indicates the best fit position of the density jump (see Sect. 5.3.1).

5.6.2 The spectrum

The radio images in Fig. 5.7 (lower panel) show a complex, Mpc-scale diffuse source associated with A754. We use our 330 MHz GMRT and the reprocessed 1365 MHz VLA data presented in Sect. refsec:radioobs, along with the VLA image at 74 MHz kindly provided by N. Kassim (see Fig. 1 in K01), to derive its integrated spectrum. The flux densities of the diffuse emission, after the subtraction of the discrete sources, are 828±41 mJy and 89±5 mJy at 330 MHz and 1365 MHz, respectively. These are also reported in Table 5.3, along with the associated uncertainties and angular resolution of the images used for the measurements. We obtained these values by integrating over the same area that encompasses the whole diffuse emission as detected at both frequencies [3]. We note that the flux density at 1365 MHz is lower than the value reported in B03 where, however, the authors notice that the subtraction of discrete sources is not accurate (B03; see also Sect. 5.6.1). The flux density of the whole diffuse emission at 74 MHz is ~ 6.6 Jy (Tab. 5.3). This value was integrated over the same area described above and does not include the

---

[3]We also checked that no significant change in the spectral index occurs by integrating within the emission at the 2σ level.

contribution of the brightest radio galaxies at the cluster center (i.e., S2, S3 and S4, and the extended radio galaxy north–east of S1; see Fig. 5.6) which amounts to a total of ~ 2.9 Jy (as estimated in K01). However, due to the lower sensitivity, only part of the extended emission visible at 330 MHz and 1365 MHz is detected at 74 MHz. Thus, our estimate should be considered as a lower limit to the flux. The spectral index for the whole diffuse emission between 330 and 1365 MHz is $\alpha = 1.57 \pm 0.05$. This value is steeper than typically found for giant radio halos ($\alpha \sim 1.2 - 1.3$; e.g., Ferrari et al. 2008), although a number of halos with ultra-steep spectrum ($\alpha > 1.5$) has been discovered in the past few years (*e.g.* Brunetti et al. 2008; Brentjens 2008; Macario et al. 2010; see also Chap. 3).

For simplicity, in the following we will call *relic* the feature discovered by K01 at 74 MHz, that they defined as eastern radio relic (see also discussion, Sect. 5.7). In our GMRT image at 330 MHz, the relic does not appear as a distinct feature separated from the radio halo, nor a clear increment of the surface brightness of the diffuse emission is detected in that region. This may imply that the spatial segregation between the relic and the halo in the 74 MHz image (see Fig. 1 in K01) may be due to a steeper spectrum of the relic at $\nu \lesssim 300$ MHz combined with the lower sensitivity of the 74 MHz observation.

To obtain the radio spectrum of the relic region, we integrated the flux densities at 330 MHz and 1365 MHz over the area defined by the 2σ contour level of the relic at 74 MHz (green ellipse in Fig. 5.7, lower panel). We obtained 106±5 mJy at 330 MHz and 6.0±0.3 mJy at 1365 MHz (see Table 5.3).

In Fig. 5.9 we show the integrated radio spectrum of the relic, in the frequency range 74–1365 MHz. The relic has indeed a very steep spectrum, with $\alpha_{0.07GHz}^{0.3GHz} = 1.77 \pm 0.10$, and $\alpha_{0.3GHz}^{1.4GHz} = 2.02 \pm 0.04$. An extrapolation of this power law to lower frequencies predicts a 74 MHz flux density that is consistent with that reported in K01. For a direct comparison, the flux densities of the whole diffuse emission are also shown.

A spectral study of the diffuse emission in A 754 was presented in Kale et al. (2009). However their analysis is limited to specific regions of emission detected in their GMRT 150 MHz image (that do not show the whole extended emission). Therefore, we cannot compare our spectral results to those found by them.

Table 5.3: Flux densities of the diffuse radio emission in A 754

ν (MHz)	HPBW , $'' \times ''$	S_ν (mJy)		Ref.
		relic	*whole emission*	
74	316×232	1489 ± 223	~6600	this work; K01
330	109×74	106 ± 5	828 ± 41	this work; Fig. 5.7
1365	70.0×70.0	6.0 ± 0.3	89 ± 5	this work; Fig. 5.7
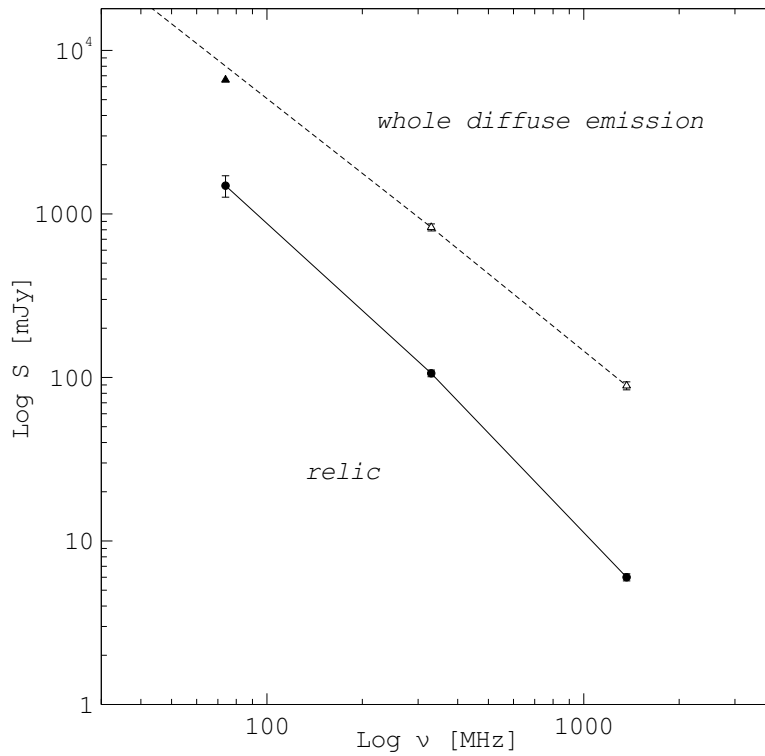
Figure 5.9: Integrated spectrum of relic region (filled dots) in A 754 in the frequency range 74–1365 MHz. The solid line connects the values of flux density reported in Table 5.3. The spectrum of the whole diffuse emission between 330 and 1365 MHz is also shown (open triangles and dashed line); the estimated flux density at 74 MHz (filled triangle) is in reasonable agreement with the extrapolation of the spectrum.

5.7 Discussion

The main result of the study presented here is the clear X-ray detection of a shock front in the intracluster gas of A 754, which coincides with the edge of non-thermal radio diffuse emission at 325 MHz.

Particle acceleration at the shock front cannot be responsible for the whole Mpc-

scale diffuse emission seen in Fig. 5.7. Given the shock parameters derived in Sect. 5.3.2, the downstream velocity of the gas is $\simeq 1100$ km s^{-1}, which implies that the size of the diffuse emission produced by the shock can be only $\sim 100 - 200$ kpc, once the radiative lifetime of the emitting electrons $(1 - 2 \times 10^8$ yr) is taken into account (see also the discussion in Markevitch et al. 2005 and Brunetti et al. 2008). However, the spatial coincidence of the ultra-steep spectrum radio edge with the shock front suggests a physical connection between these two features, and possibly an indirect connection between the shock and the diffuse emission on the larger scale. If one assumes that relativistic electrons in the relic region are accelerated via Fermi mechanism by the shock front with $M \sim 1.6$ (as observed in X-rays, see Sect. 5.3.2), the expected slope of the radio spectrum from that region, accounting for the downstream losses, is $\alpha \sim 2.3$ ($\alpha = \alpha_{inj} + 1/2$, where $\alpha_{inj} = (p - 1)/2$ and $p = 2[(M^2 + 1)/(M^2 - 1)]$; e.g., Blandford & Eichler 1987), in rough agreement with the radio observation (see Sect. 5.6.2). However, we can rule out direct shock acceleration on energy grounds. If we extrapolate the power law spectrum of electrons responsible for the relic emission down to thermal energies (as we should if the seed electrons are thermal), the energy in relativistic electrons will be of the same order as the thermal energy in the ICM requiring an implausibly high acceleration efficiency. This energy argument implies that observable radio emission cannot be produced at shocks with $M < 2$ (Hoeft & Brüggen 2007).

Below we discuss possible scenarios for the origin of the cluster-scale diffuse emission in A754.

1. The edge emission might arise from relativistic plasma that is re-energized at the shock. If fossil electrons are present in the ICM, compression by the shock can significantly increase their synchrotron emission at the observing frequency (e.g., Ensslin et al. 1998, Ensslin & Gopal-Krishna 2001, Markevitch et al. 2005). Adiabatic compression increases the maximum synchrotron frequency emitted by a population of fossil electrons by $r^{4/3}$ times (e.g., Markevitch et al. 2005), where r is the shock compression factor (considering a shock moving perpendicular to the line of sight). In our case, this implies only a moderate boosting of a factor 2. The resulting synchrotron emission may light up at our observing frequency. The drawback of this scenario is that in this case the fossil plasma must have been injected in the ICM only a few 10^8 yrs ago,

because the fossil electrons must exixt at energies just below those necessary to emit at the observed frequency, and at those energies the lifetime is short. This problem remains even if one assumes that the fossil plasma is confined (not mixed) by the ICM (Ensslin & Gopal-Krishna 2001), due to the low Mach number of the shock.

2. Shock re-acceleration of fossil relativistic plasma can potentially be an efficient process even in the case of weak shocks, though this process at weak shocks is poorly understood and its efficiency is uncertain. Assuming the standard linear shock acceleration theory (e.g., Blandford & Eichler 1987), the spectrum of re-accelerated electrons is:

$$N(\gamma) = (p+2)\gamma^{-p} \int_{\gamma_{min}}^{\gamma} N_{fss}(x)x^{p-1}dx \qquad (5.1)$$

where $p = 2[(M^2 + 1)/(M^2 - 1)]$ is the slope of the spectrum of accelerated electrons immediately after the shock, N_{fss} is the spectrum of fossil electrons in the upstream region, and γ_{min} is the minimum energy of the fossil electrons at which the re-acceleration process works. If the fossil relativistic electrons have an exponential cutoff in their power spectrum (as they should if they result from radiative cooling, e.g. Sarazin 2002), shock re-acceleration should create a spectrum above that cutoff with a slope similar to the one in the classical Fermi re-acceleration. Assuming $M \sim 1.6$, consistent with our findings in Sect. 5.3.1, a power-law tail of radio emission with $\alpha \sim 2.3$ can be generated at energies $\gamma > 1000$ (Figure 5.10). This scenario avoids the energy argument mentioned earlier, because the resulting steep spectrum of electrons does not extend down to the thermal energies.

3. The connection between the edge and the shock might be indirect. For instance, the passage of the shock may have driven small-scale turbulence in the ICM, which may be long-lived and also produce the radio halo on the larger scale. In this case, the radio edge would mark the region where turbulent acceleration is just beginning to occur. This should happen after $\sim$1 eddy turnover-time of the turbulence, $\approx L/V_l$ (where L and V_l are the maximum scale and velocity of the turbulent eddies), since the turbulent modes at smaller scales are the most important in the particle acceleration process (e.g., Brunetti & Lazarian 2007 and references therein). This may also explain the very steep spectrum of

the radio emission in the shock region. A possible indirect connection between shocks and the cluster-wide diffuse radio emission is suggested by the present radio observation, as well as those of several other clusters, where bridges of emission connecting radio relics and halos in several clusters are seen (see, for instance, the discussion in Brunetti et al. 2008; see also the recent review by Markevitch 2010). A theoretical exploration of this scenario deserves a future effort.
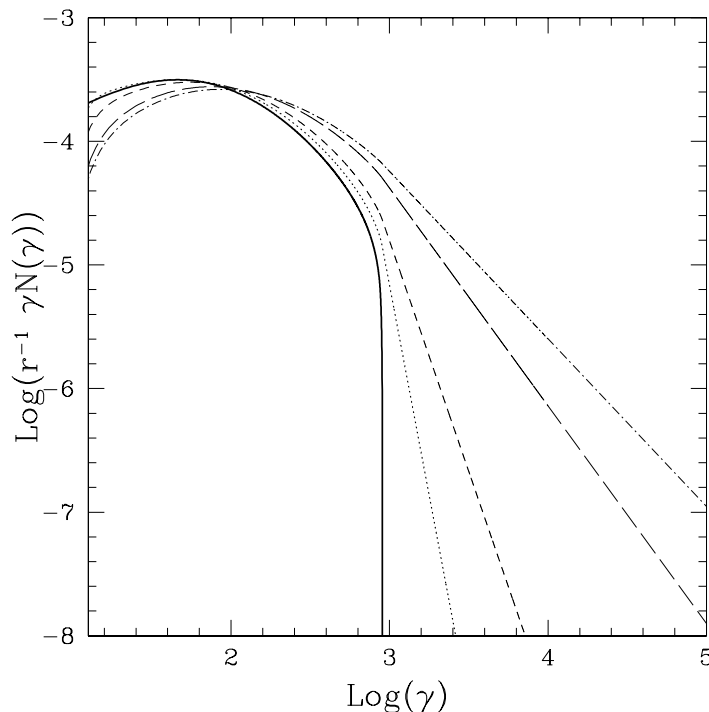
Figure 5.10: Spectrum of re-accelerated electrons according to Eq. 5.1 We also correct for the shock compression factor in the downstream region, r. The thick solid line is the initial spectrum of fossil electrons (assuming an age of the population of a few Gyrs and typical cluster physical parameters, e.g. Sarazin 2002). Different models show the spectrum for Mach numbers 1.3 (dotted line), 1.57 (dashed line), 2.5 (long–dashed line), and 3.5 (dot–dashed line). A minimum energy $\gamma_{min} = 10$ is adopted in the calculations.

5.8 Summary and conclusions

In this chapter, we have presented a combined X–ray and radio study of the nearby merging galaxy cluster Abell 754.

The new *Chandra* observation confirms the presence of a merger shock front east of the cluster core by providing the Mach number from the density jump across the

shock M= $1.57^{+0.16}_{-0.12}$, and a direct measurement of a gas temperature jump of the right sign across the arc-like brightness edge, $T_2/T_1 = 2.2^{+1.1}_{-0.7}$.

The new GMRT radio image of the cluster at 330 MHz reveals that the centrally located diffuse emission is very extended and complex, and is mainly elongated in the east-west direction. Most interestingly, the eastern edge of this source coincides with the shock. We studied the spectral properties of the diffuse radio emission, using the GMRT data, archival VLA data at 1.4 GHz, and previous VLA results at 74 MHz. We find that the region next to the radio edge (the *relic* region in K01) has a very steep integrated spectrum, with $\alpha^{1.4GHz}_{0.3GHz} = 2.02 \pm 0.04$ and $\alpha^{0.3GHz}_{0.07GHz} = 1.77 \pm 0.10$ This is steeper than the average spectrum of the whole diffuse emission, $\alpha^{1.4GHz}_{0.3GHz} = 1.57 \pm 0.05$, which is in itself steeper than the typical spectrum of radio halos.

The spatial coincidence of the steep spectrum radio edge and the merger shock front suggests a physical connection. The low Mach number of the shock and the very steep synchrotron spectrum of the edge allow us to rule out the scenario of direct shock acceleration of thermal particles for the origin of the edge, because it would require an implausibly high acceleration efficiency (of order 1).

Possible alternative scenarios are re-acceleration and/or adiabatic compression of fossil relativistic plasma in the ICM. Of these, shock re-acceleration is more plausible for this weak shock. It should produce a spectrum of electrons that is consistent with the observed steep radio spectrum of the relic region.

Finally, an indirect connection between the shock and the radio edge is also possible. The shock passage may drive small-scale turbulence that may re-accelerate electrons over the cluster volume.

A more detailed study of the diffuse emission over a wider frequency range will help to determine the most plausible scenario for its origin; scheduled deep GMRT low frequency observations (150, 235, 330 MHz) will allow us to address this point.

Chapter 6

Galaxy clusters with LOFAR: early results and future surveys

The Low Frequency Array (LOFAR) is the new generation radio telescope which will soon take over the current instruments in the study of diffuse radio sources in galaxy clusters, in particular with respect to the ultra steep spectrum emission. For this reason, it is crucial to master the data reduction procedures to best exploit the capabilities of this instrument.

LOFAR is now in the commissioning phase. The commissioning of the LOFAR imaging system has been ongoing since the first 3 working stations became available in the summer of 2009. From then on, the LOFAR collaboration started organizing the *Imaging Busy Weeks*, on regular basis. During these weeks, a team of people involved in the LOFAR project have been working on the first commissioning data, contributing to different tasks aimed to test both the instrument capabilities and the software developed for the imaging pipeline. As Ph.D. member of the LOFAR Survey Key Science Project (SKSP), during the the past 2 years I have participated in the busy weeks activities and I have been involved in the commissioning activities related to the clusters KSP working group.

After a brief introduction to the LOFAR telescope, in this Chapter I will summarize the main goals of the SKSP, with particular focus on the importance of survey observations of galaxy clusters. Then I will report early results obtained by the LOFAR imaging busy week team from commissioning observations of galaxy clusters.

6.1 An overview of the Low Frequency Array (LOFAR)

The Low Frequency Array (LOFAR; Falcke et al. 2007) is a unique radio telescope facility, that will observe the Universe between 10 and 240 MHz with unprecedented sensitivity and angular resolution. After some re-scoping from the original project, the array will consist of 24 *core* stations, located within the central 5 km area in the North-Eastern part of the Netherlands (near the village of Exloo), 16 *remote* stations out to 100 km within the Netherlands, and 8 *international* stations located in Germany (5), France, Sweden and the United Kingdom. Baseline lengths range from several meters in the inner core to 1500 km between international stations. The construction LOFAR is still underway. At the current stage, 32 stations are completed[1], and are routinely performing both single-station and interferometric commissioning observations: 20 in the core, 7 remote, and 5 international (3 in Germany, 1 in UK and 1 in France). An example of a LOFAR core station is shown in Fig. 6.1 (top panel). Each LOFAR station has a Low Band Antennas (LBA) and a High Band Antennas (HBA) field (see Fig. 6.1, bottom panels). The LBA fields are made up of 96 simple dual polarization dipoles that are combined as a phased array and are sensitive between 10 and 80 MHz (*i.e.,* before the FM band). The HBA fields are made up of either 48 (in remote stations) or 96 (in core stations) tiles of dual dipole antennas that form an aperture array system, which is sensitive between 110 and 240 MHz. For the core-stations, the HBA field is split into two sub-fields, whereas for the remote and international stations all of the HBA tiles are grouped together.

Unlike the usual parabolic dish radio telescopes, the LOFAR stations have no moving parts. Observations towards a particular target in the sky are obtained by coherently adding the signals of the incoming radiation in the direction of interest. This *beamforming* is carried out by computing and is highly flexible. For example, the LOFAR system has 248 sub-bands that can be used as a single beam with a total bandwidth of 48 MHz. Alternatively, the sub-bands can be used to form up to 248 different beams on the sky simultaneously, but with a smaller bandwidth per beam. The data from the individual stations are connected via optical fibres to the IBM BlueGene/P supercomputer in Groningen, where the correlated visibilities are produced (see

---

[1]The current status of the buildup of LOFAR stations can be seen as a Google Maps overlay at http://www.astron.nl/~heald/lofarStatusMap.html

e.g. de Vos et al. 2009 for more details).

LOFAR has many different scientific goals, and a number of Key Science Projects (KSP) have been designed to i) carry out deep extragalactic surveys, ii) probe the epoch of re-ionization, iii) study cosmic magnetism, iv) investigate the transient sky, v) study solar physics and vi) observe ultra high energy cosmic rays (see *e.g.* Rottgering et al. 2006). LOFAR will also provide an important testbed for the technologies (hardware and software) that will be used for the Square Kilometre Array.

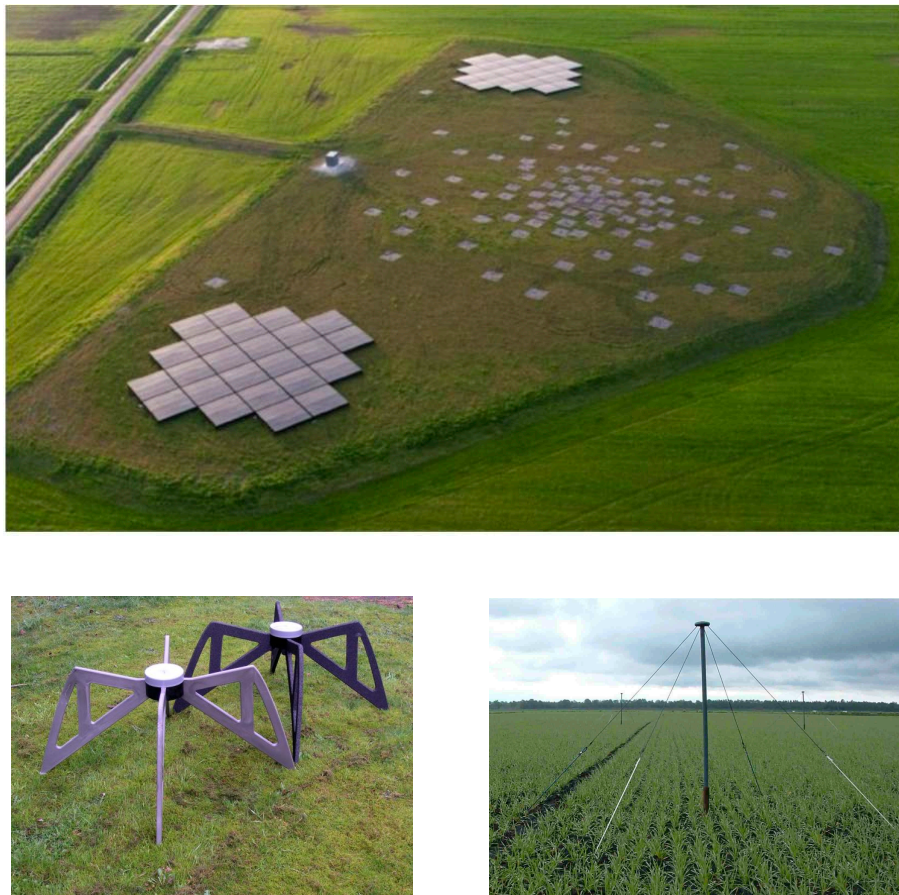Figure 6.1: *Top panel*: Example of a LOFAR core station, showing the 96 simple dipoles that are combined as an LBA phased array, the 48 tiles combined as an HBA aperture array (split into 224 tile sub-fields) and the electronics cabinet in the centre. From McKean et al. 2011 (submitted). *Bottom panels*: Pictures of HBA (left) and a LBA (right) dipole elements (from http://www.lofar.org/ image gallery).

6.2   The LOFAR cluster Survey Key Science Project

In this section we will describe only some aspects of the LOFAR Survey Key Science Project (SKSP), relevant to the scientific topic of this thesis.

The huge fractional bandwidth, the large collecting area and the possibility of multi-beam observations makes LOFAR an ideal survey facility. For example, at 50 MHz each beam has a 7.5 degrees field of view. With theoretical LOFAR sensitivities and feasible observing times, such a field will typically contain 1 high redshift radio galaxy ($z > 6$), 5 Abell clusters, 5 NGC galaxies, 5 lensed radio sources and several giant (> 1 Mpc) radio galaxies.

The SKSP is a big project aimed to observe large areas of the sky at a number of "key" frequencies. The SKSP is driven by four key scientific topics: (i) investigation of high-redshift galaxies; (ii) study of galaxy clusters; (iii) study of the cosmic star formation history; (iv) exploration of new parameter space for serendipitous discovery (see Rottgering 2010 for more details on each topic). To reach the goals of all these topics, the proposed surveys will be carried out at five frequencies, referred to as 15, 30, 60, 120, 150 and 200 MHz, and with a *three-tier* approach (see Table 1 and 2 in Rottgering 2010 for more details).

Compared to other radio surveys, the proposed LOFAR surveys will be unique both in terms of explored frequencies and of reached sensitivities. In Fig. 6.2, the flux density limits of a number of radio surveys in function of frequency are plotted together with the proposed surveys. It is clear that the proposed LOFAR surveys will be 2-3 orders of magnitudes deeper than any other existing large sky radio survey.

Among the above mentioned scientific topics, the study of galaxy clusters is one of the main science drivers of the SKSP. In particular some of the proposed surveys are very well designed for the study of diffuse radio emission in galaxy clusters. In this context, the observational and scientific goals of the Cluster SKSP are the following:

- **surveys of diffuse radio emission**: the LOFAR surveys at 120 MHz are expected to discover of $\sim$350 giant radio halos at redshift $z \leq 0.6 - 0.7$, most of them with very steep spectrum ($\alpha \geq 1.5$; Cassano et al. 2010a). This will
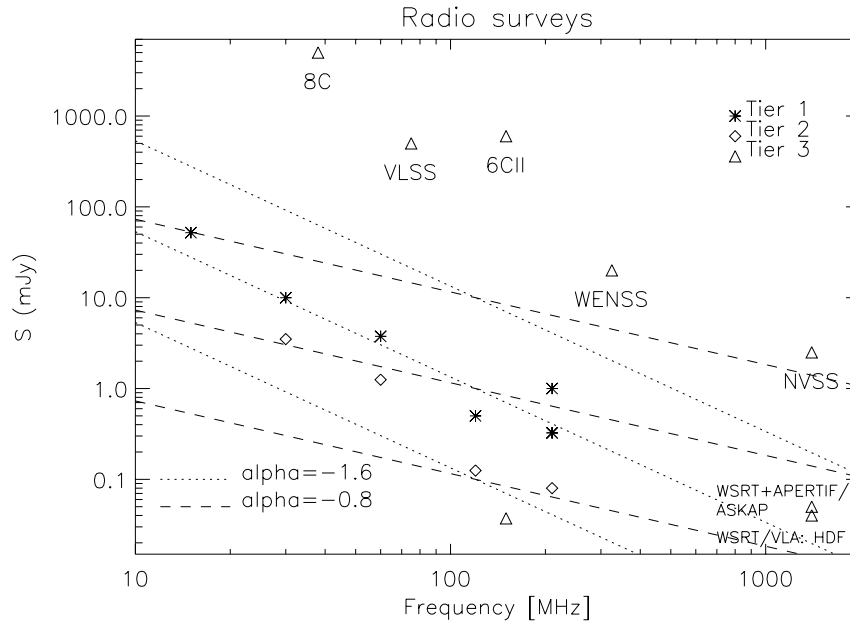
Figure 6.2: Flux density limits (5σ) of the proposed LOFAR surveys compared to other existing radio surveys. The lines represent different power-law ($S \propto \nu^{\alpha}$, with $\alpha = -1.6$ and -0.8) to illustrate how, depending on the spectral indices of the sources, the LOFAR surveys will compare to other surveys.

allow an improvement in our understanding of the statistical properties of giant radio halos and of their origin and evolution with cosmic time;

- **studying the merger–radio halo connection**: X–ray cluster catalogues in the northern hemisphere, such as NORAS and REXCESS (Böhringer et al. 2000, 2007) contain more than 600 galaxy clusters in the redshift range 0–0.6 with X-ray and optical information. The brightest of these clusters will be surveyed with unprecedented sensitivity and adequate spatial resolution by the LOFAR surveys, allowing us to address the connection between the formation of radio halos and cluster mergers with unprecedented statistics.

- **spectrum of radio halos**: the shape of the spectrum of radio halos is a fundamental observable to understand the mechanisms responsible for particle acceleration in the ICM (Sect. 1.9.1; *e.g.* Brunetti 2003). Present observations are limited in providing solid constraints due to the small frequency range (typically 330–1400 MHz) where halos can be studied today. LOFAR surveys will detect all the known radio halos in the northern hemisphere with unprecedented sensitivity and to measure accurately their flux densities in the

frequency range 15–200 MHz. This guarantees a fairly large frequency coverage and opens the possibility to firmly constrain the acceleration mechanisms of the relativistic matter.

- **spectral and polarization studies of radio relics**: although a connection between merger shocks and radio relics is fairly accepted, it is not yet clear wether the origin of relics is due to shock acceleration of thermal particles (Sect. 1.9.2; *e.g.* Enßlin et al. 1998) or to re-energization (via adiabatic compression) of ghost relativistic plasma due to the shock passage (Sect. 1.9.2; *e.g.* Enßlin & Gopal-Krishna 2001). These models have different expectations in terms of synchrotron spectral shape and polarization, that will be properly tested by sensitive observations down to the LOFAR frequencies.

These goals will be achieved by the proposed survey observation, in particular:

- The *tier 1* observations will survey of the northern hemisphere at 15, 30, 60, 120, 200 MHz. The depth and large area of the planned 120 MHz survey are designed to detect the diffuse synchrotron emission in galaxy clusters from both radio halos and relics, up to a redshift z$\sim$1.
  Based on present models and on the survey sensitivities, detection of radio halos and relics is expected in more than 500 clusters (up to $z = 1$) at 120 MHz (rms 0.1 mJy). The 200 MHz survey will be shallow (rms 0.2 mJy) and thus it will be followed by a deeper survey at the same frequency (rms 0.065 mJy; Fig. 6.2), with adequate spatial resolution, pointed on 60 X-ray luminous clusters that host diffuse emission. These surveys are expected to address most of the above mentioned goals.

- In the deeper *tier 2* surveys, a few nearby clusters with diffuse emission will be observed at 30, 60, 120, and 200 MHz. These observation will allow to study the spectral and polarization properties of these sources with unprecedented detail.

6.3   The LOFAR imaging pipeline

The huge data volume of a typical LOFAR observation (*e.g.* 15 TB for 6 hour dataset with 25 stations and 1 s integration time), and the planned LOFAR coverage of the

northern sky (Sect. 6.2) together require that most imaging processing is done offline in an automated process, such that fully calibrated images are produced by the system during survey operations. To this purpose, the LOFAR Imaging Pipeline[2] is being developed.

The Imaging Pipeline is shown schematically in Figure 6.3. Following the data path from the left, visibility data are stored in Measurement Sets at the IBM Blue Gene/P correlator in Groningen (referred to as Offline Processing, or OLAP), and recorded to storage nodes in the current LOFAR offline processing cluster. The first data processing step is to flag the data in time and frequency, and optionally to compress the data in time, frequency, or both (Default Pre-Processing Pipeline, or DPPP in Fig. 6.3). At this step, the subtraction of the contributions of the brightest sources in the sky from the visibilities is also planned to be included. This procedure is currently under development by the imaging team. Next, the calibration steps begin. Using the BlackBoard Selfcal (BBS) system that has been developed for LOFAR, a local sky model (LSM) is generated from a Global Sky Model (GSM) that is stored in a database. Calibration of the complex station gains is achieved using this LSM. At this stage, an additional flagging operation (not shown in Fig. 6.3) is performed with DPPP in order to clip any remaining RFI or bad data. Next, the calibrated data are imaged using either the CImager[3], or more typically at present, the imager provided as part of the CASA package. One or more major cycle loops of calibration, flagging, imaging, and LSM updates are performed. At the end of the process, the final LSM will be used to update the GSM, and final image products will be available.

The pipeline is already functional as an automated processing chain. However, test of the pipeline software is still undergoing significant work, and each individual components of the process is being used independently for commissioning purposes. These tests represent the main tasks of the imaging busy weeks.

6.4 Imaging of LOFAR data: technical issues

The main critical issues related to the imaging of LOFAR data can be summarized as follows:

---

[2]The pipeline is currently implemented in python, and is an adaptation of the LOFAR Transient Pipeline (see Swinbank 2010 for a more complete description).

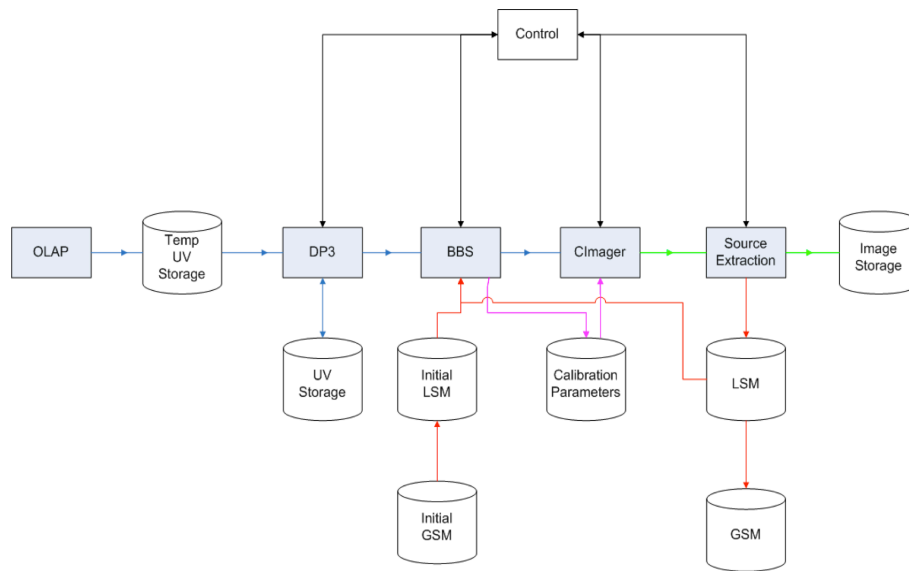[3]which is under development for the ASKAP telescope

Figure 6.3: Schematic representation of the LOFAR Imaging Pipeline, courtesy of R. Nijboer (ASTRON). See the text for a description of the various software components and the data path.

- **RFI mitigation**: the RFI excision is crucial at low frequencies. The high time and frequency resolutions of LOFAR data allow a relatively ease detection of RFI (thus minimizing the data loss). However, due to the large volume of data and the high sensitivity requirements of many projects, sophisticated automated flagging procedures are required. Efficient algorithms are still implemented in imaging pipeline (DPPP, see above). Moreover, new algorithms for automatic data flagging have been recently developed and being tested on LOFAR data by the imaging team (Offringa et al. 2010);

- **ionospheric calibration**: the ionospheric conditions below 70 MHz are poorly constrained, and need to be tested. Accurate ionospheric TEC (total electronic content) models are required, to predict the ionospheric behaviour at long wavelengths. Calibration algorithms that properly model and remove the ionospheric effects from the data (such as SPAM, Intema et al. 2009) are under development and are being tested on LOFAR observations.

- **wide field imaging related issues**: the LOFAR large fields of view require advanced wide field imaging techniques to be employed (either through faceting and w-projection algorithms). Moreover, the presence of very bright off-axis sources can interfere with the observed target, and directional-dependent self

calibration procedure are needed.

In particular, a few very strong radio sources can potentially contaminate each LOFAR observation (the so called the "A-team": *i.e.,* CygA, CasA, VirA). These sources need to be properly imaged over the entire observing band and subtracted from the target field. This is one of the main activities of the imaging busy weeks.

6.5   Early commissioning image of A2256

As initial test of the LOFAR imaging capabilities, during May 2010, a campaign of imaging commissioning, with emphasis on complicated fields containing extended sources, was started. Data sets were taken for a range of objects including M51, Cygnus A, 3C61.1, NGC 6251 (see Heald et al. 2010 and Wucknitz 2010).

In this campaign, a few galaxy clusters containing diffuse radio emission has also been observed. Here, first results from the LOFAR observation of the cluster A 2256 are reported. These results are due to the efforts of many people in the imaging team.

Abell 2256 is a textbook example of a cluster hosting both a radio relic and halo (see Sec. 1.6; Fig. 1.5). This cluster was observed with LOFAR in the HBA band ($115 - 165$ MHz) for about 8 hours. The data were taken with 10 core stations and 5 remote stations (the core stations were split resulting in a total of 25 stations). An image was made using 18 sub-bands covering a total of 4 MHz of bandwidth around 135 MHz. The resolution of the image is $30''\times20''$ and the noise is a few mJy beam^{-1} (see Figure 6.4). The yellow (brighter) regions in the image are associated with several disturbed radio galaxies. The large-scale emission in red and blue is mostly from the radio relic, although additional faint emission in the south of the cluster (bottom of the image) comes from the radio halo. So far, deep images at low frequencies have been obtained with the GMRT at 150 MHz (Intema 2009, rms $\sim$2.1 mJy/b; Kale et al. 2010, rms $\sim$ 3.6 mJy/b). These images only tentatively recovers some of the central halo emission. The LOFAR very sensitive central core more clearly detect the central halo, showing LOFAR's capabilities for the study diffuse steep spectrum emission in clusters. Next steps in improving this image are reducing the data from all the 256 sub bands, and the

application of more sophisticated data reduction algorithms. These include iteration of self-calibration/peeling loops, and proper application of ionospheric corrections (Intema et al. 2009).

Furthermore, with the station calibration recently operational and all the 36 station Dutch stations soon available, new commissioning observations will be able to reach two order of magnitude deeper images.
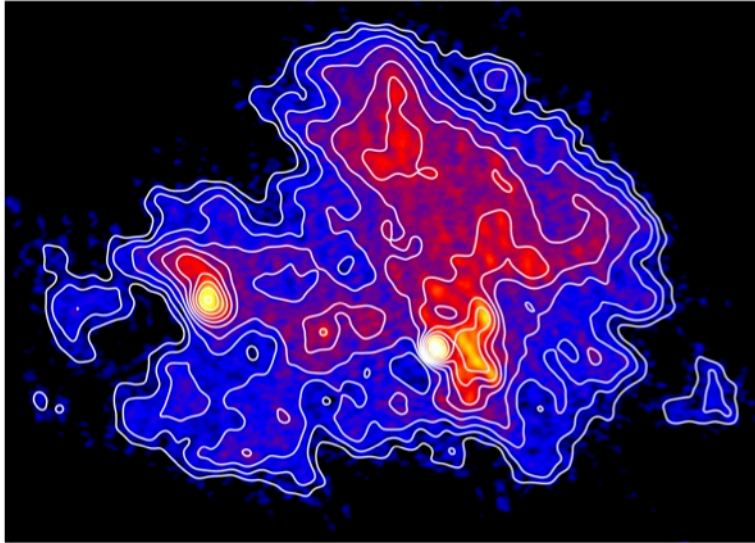
Figure 6.4: A 135 MHz LOFAR image of A 2256. The image has been made from data taken with 10 core stations and 5 remote stations. Only 4 MHz bandwidth out of a total 48 MHz was used during the reduction. The resolution of the image is about $30'' \times 20''$; the contour levels begin at 22 mJy beam^{-1}, and increase in increments of 25%.

These observations are crucial to test the available software for the data reduction and to optimize them in order to image the diffuse extended cluster emission.

Conclusions and future perspectives

The purpose of this thesis was to improve the knowledge of the spectral properties of diffuse radio sources in galaxy clusters, and of their connection with the thermal properties of the host cluster, that are crucial aspects to understand their origin.

With this aim, we studied in detail the diffuse radio emission in two clusters: the central radio halo in A 697, and the complex diffuse source in A 754. We studied their spectral properties thanks to proprietary low frequency GMRT observations, combined with VLA archival data. Furthermore, we investigated their connection with the thermal X-ray gas, by means of *Chandra* public data (for A 697), as well as new *Chandra* deep observations (for A 754).

Moreover, in this thesis we focused on the importance of low frequency observations for the study of radio halos with very steep spectrum (USSRH, $\alpha \geq 1.5$), which are suitable target to discriminate between the models proposed for the origin of radio halos. In this respect, we performed 150 MHz GMRT follow-up observations of three clusters hosting an USSRH, and presented preliminary results for two of them (A 697 and A 521). In the light of the fact that LOFAR will be the future instrument to address the questions of the origin and evolution of diffuse cluster radio sources, experience has been gained in the acquisition, reduction and analysis of the first data delivered by the LOFAR core.

Summary of the results

- **USSRHs: the case of A 697.**

  Thanks to new high sensitivity GMRT observations at 325 MHz we confirmed that A 697 hosts the second USSRH known to date, after the discovery of prototypical USSRH in A 521.

We have performed an accurate study of its integrated spectrum, by using the new GMRT 325 MHz observations, together with previous GMRT observations at 610 MHz, and VLA-C archival data at 1.4 GHz.

The radio spectrum, determined with three data points in the frequency range 325 MHz–1.4 GHz, has a spectral index $\alpha_{325\ \mathrm{MHz}}^{1.4\ \mathrm{GHz}} = 1.8 \pm 0.1$. We have performed an accurate analysis of the fraction of flux density that might be missed in our GMRT observations due to the u–v coverage at short spacings (through the "fake radio halo" procedure). This analysis led to an estimated spectral index $\alpha_{\mathrm{rev}}=1.7$.

The largest extent of the radio halo at 325 MHz is $\sim 5'$ (corresponding to 1.3 Mpc h_{70}^{-1}), and it is considerably larger than at higher frequencies. This property is similar to that of the USSRH in A 521, and different from what is observed in "classical" radio halos (*i.e.,* with flatter spectral indexes, $\alpha \sim 1.2 - 1.4$).

Although to a qualitative level, a re-analysis of *Chandra* archival data supports the idea of a complex dynamical state of the cluster, which is likely undergoing multiple mergers events. A comparison between the 325 MHz radio emission and the X-ray image reveals that the halo resembles the X-ray morphology, both in terms of extension and elongation. The very steep spectrum of the giant halo in A 697 allowed a prompt test of the hadronic models for the origin of radio halos. Assuming that the halo originates from the injection of secondary electrons, we showed that its very steep spectrum implies an implausibly large energy budget of relativistic protons. Thus, a hadronic origin is disfavoured. It is noteworthy that USSRHs are expected in the framework of turbulent re-acceleration models for the origin of radio halos, as consequence of less energetic mergers. This population of radio halos is also predicted to be more common in the Universe, and more easily detectable at low frequencies.

- **USSRHs: GMRT follow-up at 150 MHz**.

We have performed an observational campaign of GMRT 150 MHz follow up observations of three clusters hosting (either candidate or confirmed) USSRHs: A 697, A 521, A 1682. These high sensitivity ($\sim$10 hours/cluster) observations are aimed to study their low frequency properties, and to characterize their

low frequency spectrum. We have presented preliminary results at 150 MHz for A 697. In our preliminary image, the radio halo shows a rather patchy morphology, and appears to be more extended with respect to higher frequencies. We estimate that the total flux density at 150 MHz is in the range 165-250 mJy, allowing for calibration uncertainties and for the uncertainties in the subtraction of the individual radio sources embedded in the radio halo. Despite the large uncertainty, the flux density at 150 MHz is still consistent with a steep spectrum with $\alpha \sim 1.7$. We trust that further improvements in the calibration and imaging (currently in progress), as well as an appropriate subtraction of the individual embedded radio sources, will allow us to derive a more accurate flux density value at this frequency.

The large field of view of our deep observation of the A 697 also allowed us to detect a candidate diffuse radio source in the field of view. This source is located far away from the cluster centre. Its nature is unclear, due to the lack of information at other frequencies, and clear optical counterpart.

We showed a preliminary 150 MHz image of A521. The USSRH is barely detected in this image, due to its low surface brightness and the still relatively high rms noise. Data reduction is in progress. The bright radio relic dominates the image, and we estimated its total flux density at 150 MHz, which is 327 ± 49 mJy. This value lies on the power law spectrum with $\alpha \simeq 1.5$, as determined in the frequency range 235 MHz–5 GHz.

- **Merger shocks and diffuse radio emission: the case of A 754**.

  We have performed a combined X–ray and radio study of the nearby prototypical merging galaxy cluster A 754. From the surface brightness and spectral analysis of new deep *Chandra* observation, we confirmed the presence of a merger shock front East of the cluster core. We provided the Mach number from the density jump across the shock M= $1.57^{+0.16}_{-0.12}$, and a direct measurement of a positive gas temperature jump across the arc-like brightness edge, $T_2/T_1 = 2.2^{+1.1}_{-0.7}$. A 754 is only the fourth cluster with a clear detection of a merger shock.

  The new GMRT radio image of the cluster at 330 MHz revealed that the centrally located diffuse emission is very extended and complex, and is mainly

elongated in the East-West direction. Most interestingly, the eastern edge of this source coincides with the shock. We studied the spectral properties of the diffuse radio emission, using the GMRT data, archival *VLA* data at 1.4 GHz, and previous *VLA* results at 74 MHz. We found that the region next to the radio edge (previously defined *relic* region) has a very steep integrated spectrum, with $\alpha_{0.3GHz}^{1.4GHz} = 2.02 \pm 0.04$ and $\alpha_{0.07GHz}^{0.3GHz} = 1.77 \pm 0.10$. This is steeper than the average spectrum of the whole diffuse emission, $\alpha_{0.3GHz}^{1.4GHz} = 1.57 \pm 0.05$, which is in itself steeper than the typical spectrum of radio halos. This is the second case in the literature with a clear coincidence between a shock and a diffuse radio feature.

On the basis of the spatial coincidence of the shock front with the edge of the non-thermal diffuse emission, we have discussed its origin in the framework of the possible scenarios. The observed coincidence suggests a physical connection. Due to the low Mach number ($M \sim 1.6$) of the shock and the very steep synchrotron spectrum of the edge ($\alpha \simeq 2$) direct shock acceleration of thermal particles for the origin of the edge is ruled out, because it would require an implausibly high acceleration efficiency.

Other possible scenarios are re-acceleration and/or adiabatic compression of fossil relativistic plasma in the ICM. We argue that shock re-acceleration is more plausible for such weak shock. This process should produce a spectrum of electrons that is consistent with the observed steep radio spectrum of the relic region.

Finally, we briefly discussed the possibility of an indirect connection between the shock and the radio edge. The shock passage may drive small-scale turbulence able to re-accelerate electrons over the cluster volume, explaining both the steep spectrum radio edge close to the shock, and the diffuse emission on larger scale.

Future perspectives

Our work has not ended. Short and long term perspectives are highlighted and briefly summarized here.

- In the present thesis we have thrown a light on the origin of USSRH and on the connection between merger shocks and associated steep spectrum radio

emission. A number of questions however are still pending, and for this reason follow-up projects have already started.

Concerning the case of A 697, it is essential to constrain both the low frequency and high frequency end of the spectrum, so as to derive a spectral shape to be compared to the theoretical expectations. To this aim, we have recently performed high sensitivity observations of the radio halo in the L band (1.3 and 1.7 GHz) with the EVLA in the C and D configuration. The data reduction is in progress. Preliminary results on two chunks of EVLA D-array data were presented. Once the data from the C and D array will be completely reduced and combined, we expect to derive accurate flux density measurements of the radio halo at 1.3 GHz and 1.7 GHz, and thus derive the spectral shape in the frequency range 150 MHz - 1.7 GHz with 5 data points.

GMRT high sensitivity observations have just been carried out for A 754 at 150, 235, 330 MHz (February 2011), with two different aims: *(i)* to derive an integrated spectrum for the diffuse radio emission with 5 data points between 74 MHz and 1.4 GHz, and *(ii)* to perform a spectral imaging analysis between pairs of frequencies, in order to study possible steepening trends, to be compared with the theoretical expectations for the shock-diffuse radio emission connection.

The 150 MHz follow-up of USSRHs is in progress. In particular, we are working on the observations of A 1682, which hosts a candidate steep spectrum radio halo at its centre. The analysis of these 150 MHz data will allow to carry out an appropriate study of this source. Once final images of all our 150 MHz sample will be obtained, we will have the chance to characterize the low frequency properties of USSRHs, and to improve our understanding of the origin of radio halos. Moreover, beyond this main target, the combined large field of view and the high sensitivity of each 150 MHz pointing, may allow to detect new diffuse steep spectrum radio sources. A candidate diffuse source has been indeed detected in the A 697 field of view, and we are planning pointed follow up radio observations.

- LOFAR will soon become the reference instrument in the study of diffuse emission in clusters of galaxies. LOFAR will observe large areas of the sky

with unprecedented sensitivity, and will cover the optimal frequency range (10–240 MHz) to detect and study these sources. The instrument is now in the commissioning phase, and first images of clusters hosting diffuse central radio emission already revealed its extreme capabilities in this research field. We thus expect to be able to considerably improve our knowledge of diffuse cluster radio sources. In particular, we trust there will be a relevant contribution to the statistical properties of radio halos, and to the number of USSRHs, expected to be related to minor mergers and less energetic mass assembly processes in the formation of galaxy clusters.

Bibliography

Abell, G. O., Corwin, Jr., H. G., & Olowin, R. P. 1989, ApJS, 70, 1

Ackermann, M., Ajello, M., Allafort, A., et al. 2010, ApJL, 717, L71

Aharonian, F., Akhperjanian, A. G., Anton, G., et al. 2009a, A&A, 495, 27

Aharonian, F., Akhperjanian, A. G., Anton, G., et al. 2009b, A&A, 502, 437

Ajello, M., Rebusco, P., Cappelluti, N., et al. 2009, ApJ, 690, 367

Ajello, M., Rebusco, P., Cappelluti, N., et al. 2010, ApJ, 725, 1688

Allen, S. W., Schmidt, R. W., & Fabian, A. C. 2002, MNRAS, 334, L11

Bacchi, M., Feretti, L., Giovannini, G., & Govoni, F. 2003, A&A, 400, 465

Badhwar, G. D., Golden, R. L., & Stephens, S. A. 1977, Phys. Rev. D, 15, 820

Bagchi, J., Durret, F., Neto, G. B. L., & Paul, S. 2006, Science, 314, 791

Ballarati, B., Feretti, L., Ficarra, A., et al. 1981, A&A, 100, 323

Bartlett, J. G. 2006, ArXiv Astrophysics e-prints

Bauer, F. E., Fabian, A. C., Sanders, J. S., Allen, S. W., & Johnstone, R. M. 2005, MNRAS, 359, 1481

Belsole, E., Sauvageot, J., Pratt, G. W., & Bourdin, H. 2005, Advances in Space Research, 36, 630

Biviano, A. 2000, in Constructing the Universe with Clusters of Galaxies

Blandford, R. & Eichler, D. 1987, Phys. Rep., 154, 1

Blasi, P. & Colafrancesco, S. 1999, Astroparticle Physics, 12, 169

130

Blasi, P., Gabici, S., & Brunetti, G. 2007, International Journal of Modern Physics A, 22, 681

Böhringer, H., Schuecker, P., Guzzo, L., et al. 2004, A&A, 425, 367

Böhringer, H., Schuecker, P., Pratt, G. W., et al. 2007, A&A, 469, 363

Böhringer, H., Voges, W., Huchra, J. P., et al. 2000, ApJS, 129, 435

Bonafede, A., Feretti, L., Giovannini, G., et al. 2009a, A&A, 503, 707

Bonafede, A., Feretti, L., Murgia, M., et al. 2010, A&A, 513, A30+

Bonafede, A., Giovannini, G., Feretti, L., Govoni, F., & Murgia, M. 2009b, A&A, 494, 429

Bonamente, M., Joy, M. K., LaRoque, S. J., et al. 2006, ApJ, 647, 25

Borgani, S., Murante, G., Springel, V., et al. 2004, MNRAS, 348, 1078

Brentjens, M. A. 2008, A&A, 489, 69

Briel, U. G., Henry, J. P., & Boehringer, H. 1992, A&A, 259, L31

Briel, U. G., Henry, J. P., Schwarz, R. A., et al. 1991, A&A, 246, L10

Brown, S. & Rudnick, L. 2010, ArXiv e-prints

Brunetti, G. 2003, in Astronomical Society of the Pacific Conference Series, Vol. 301, Astronomical Society of the Pacific Conference Series, ed. S. Bowyer & C.-Y. Hwang, 349–+

Brunetti, G. 2004, Journal of Korean Astronomical Society, 37, 493

Brunetti, G. 2009, A&A, 508, 599

Brunetti, G. & Blasi, P. 2005, MNRAS, 363, 1173

Brunetti, G. & Cassano, R. 2010, in ISKAF2010 Science Meeting

Brunetti, G., Cassano, R., Dolag, K., & Setti, G. 2009, A&A, 507, 661

Brunetti, G., Giacintucci, S., Cassano, R., et al. 2008, Nature, 455, 944

Brunetti, G. & Lazarian, A. 2007, MNRAS, 378, 245

Brunetti, G. & Lazarian, A. 2010, ArXiv e-prints

Brunetti, G., Setti, G., Feretti, L., & Giovannini, G. 2001, MNRAS, 320, 365

Brunetti, G., Venturi, T., Dallacasa, D., et al. 2007, ApJL, 670, L5

Buote, D. A. 2001, ApJL, 553, L15

Burns, J. O., Sulkanen, M. E., Gisler, G. R., & Perley, R. A. 1992, ApJL, 388, L49

Bykov, A. M., Dolag, K., & Durret, F. 2008, SSRv, 134, 119

Cassano, R. 2009, in Astronomical Society of the Pacific Conference Series, Vol.
    407, Astronomical Society of the Pacific Conference Series, ed. D. J. Saikia,
    D. A. Green, Y. Gupta, & T. Venturi, 223–+

Cassano, R. 2010, A&A, 517, A10+

Cassano, R. & Brunetti, G. 2005, MNRAS, 357, 1313

Cassano, R., Brunetti, G., Röttgering, H. J. A., & Brüggen, M. 2010a, A&A, 509,
    A68+

Cassano, R., Brunetti, G., & Setti, G. 2006, MNRAS, 369, 1577

Cassano, R., Brunetti, G., Setti, G., Govoni, F., & Dolag, K. 2007, MNRAS, 378,
    1565

Cassano, R., Brunetti, G., Venturi, T., et al. 2008, A&A, 480, 687

Cassano, R., Ettori, S., Giacintucci, S., et al. 2010b, ApJL, 721, L82

Cavaliere, A. & Fusco-Femiano, R. 1976, A&A, 49, 137

Cavaliere, A. & Fusco-Femiano, R. 1978, A&A, 70, 677

Churazov, E., Forman, W., Jones, C., Sunyaev, R., & Böhringer, H. 2004, MNRAS,
    347, 29

Churazov, E., Forman, W., Vikhlinin, A., et al. 2008, MNRAS, 388, 1062

Clarke, T. E. 2004, Journal of Korean Astronomical Society, 37, 337

Clarke, T. E. & Ensslin, T. A. 2006, AJ, 131, 2900

132

Clarke, T. E., Kronberg, P. P., & Böhringer, H. 2001, ApJL, 547, L111

Clowe, D., Bradač, M., Gonzalez, A. H., et al. 2006, ApJL, 648, L109

Cohen, A. S. & Röttgering, H. J. A. 2009, AJ, 138, 439

Condon, J. J., Cotton, W. D., Greisen, E. W., et al. 1998, AJ, 115, 1693

Cotton, W. D., Condon, J. J., Perley, R. A., et al. 2004, in Presented at the Society of Photo-Optical Instrumentation Engineers (SPIE) Conference, Vol. 5489, Society of Photo-Optical Instrumentation Engineers (SPIE) Conference Series, ed. J. M. Oschmann Jr., 180–189

Dahle, H., Kaiser, N., Irgens, R. J., Lilje, P. B., & Maddox, S. J. 2002, ApJS, 139, 313

Dallacasa, D., Brunetti, G., Giacintucci, S., et al. 2009, ApJ, 699, 1288

De Grandi, S. & Molendi, S. 2001, ApJ, 551, 153

de Vos, M., Gunst, A. W., & Nijboer, R. 2009, IEEE Proceedings, 97, 1431

Deiss, B. M., Reich, W., Lesch, H., & Wielebinski, R. 1997, A&A, 321, 55

Dennison, B. 1980, ApJL, 239, L93

Dermer, C. D. 1986, A&A, 157, 223

Diaferio, A. 1999, MNRAS, 309, 610

Dolag, K. & Enßlin, T. A. 2000, A&A, 362, 151

Dolag, K., Vazza, F., Brunetti, G., & Tormen, G. 2005, MNRAS, 364, 753

Donnert, J., Dolag, K., Cassano, R., & Brunetti, G. 2010, MNRAS, 407, 1565

Dressler, A. 1980, ApJ, 236, 351

Ebeling, H., Barrett, E., & Donovan, D. 2004, ApJL, 609, L49

Ebeling, H., Edge, A. C., Allen, S. W., et al. 2000, MNRAS, 318, 333

Ebeling, H., Edge, A. C., Bohringer, H., et al. 1998, MNRAS, 301, 881

Enßlin, T., Pfrommer, C., Miniati, F., & Subramanian, K. 2011, A&A, 527, A99+

Enßlin, T. A. 1999, in Diffuse Thermal and Relativistic Plasma in Galaxy Clusters, ed. H. Boehringer, L. Feretti, & P. Schuecker, 275–+

Ensslin, T. A., Biermann, P. L., Klein, U., & Kohle, S. 1998, A&A, 332, 395

Enßlin, T. A. & Brüggen, M. 2002, MNRAS, 331, 1011

Enßlin, T. A. & Gopal-Krishna. 2001, A&A, 366, 26

Fabian, A. C. 1994, ARA&A, 32, 277

Fabricant, D., Beers, T. C., Geller, M. J., et al. 1986, ApJ, 308, 530

Falcke, H. D., van Haarlem, M. P., de Bruyn, A. G., et al. 2007, Highlights of Astronomy, 14, 386

Felten, J. E., Gould, R. J., Stein, W. A., & Woolf, N. J. 1966, ApJ, 146, 955

Feretti, L. 1999, in Diffuse Thermal and Relativistic Plasma in Galaxy Clusters, ed. H. Boehringer, L. Feretti, & P. Schuecker, 3–+

Feretti, L. 2003, in Astronomical Society of the Pacific Conference Series, Vol. 301, Astronomical Society of the Pacific Conference Series, ed. S. Bowyer & C.-Y. Hwang, 143–+

Feretti, L., Fusco-Femiano, R., Giovannini, G., & Govoni, F. 2001, A&A, 373, 106

Feretti, L., Giovannini, G., & Bohringer, H. 1997, NewA, 2, 501

Feretti, L., Orrù, E., Brunetti, G., et al. 2004, A&A, 423, 111

Feretti, L., Schuecker, P., Böhringer, H., Govoni, F., & Giovannini, G. 2005, A&A, 444, 157

Ferrari, C., Govoni, F., Schindler, S., Bykov, A. M., & Rephaeli, Y. 2008, SSRv, 134, 93

Finoguenov, A., Henriksen, M. J., Miniati, F., Briel, U. G., & Jones, C. 2006, ApJ, 643, 790

Fujita, Y., Takizawa, M., & Sarazin, C. L. 2003, ApJ, 584, 190

Fusco-Femiano, R., Dal Fiume, D., De Grandi, S., et al. 2000, ApJL, 534, L7

134

Fusco-Femiano, R., dal Fiume, D., Feretti, L., et al. 1999, ApJL, 513, L21

Fusco-Femiano, R., Landi, R., & Orlandini, M. 2005, ApJL, 624, L69

Fusco-Femiano, R., Landi, R., & Orlandini, M. 2007, ApJL, 654, L9

Fusco-Femiano, R., Orlandini, M., Brunetti, G., et al. 2004, ApJL, 602, L73

Fusco-Femiano, R., Orlandini, M., De Grandi, S., et al. 2003, A&A, 398, 441

Giacconi, R., Murray, S., Gursky, H., et al. 1972, ApJ, 178, 281

Giacintucci, S. 2007, PhD thesis, Astronomy Department, University of Bologna, http://amsdottorato.cib.unibo.it/353/

Giacintucci, S., Markevitch, M., Brunetti, G., Cassano, R., & Venturi, T. 2011, A&A, 525, L10+

Giacintucci, S., Venturi, T., Bardelli, S., et al. 2006, NewA, 11, 437

Giacintucci, S., Venturi, T., Brunetti, G., et al. 2005, A&A, 440, 867

Giacintucci, S., Venturi, T., Brunetti, G., et al. 2009, A&A, 505, 45

Giacintucci, S., Venturi, T., Macario, G., et al. 2008, A&A, 486, 347

Gilfanov, M. R., Syunyaev, R. A., & Churazov, E. M. 1987, Soviet Astronomy Letters, 13, 3

Giovannini, G., Bonafede, A., Feretti, L., et al. 2009, A&A, 507, 1257

Giovannini, G. & Feretti, L. 2002, in Astrophysics and Space Science Library, Vol. 272, Merging Processes in Galaxy Clusters, ed. L. Feretti, I. M. Gioia, & G. Giovannini, 197–227

Giovannini, G., Feretti, L., & Stanghellini, C. 1991, A&A, 252, 528

Giovannini, G., Feretti, L., Venturi, T., Kim, K., & Kronberg, P. P. 1993, ApJ, 406, 399

Giovannini, G., Tordi, M., & Feretti, L. 1999, NewA, 4, 141

Girardi, M. & Biviano, A. 2002, in Astrophysics and Space Science Library, Vol. 272, Merging Processes in Galaxy Clusters, ed. L. Feretti, I. M. Gioia, & G. Giovannini, 39–77

Girardi, M., Boschin, W., & Barrena, R. 2006, A&A, 455, 45

Gitti, M., Ferrari, C., Domainko, W., Feretti, L., & Schindler, S. 2007, A&A, 470, L25

Gómez, P. L., Loken, C., Roettiger, K., & Burns, J. O. 2002, ApJ, 569, 122

Govoni, F., Dolag, K., Murgia, M., et al. 2010, A&A, 522, A105+

Govoni, F. & Feretti, L. 2004, International Journal of Modern Physics D, 13, 1549

Govoni, F., Feretti, L., Giovannini, G., et al. 2001a, A&A, 376, 803

Govoni, F., Markevitch, M., Vikhlinin, A., et al. 2004, ApJ, 605, 695

Govoni, F., Murgia, M., Feretti, L., et al. 2005, A&A, 430, L5

Govoni, F., Murgia, M., Markevitch, M., et al. 2009, A&A, 499, 371

Govoni, F., Taylor, G. B., Dallacasa, D., Feretti, L., & Giovannini, G. 2001b, A&A, 379, 807

Greisen, E. W., Spekkens, K., & van Moorsel, G. A. 2009, AJ, 137, 4718

Gunn, J. E., Hoessel, J. G., & Oke, J. B. 1986, ApJ, 306, 30

Hales, S. E. G., Riley, J. M., Waldram, E. M., Warner, P. J., & Baldwin, J. E. 2007, MNRAS, 382, 1639

Heald, G., McKean, J., Pizzo, R., et al. 2010, ArXiv e-prints

Henriksen, M. J. & Markevitch, M. L. 1996, ApJL, 466, L79+

Henry, J. P. & Briel, U. G. 1995, ApJL, 443, L9

Henry, J. P., Finoguenov, A., & Briel, U. G. 2004, ApJ, 615, 181

Herzog, E., Wild, P., & Zwicky, F. 1957, PASP, 69, 409

Hickox, R. C. & Markevitch, M. 2006, ApJ, 645, 95

136

Hoeft, M. & Brüggen, M. 2007, MNRAS, 375, 77

Iapichino, L. & Niemeyer, J. C. 2008, MNRAS, 388, 1089

Intema, H. T. 2009, PhD thesis, Leiden Observatory, Leiden University, P.O. Box 9513, 2300 RA Leiden, The Netherlands

Intema, H. T., van der Tol, S., Cotton, W. D., et al. 2009, A&A, 501, 1185

Jaffe, W. J. 1977, ApJ, 212, 1

Jeltema, T. E., Canizares, C. R., Bautz, M. W., & Buote, D. A. 2005, ApJ, 624, 606

Johnston-Hollitt, M., Clay, R. W., Ekers, R. D., Wieringa, M. H., & Hunstead, R. W. 2002, in IAU Symposium, Vol. 199, The Universe at Low Radio Frequencies, ed. A. Pramesh Rao, G. Swarup, & Gopal-Krishna, 157–+

Johnston-Hollitt, M. & Ekers, R. D. 2004, ArXiv Astrophysics e-prints

Jones, C. & Forman, W. 1984, ApJ, 276, 38

Jones, C. & Forman, W. 1999, ApJ, 511, 65

Kalberla, P. M. W., Burton, W. B., Hartmann, D., et al. 2005, A&A, 440, 775

Kale, R. & Dwarakanath, K. S. 2009, ApJ, 699, 1883

Kale, R. & Dwarakanath, K. S. 2010, ApJ, 718, 939

Kassim, N. E., Clarke, T. E., Enßlin, T. A., Cohen, A. S., & Neumann, D. M. 2001, ApJ, 559, 785

Katz, N. & White, S. D. M. 1993, ApJ, 412, 455

Kempner, J. C. & Sarazin, C. L. 2001, ApJ, 548, 639

Kim, K., Kronberg, P. P., Dewdney, P. E., & Landecker, T. L. 1990, ApJ, 355, 29

Komissarov, S. S. & Gubanov, A. G. 1994, A&A, 285, 27

Krivonos, R. A., Vikhlinin, A. A., Markevitch, M. L., & Pavlinsky, M. N. 2003, Astronomy Letters, 29, 425

Large, M. I., Mathewson, D. S., & Haslam, C. G. T. 1959, Nature, 183, 1663

Lau, E. T., Kravtsov, A. V., & Nagai, D. 2009, ApJ, 705, 1129

Liang, H., Hunstead, R. W., Birkinshaw, M., & Andreani, P. 2000, ApJ, 544, 686

Longair, M. S. 1981, High energy astrophysics. an informal introduction for students of physics and astronomy, ed. Longair, M. S.

Macario, G., Markevitch, M., Giacintucci, S., et al. 2011a, ApJ, 728, 82

Macario, G., Venturi, T., Brunetti, G., et al. 2010, A&A, 517, A43+

Macario, G., Venturi, T., Dallacasa, D., et al. 2011b, ArXiv e-prints

Markevitch, M. 2006, in ESA Special Publication, Vol. 604, The X-ray Universe 2005, ed. A. Wilson, 723–+

Markevitch, M. 2010, ArXiv e-prints

Markevitch, M., Bautz, M. W., Biller, B., et al. 2003a, ApJ, 583, 70

Markevitch, M., Forman, W. R., Sarazin, C. L., & Vikhlinin, A. 1998, ApJ, 503, 77

Markevitch, M., Gonzalez, A. H., David, L., et al. 2002, ApJL, 567, L27

Markevitch, M., Govoni, F., Brunetti, G., & Jerius, D. 2005, ApJ, 627, 733

Markevitch, M., Mazzotta, P., Vikhlinin, A., et al. 2003b, ApJL, 586, L19

Markevitch, M., Sarazin, C. L., & Vikhlinin, A. 1999, ApJ, 521, 526

Markevitch, M. & Vikhlinin, A. 2001, ApJ, 563, 95

Markevitch, M. & Vikhlinin, A. 2007, Phys. Rep., 443, 1

Markevitch, M., Vikhlinin, A., Mazzotta, P., & VanSpeybroeck, L. 2000, ArXiv Astrophysics e-prints

Mazzotta, P. & Giacintucci, S. 2008, ApJL, 675, L9

Mazzotta, P., Rasia, E., Moscardini, L., & Tormen, G. 2004, MNRAS, 354, 10

McCarthy, I. G., Frenk, C. S., Font, A. S., et al. 2008, MNRAS, 383, 593

Mewe, R. & Gronenschild, E. H. B. M. 1981, A&AS, 45, 11

Moskalenko, I. V. & Strong, A. W. 1998, ApJ, 493, 694

Murgia, M., Govoni, F., Feretti, L., et al. 2004, A&A, 424, 429

Nagai, D., Kravtsov, A. V., & Vikhlinin, A. 2007, ApJ, 668, 1

Offringa, A. R., de Bruyn, A. G., Zaroubi, S., & Biehl, M. 2010, ArXiv e-prints

O'Hara, T. B., Mohr, J. J., Bialek, J. J., & Evrard, A. E. 2006, ApJ, 639, 64

Orrú, E., Murgia, M., Feretti, L., et al. 2007, A&A, 467, 943

Paul, S., Iapichino, L., Miniati, F., Bagchi, J., & Mannheim, K. 2011, ApJ, 726, 17

Peres, C. B., Fabian, A. C., Edge, A. C., et al. 1998, MNRAS, 298, 416

Peterson, J. R. & Fabian, A. C. 2006, Phys. Rep., 427, 1

Peterson, J. R., Kahn, S. M., Paerels, F. B. S., et al. 2003, ApJ, 590, 207

Peterson, J. R., Paerels, F. B. S., Kaastra, J. S., et al. 2001, A&A, 365, L104

Petrosian, V. 2001, ApJ, 557, 560

Pfrommer, C. & Enßlin, T. A. 2004, Journal of Korean Astronomical Society, 37, 455

Pfrommer, C., Springel, V., Enßlin, T. A., & Jubelgas, M. 2006, MNRAS, 367, 113

Pizzo, R. F., de Bruyn, A. G., Bernardi, G., & Brentjens, M. A. 2011, A&A, 525, A104+

Ramella, M., Biviano, A., Pisani, A., et al. 2007, A&A, 470, 39

Randall, S. W., Sarazin, C. L., & Ricker, P. M. 2002, ApJ, 577, 579

Reimer, O., Pohl, M., Sreekumar, P., & Mattox, J. R. 2003, ApJ, 588, 155

Reiprich, T. H. & Böhringer, H. 2002, ApJ, 567, 716

Rengelink, R. B., Tang, Y., de Bruyn, A. G., et al. 1997, A&AS, 124, 259

Rephaeli, Y. & Gruber, D. 2003, ApJ, 595, 137

Rephaeli, Y., Nevalainen, J., Ohashi, T., & Bykov, A. M. 2008, SSRv, 134, 71

Ricker, P. M. & Sarazin, C. L. 2001, ApJ, 561, 621

Roettiger, K., Burns, J. O., & Stone, J. M. 1999a, ApJ, 518, 603

Roettiger, K., Stone, J. M., & Burns, J. O. 1999b, ApJ, 518, 594

Roettiger, K., Stone, J. M., & Mushotzky, R. F. 1998, ApJ, 493, 62

Rossetti, M. & Molendi, S. 2004, A&A, 414, L41

Rossetti, M. & Molendi, S. 2010, A&A, 510, A83+

Rottgering, H. J. A. 2010, in ISKAF2010 Science Meeting

Rottgering, H. J. A., Braun, R., Barthel, P. D., et al. 2006, ArXiv Astrophysics
    e-prints

Rottgering, H. J. A., Wieringa, M. H., Hunstead, R. W., & Ekers, R. D. 1997,
    MNRAS, 290, 577

Russell, H. R., Sanders, J. S., Fabian, A. C., et al. 2010, MNRAS, 406, 1721

Rybicki, G. B. & Lightman, A. P. 1979, Radiative processes in astrophysics, ed.
    Rybicki, G. B. & Lightman, A. P.

Ryu, D., Kang, H., Hallman, E., & Jones, T. W. 2003, ApJ, 593, 599

Sanders, J. S., Fabian, A. C., & Smith, R. K. 2011, MNRAS, 410, 1797

Santos, J. S., Rosati, P., Tozzi, P., et al. 2008, A&A, 483, 35

Sarazin, C. L. 1988, , 76, 639

Sarazin, C. L. 1999, ApJ, 520, 529

Sarazin, C. L. 2002, in Astrophysics and Space Science Library, Vol. 272, Merging
    Processes in Galaxy Clusters, ed. L. Feretti, I. M. Gioia, & G. Giovannini, 1–38

Schlickeiser, R., Sievers, A., & Thiemann, H. 1987, A&A, 182, 21

Schneider, P. 2006, in KITP: Blackboard Lunch Series

Schuecker, P., Böhringer, H., Reiprich, T. H., & Feretti, L. 2001, A&A, 378, 408

Schuecker, P., Finoguenov, A., Miniati, F., Böhringer, H., & Briel, U. G. 2004, A&A, 426, 387

Stecker, F. W. 1970, , 6, 377

Stephens, S. A. & Badhwar, G. D. 1981, , 76, 213

Struble, M. F. & Rood, H. J. 1999, ApJS, 125, 35

Subramanian, K., Shukurov, A., & Haugen, N. E. L. 2006, MNRAS, 366, 1437

Swinbank, J. D. 2010, in ISKAF2010 Science Meeting

Takizawa, M. 2005, ApJ, 629, 791

Thierbach, M., Klein, U., & Wielebinski, R. 2003, A&A, 397, 53

van Weeren, R. J., Röttgering, H. J. A., Brüggen, M., & Cohen, A. 2009, A&A, 505, 991

van Weeren, R. J., Röttgering, H. J. A., Brüggen, M., & Hoeft, M. 2010, Science, 330, 347

Vazza, F., Brunetti, G., Gheller, C., & Brunino, R. 2010a, NewA, 15, 695

Vazza, F., Brunetti, G., Gheller, C., Brunino, R., & Brüggen, M. 2010b, ArXiv e-prints

Vazza, F., Brunetti, G., Kritsuk, A., et al. 2009, A&A, 504, 33

Vazza, F., Tormen, G., Cassano, R., Brunetti, G., & Dolag, K. 2006, MNRAS, 369, L14

Venturi, T., Giacintucci, S., Brunetti, G., et al. 2007, A&A, 463, 937

Venturi, T., Giacintucci, S., Cassano, R., et al. 2009, in Astronomical Society of the Pacific Conference Series, Vol. 407, Astronomical Society of the Pacific Conference Series, ed. D. J. Saikia, D. A. Green, Y. Gupta, & T. Venturi, 232–+

Venturi, T., Giacintucci, S., Dallacasa, D., et al. 2008, A&A, 484, 327

Vikhlinin, A., Forman, W., & Jones, C. 1997, ApJL, 474, L7+

Vikhlinin, A., Forman, W., & Jones, C. 1999, ApJ, 525, 47

Vikhlinin, A., Kravtsov, A., Forman, W., et al. 2006, ApJ, 640, 691

Vikhlinin, A., Markevitch, M., Murray, S. S., et al. 2005, ApJ, 628, 655

Vogt, C. & Enßlin, T. A. 2005, A&A, 434, 67

Werner, N., Durret, F., Ohashi, T., Schindler, S., & Wiersma, R. P. C. 2008a, SSRv, 134, 337

Werner, N., Finoguenov, A., Kaastra, J. S., et al. 2008b, A&A, 482, L29

Wik, D. R., Sarazin, C. L., Finoguenov, A., et al. 2011, ApJ, 727, 119

Wik, D. R., Sarazin, C. L., Finoguenov, A., et al. 2009, ApJ, 696, 1700

Willson, M. A. G. 1970, MNRAS, 151, 1

Wucknitz, O. 2010, in ISKAF2010 Science Meeting

Zabludoff, A. I. & Zaritsky, D. 1995, ApJL, 447, L21+

Zwicky, F. & Kowal, C. T. 1968, "Catalogue of Galaxies and of Clusters of Galaxies", Volume VI, ed. Zwicky, F., Herzog, E., & Wild, P.